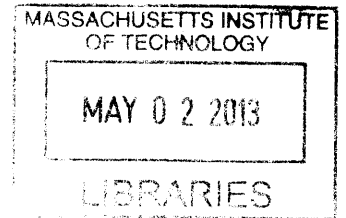


**Bio-inspired composites – a *de novo* approach to the  
conceptualization, design and synthesis of tough mesoscale  
structures with simple building blocks** **ARCHIVES**

by

Leon Sokratis Scheie Dimas



SUBMITTED TO THE DEPARTMENT OF CIVIL AND  
ENVIRONMENTAL ENGINEERING IN PARTIAL FULFILLMENT OF  
THE REQUIREMENTS FOR THE DEGREE OF

MASTERS OF SCIENCE IN CIVIL AND ENVIRONMENTAL  
ENGINEERING  
AT THE  
MASSACHUSETTS INSTITUTE OF TECHNOLOGY

February 2013

© 2013 Massachusetts Institute of Technology. All rights reserved.

Author: \_\_\_\_\_  
Department of Civil and Environmental Engineering  
January 18, 2013

Certified by: \_\_\_\_\_  
Markus J. Buehler  
Associate Professor of Civil and Environmental Engineering  
Thesis Supervisor

Accepted by: \_\_\_\_\_  
Heidi Nepf  
Chair, Departmental Committee for Graduate Students



Bio-inspired composites – a *de novo* approach to the  
conceptualization, design and synthesis of tough mesoscale  
structures with simple building blocks

by

Leon Sokratis Scheie Dimas

Submitted to the Department of Civil and Environmental Engineering on January 18, 2013, in partial fulfillment of the requirements for the degree of Master of Science in Civil and Environmental Engineering.

## Abstract

Composites play an important role as structural materials in a range of engineering fields due to their potential to combine the best mechanical properties of their constituents. In biology, composites are ubiquitous and exhibit fascinating and precise architectures at fine length scales, where bone, hexactinellid sponges and nacreous abalone shells are prime examples. By learning from nature a *de novo* approach is applied leading to the synthesis of bio-inspired tough composites with simple building blocks. Fundamental design principles employed by nature in the assembly of mineralized composites are elucidated with simple mesoscale discrete lattice models. Computational investigations show that specific topological arrangements of soft and stiff phases in composites can markedly change the stress and strain transfer through a system, thus fundamentally changing their fracture mechanical behavior. Indeed, architectures are created from brittle building blocks that exhibit stable fracture propagation under sustained load transfer and increasing deformation. Furthermore, a detailed study of the basic interactions between constituents phases in a composite lead to fundamental insights of elastic interactions and stiffness ratios as controlling elements of the fracture mechanical behavior of composite systems. Tuning the linear elastic constitutive behavior of the matrix phase in a bone-like topology creates a set of composites spanning a wide area of toughness vs. stiffness in the Ashby plot. One specific composite system, designed at ‘minimal cost’, exhibits a fracture toughness modulus eight times larger than its constituents while retaining over 80% of the Young’s modulus of its stiffest phase. Finally the insights gained from the computational investigations are used as input in a design process resulting in 3D printed bio-inspired composite specimens. Utilizing multi-material 3D printing with structural features at micrometer length scales composites are printed with toughness moduli an order of magnitude larger than their building blocks. A computational model capable of predicting the experimentally observed mechanisms and trends in mechanical behavior is also produced. The research presents exciting outlooks for the future design of tough, structurally robust bio-inspired materials with applications in a wide range of engineering disciplines.

Thesis Supervisor: Markus J. Buehler

Title: Associate Professor of Civil and Environmental Engineering





## **Acknowledgements**

This research was funded by the DOD-Army Research Office (grant number W911NF1010127, program officer Larry C. Russell) and a graduate research fellowship awarded by the Department of Civil and Environmental Engineering at the Massachusetts Institute of Technology. Their support is appreciated.



# Table of contents:

1	Introduction.....	10
2	Background.....	15
2.1	Nature as a source of inspiration.....	15
2.2	Mineralized materials and hierarchical structures .....	15
2.2.1	Mineralized materials – ordering simple constituents in a tough composite	16
2.2.2	Hierarchical structures – assembling primitive building blocks at multiple scales to advanced functional materials .....	20
3	Methods.....	25
3.1	Modeling mesoscale structures – spring bead models.....	25
3.2	Material model – starting from bulk and nanoporous silica .....	27
3.3	Measuring stress in a discrete system .....	28
3.3.1	The virial theorem and the virial stress.....	29
3.4	Strain measures for discrete lattices.....	31
3.4.1	An atomistic deformation gradient .....	31
3.4.2	Moving least squares fit to displacement field .....	33
3.4.3	Virial strain vs. MLS approximation – derivation and discussion.....	34
4	Designing tough composites from simple building blocks with bio-inspired topologies	38
4.1	Introduction.....	38
4.2	Materials and the Material Model.....	39
4.2.1	Topologies and Experimental Setup .....	40
4.3	Methods.....	41
4.4	Results.....	42
4.4.1	Ordered arrangement of nanoporous silica – Decreasing sensitivity to cracks	45
4.4.2	Introduction of weak links – stabilizing fracture .....	51
4.5	Scalability of results.....	55

4.6	Conclusions.....	55
5	Designing tougher composites by elucidating simple interactions between composite constituents .....	57
5.1	Materials and Methods.....	58
5.2	Results.....	62
5.3	Discussion.....	72
6	From Computer Models to Synthesized Composites – Closing the Loop.....	73
6.1	Materials and Methods.....	74
6.1.1	Experimental approach: Synthesis.....	74
6.1.2	Experimental approach: Fracture testing .....	75
6.1.3	Material properties of base materials.....	77
6.1.4	Computational modeling.....	77
6.2	Results.....	80
6.2.1	Comparison of Computational Predictions with Experiment .....	80
6.2.2	Focus: experimentally observed fracture mechanisms .....	87
6.3	Conclusions and outlook.....	92
7	Discussion and Conclusion.....	94
8	Appendix.....	105
8.1	List of figures.....	105
8.2	List of tables.....	115

## List of journal publications:

1. L. S. Dimas, M. J. Buehler, “Influence of topology on mechanical properties of bio-inspired silica-based hierarchical materials”, *Bioinspiration and Biomimetics*, Vol. 7, paper # 036024 (2012)
2. L. S. Dimas, M. J. Buehler, “Tough and strong composites from simple building blocks”, in review.
3. L. S. Dimas, G. H. Bratzel, I. Eylon, M. J. Buehler, “Tough Composites Inspired by Mineralized Natural Materials: Computation, 3D printing and Testing”, in submission.

# 1 Introduction

Composite materials are commonly designed from building blocks with contrasting material properties with the goal of combining two attractive properties in one material system. A fundamental question in engineering composite materials for structural applications is how to design composites that effectively combine the properties of stiffness and toughness. Biologically mineralized composites such as bone, nacre, the frustules of diatom algae and deep-sea sponges are structural engineering wonders in this regard as they are assembled from simple building blocks and effectively combine high stiffness with high toughness and strength [1-10].

A large number of research efforts have focused on investigating the impressive mechanical properties of biomineralized materials in light of their hierarchical nature [1, 10-20]. Amongst other things, these studies have introduced and elucidated the importance of the cooperativity of deformation mechanisms across arrays of length scales prevalent in natural hierarchical systems. Especially, in the context of fracture, a multiscale phenomenon [21], many natural toughening mechanisms are attributed to the hierarchy of structural features spanning length scales from the nanoscale to the macroscale [1, 10, 17, 22-25]. With the advancement of computational tools, *in silico* studies have also become a popular tool used to gain fundamental insight into the design principles employed by nature in developing advanced materials from primitive building blocks [26-31]. In [26] the authors utilized finite element models to support their arguments that the nanometer size of certain structural features in mineralized structures might be a conscious design mechanism employed by nature to optimize local flaw tolerance. They predict that there exists a certain length scale at which brittle materials become insensitive to flaws, thus enabling them to reach their theoretical strength irrespective of cracks or defects. Furthermore, in [30, 31] the authors used a multiscale modeling approach, informing mesoscale models with first principles derived full

atomistic data of silica to portray a direct correlation between increased toughening behavior and number of hierarchical levels in a diatom inspired system. Theoretical analyses have also proven very valuable to further elucidate the structure-property relationships of bio-composites with several contributions highlighting the essential role of large stiffness-ratios in reducing crack tip stress concentrations in lamellar structures [32, 33].

Furthermore, a variety of other studies attribute the impressive combination of fracture toughness and stiffness exhibited by mineralized composites to other mechanisms. The more common and notable mechanisms cited include, but are not restricted to: energy dissipation and ductility through protein unfolding in the organic matrix phase [34, 35], and frictional dissipation due to shearing of mineral-organic interfaces [12, 36].

In addition to research efforts aimed at further understanding the fundamentals of strength of these mineralized composites, significant attention in the materials science research community is devoted to developing manufacturing methods with the potential of synthesizing composites with equally impressive mechanical characteristics. Since its introduction in 1992 the layer-by-layer (LBL) templating technique has been widely used for this purpose [37-41]. In [39] technique was used to create an artificial nanostructured nacre replica with strength similar to natural nacre and Young's modulus similar to that of bone. While the technique permits a fine control of structural topologies at nano length-scales, it is correspondingly demanding to utilize the approach for manufacturing macroscale structures. The thickest nacre replicas produced in [39] were 4.9  $\mu\text{m}$  thick. Furthermore, self-assembly techniques have also received great interest and the diversity of systems attainable with these methods is truly remarkable [42-45]. In [42] DNA was assembled into three dimensional nanoscale shapes while the authors in [43] used a combination of mineralization and self-assembly to create a mineral-fiber composite with a structural configuration similar to that of bone. Looking forward, while both techniques are very powerful and have the potential for a precise control of structural features at very fine length-scales, to date neither of the methods provides an outlook for large-scale cost-

effective manufacturing of complex topologies, in particular at larger hierarchical length-scales.

For many years, computers have proven an essential design tool for structural systems in the field of civil engineering. Model systems are typically conceived, subjected to the appropriate design loads and iterated upon in various computer software packages until satisfactory structural performance is obtained. Subsequently, detailed manufacturing orders are produced based on the iterated model systems and parts are assembled by separate manufacturers/contractors [46]. In this work a *de novo* complete design and synthesis approach for bio-inspired composites is proposed. Rigorous computational modeling providing fundamental insights into novel design principles for bio-inspired composites is followed by rapid manufacturing techniques producing composite structures with microscale structural features. The synthesized composites exhibiting fracture mechanical properties far superior to their individual constituents, with toughness moduli values up to 20 times than the individual constituents. Figure 1 displays the process flow of the work, from idea to design to model predictions and finally experimental results. Conclusively, the model predictions are compared with experimental results and possible improvements as well potential and impact of the methodology is discussed.

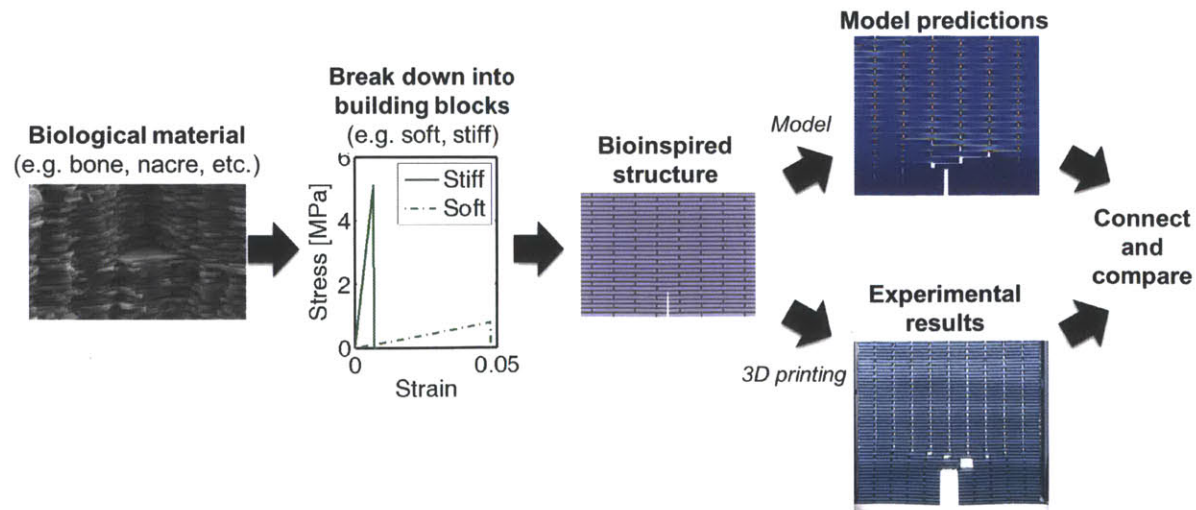


**Figure 1** Process flow of the approach used here. Starting from the simple model material building blocks composites are built with bio-inspired topologies. The bio-inspired composites are manufactured with 3D printing and proceed to test the synthesized specimens. The results are compared to model predictions. Electron microscopy image of fractured nacre surface is reprinted from <http://en.wikipedia.org/wiki/Nacre>.



By looking beyond complex and highly species-specific structural features of biomineralized materials, such as proteinaceous layers or mineral bridges, simpler interactions with key contributions to the superior stiffness, toughness and strength of biomineralized composites are identified. At some level, diatoms, bone, nacre and deep-sea sponges universally consist of more and less compliant regions arranged in specific geometries. It is hypothesized that ordering these softer and stiffer regions in specific geometrical arrangements is a powerful design principle for creating functional materials from inferior building blocks. In fact, in light of this principle it is expected that tuning and optimizing a confined number of simple geometric features of a single brittle material, e.g. silica, can produce superior materials. In Chapter 4 this hypothesis is rigorously explored with atomistically informed mesoscale spring bead models providing new insights into the influence of topological arrangement of softer and stiffer phases on the fracture mechanical response of composites.

Moreover, for a range of mineralized biological composites that combine toughness and strength, such as nacre, bone, dentin and enamel, the stiffness ratio between the stiff mineral phase and the softer organic phase is quite similar, despite the structures being composed of varying constituents [6, 47-50]. Based on these experimental findings a new hypothesis guiding further research into the fundamentals of toughness and strength of biomineralized composites is developed. Namely, the stiffness ratio, in the linear elastic regime of the constituents, controls the deformation and fracture mechanism of a composite. It is further hypothesized, that linearly elastic perfectly brittle interactions can be sufficient to lay the foundations of superior toughness in two-phase stiff bio-composite structures. A new triangular lattice spring bead model is developed, now intended to represent composites of constituents with ‘minimal cost’ constitutive behavior, *i.e.* the energy to fracture of the composite constituents is identical. Indeed, the studies show that tuning such simple constitutive behavior of the individual materials can optimize the interactions of the composite leading to fracture mechanical properties of the composites such as toughness modulus over eight times larger than for its building blocks, while retaining over 80% of the stiffness of its stiffest constituent.

Finally, to close the design loop and complete the leap from computational model to synthesized structure of bio-inspired composites, state of the art 3D printing technology is employed as a simple and effective rapid manufacturing technique to create physical artifacts of these computationally conceived systems with bio-inspired topologies. The synthesized composites exhibited structural properties similar to the presented computational systems and notably far superior to their constituents. Furthermore, the specific deformation and fracture mechanisms induced by the various topological arrangements in the experimental systems compared well to the corresponding mechanisms exhibited by the simulated composites. Moreover, key deformation mechanisms reminiscent of biomineralized structures were observed. The results indicate the possibility of designing materials in computers with tailored fracture mechanical properties and later realizing these structures with 3D printing.

## **2 Background**

### **2.1 Nature as a source of inspiration**

Through the course of history biological systems are continuously forced to optimize their design, in the context of their natural design constraints, to best persist the given environmental conditions [51]. Nature is an immense resource in terms of engineering know-how, a resource only accessible through thorough study. This has sparked the field of “Biomimicry” which in later years has assumed a very important role in a wide range of research areas [9, 52-54]. Biomimicry is as termed by Benyus in [53] “... the conscious emulation of life’s genius. Innovation inspired by nature.” Many impressive engineering feats can be directly attributed to a thorough study and emulation of ‘life’s genius’ [55-57].

While nature certainly designs complex and advanced engineering systems with impressive performance, it is as noted by Mayer in [9] essential to view natural engineered systems in light of their design constraints. Typical biocomposites such as bone, the frustules of diatomaceous algae and nacre all likely consist of the same simple building blocks, minerals and proteinaceous organics, as these are the most abundantly available. Furthermore, as typical biological materials are assembled by self-assembly their structural design is a result of minimizing energetic cost while maximizing performance [58]. Due to limited resources in demanding environments the building blocks of natural systems are commonly very primitive as compared to the materials utilized in human engineered systems. Their careful assembly is more likely to be the product of evolutionary optimization and research efforts should be directed towards understanding this aspect of their design [9].

### **2.2 Mineralized materials and hierarchical structures**

Nature is vast and there is an enormous amount of organisms and species to learn from.

As of late mineralized materials have assumed an important role in the solid mechanics community with several research efforts highlighting the impressive mechanical characteristics of these structures [1, 4, 6, 7, 16, 47, 59]. Most generally, mineralized materials are materials that are composed, fully or in part, of inorganic matter formed by mineralization, the process in which organic matter is transformed to inorganic matter. Furthermore the concept of hierarchical structures has gained increasing importance in the bioengineering community in the study of mechanical properties of biological materials [1, 5, 10, 60]. In the context of materials a hierarchical structure is one with an arrangement of structural features over a range of length scales. In the following sections mineralized materials, hierarchical structures and their impressive mechanical properties will be discussed in more depth.

### **2.2.1 Mineralized materials – ordering simple constituents in a tough composite**

Mineralized natural materials are present in nature in a variety of forms and shapes, within the field of solid mechanics much attention has been devoted to the study of bone [6, 12], mollusk shells [33, 61], deep sea sponges [1, 62] and the frustules of diatom algae [2, 8, 63]. An intriguing feature of the mentioned materials, as is highlighted in the reference works, is the primitive building blocks from which they are assembled. These are minerals that are commonly very brittle and weak [1, 16, 64, 65] and organics, typically soft and weak and assembled to a larger part by clusters of simple hydrogen bonds [66-68]. Whilst the building blocks of these mineralized structures are simple, the architectural arrangements in which they are assembled are often highly advanced.

Nacre, also known as mother of pearl, is a biological composite found on the inner layer of mollusk shells such as oyster and abalone [64]. It shares structural characteristics with the nanoscale structure of bone [10] and sponge spicule of the deep-sea sponge *Euplectella* sp. [1]. At a characteristic length scale all three of these biological mineralized composites consist of stiff mineral platelets staggered in a soft organic matrix [1, 69-73], a topological ordering similar to brick and mortar structures as seen in Figure 2. Whilst in bone this arrangement is predominant at the nanoscale in nacre and in sponge spicule it is observed at the microscale [1, 69].

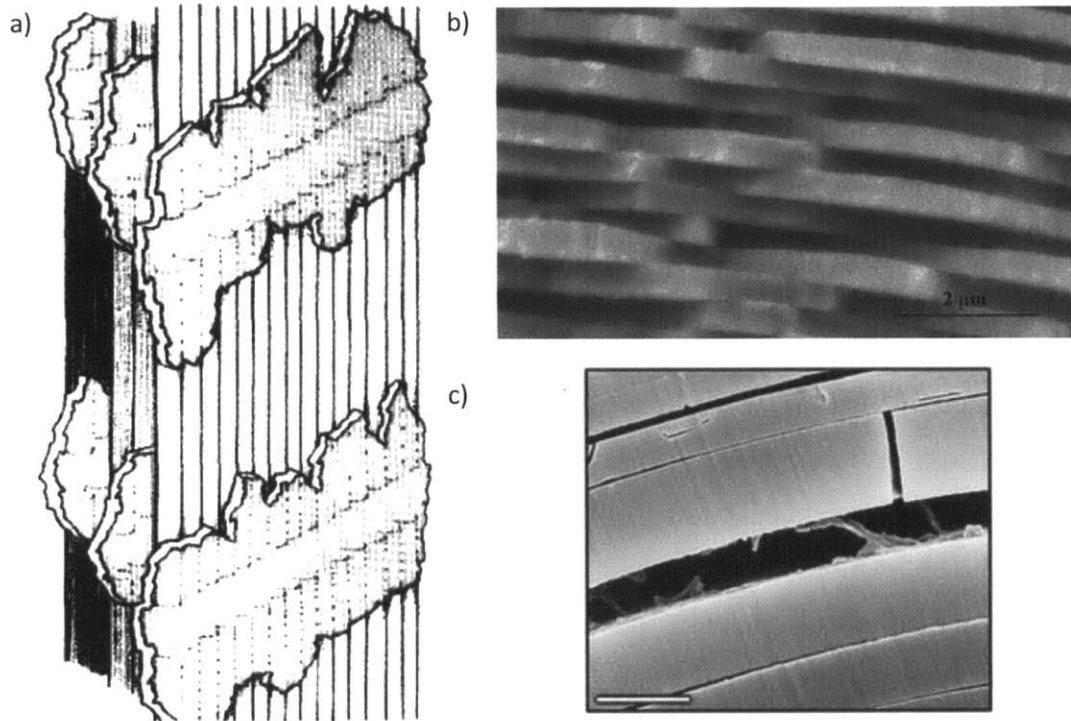


**Figure 2** (a) Schematic of the structure of bone showing plate-like crystals staggered in a collagen matrix. Figure adapted from [71], with permission from Elsevier. (b) SEM micrograph showing the staggered arrangement of aragonite platelets in nacre. A small volume fraction of organic material forms the matrix phase connecting the platelets, bar = 2 μm. Figure adapted from [69], with permission from Elsevier. (c) SEM image of a fracture spicule revealing an organic interlayer, bar = 1 μm. Figure adapted from [1], with from AAAS.

The platelets in the bone structure shown in Figure 2a are hydroxyapatite (HAp) mineral crystals, a ceramic, which are commonly known to be brittle and fracture catastrophically. The matrix phase is collagen constituting around 20 wt.% of the entire structure [74], whose mechanical properties have been studied by several groups [75, 76], and as typical for a protein is soft and extensible. Similarly the platelets in nacre are formed by the brittle ceramic aragonite ( $\text{CaCO}_3$ ) whilst the matrix phase, constituting here a mere 5 wt.% of the structure [64], again is formed of organics. Lastly, the mineral phase in the sponge spicule is composed of silica ( $\text{SiO}_2$ ), the fundamental building block of sand and glass, and again these mineral platelets are separated with a few wt.% of weak organics [1, 62].

Experimental investigations has shown nacre to be an extremely fracture resistant material; its toughness modulus is 3000 times larger than the aragonite crystals it is mainly composed of and fracture toughness values as high as  $8 \text{ MPa m}^{1/2}$  have been

reported [3, 47, 77]. Similarly groups have reported fracture toughness's of bone around  $7 \text{ MPa m}^{1/2}$  [78, 79]. These values are quite astonishing keeping in mind the large wt. % of ceramics the bio-composites are composed of. Furthermore, the structures attain these impressive fracture resistances while retaining a considerable portion of stiffness from their mineral constituent. Values of Young's modulus exceeding 100 GPa have been reported for nacre [3].

Similarly experimental investigations of the mechanical properties of siliceous composites have revealed truly fascinating mechanical properties. Levi *et. al.* [80] reported results of mechanical testing on the spicules of *Monorhaphis* sponge showing the composite to exhibit an astonishing combination of properties. The silica-based spicules dissipated large amounts of energy upon fracture, exhibited considerable stiffness and were capable of undergoing large deformations reversibly. Other deep-sea sponges with impressive mechanical characteristics include the hexactinellid sponge *Euplectella aspergillum* depicted in Figure 3a (the spicules of this structure are also depicted in Figure 2c) [1, 62]. Despite mainly being composed of the same building block as sand and glass these fascinating structures exhibit, as highlighted in the referenced work, advanced fracture toughening mechanisms such as crack blunting, crack deflection, crack arrest and stress delocalization.

In Figure 3b a variety of different structures of the silica frustules of diatom algae are pictured, exhibiting the great diversity among this class of organisms. Diatom algae are eukaryotic unicellular organisms that appear ubiquitously in aqueous environments, and they are the predominant contributors to bio-silica formation in the ocean. Despite being made primarily from this inferior building material, also the cell walls of alga exhibit mechanical properties characteristic of a highly advanced material with significant fracture toughness the main highlight as shown by recent experimental and computational work [2, 8, 27, 31, 65, 81, 82]. An interesting point to not here is that, where the structural features depicted in Figure 2 achieve a composite geometry with softer and stiffer regions by utilizing different building blocks the systems shown in Figure 3, attain a functional grading of material properties with a single building block by the use of

topology, porosity and nanoconfinement [1, 8, 81-83]. The different regions of the frustules of diatom algae show an astonishing variation of mechanical properties, Almqvist *et. al.* [2] reported elastic moduli varying over two orders of magnitude within the same siliceous frustule sample. Figure 3b clearly shows regions of varying density of porosity within the frustules thus implying a highly heterogeneous distribution of properties of within the algae cell walls.

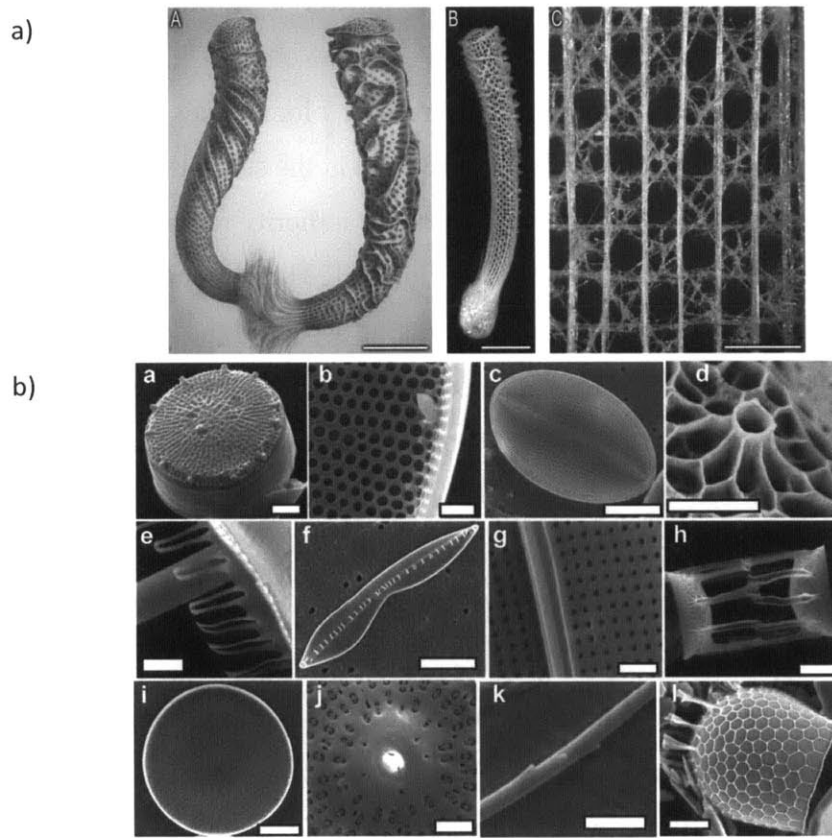


**Figure 3** (a) Details of the Western Pacific hexactinellid sponge, *Euplectella aspergillum*, and its skeleton. (A) Illustration (from Schulze, 1887) of two preserved specimens, clearly showing the holdfast apparatuses, the external ridge systems, and the terminal sieve plates. (B) Photograph of the underlying siliceous cylindrical skeletal lattice exposed by removal of the organic material. (C) At higher magnification, the square-grid architecture and regular ordering of the vertical and horizontal components of the skeletal system are clearly visible. Scale bars: A: 5 cm; B: 5 cm; C: 5mm. Figure reprinted from [62], with permission from Elsevier. (b) Images showing the broad diversity of diatom silica structures. (a) Bar = 1 μm, (b) bar = 5 μm, (c) bar = 10 μm, (d) bar = 500 nm, (e) bar = 2 μm, (f) bar = 10 μm, (g) bar = 2 μm, (h) bar = 2 μm, (i) bar = 50 μm, (j) bar = 2 μm, (k) bar = 1 μm, (l) bar = 10 μm. Figure reprinted from [81], copyright © 2007, with permission from American Chemical Society.

Figure 3, and the discussion above clearly shows that nature takes great care in the

topological assembly of mineralized structures. In fact, experimental investigations indicate that the specific architectural arrangements of the mineralized structures have been specialized for the environments the structures are exposed to. Diatoms of the type *Ellerbeckia arenaria* residing in waterfalls resist continuous stress and are able to undergo elastic deformation up to 33 % strain [84, 85] and deep-sea sponges anchored to the bottom of the ocean can also undergo large deformations without failing [1, 62].

### **2.2.2 Hierarchical structures – assembling primitive building blocks at multiple scales to advanced functional materials**

Another key structural feature amongst mineralized biomaterials is the hierarchical structure they exhibit. The term hierarchy is here used in the sense it is described in [86], as an ordered set of interrelated subsystems where no authority relation is implied. In the comprehensive works by Fratzl *et. al.* [24] and Currey [23] hierarchies in biomineralized materials are thoroughly discussed. A truly fascinating aspect of the hierarchical nature of structures in nature is the range of length scales at which the subsystems exist. In spider silk for instance, hierarchy spans over nine orders of magnitude, from nanometers to meters [87]. Here the focus will be directed towards the hierarchical structure of four mineralized structures; human vertebrate bone, nacre, the hexactinellid sponge *Euplectella sp.* and the cell walls from the diatom genus *Coscinodiscus*.

The hierarchical structure of both human vertebrate bone and the sponge *Euplectella sp.* is well documented in the literature [1, 10]. Figure 4 indicates the six hierarchical levels of vertebrate bone as identified by Rho *et. al.* [10] and Figure 5 displays the eight hierarchical levels of the glass sponge *Euplectella sp.* as identified by Aizenberg *et. al.* [1].



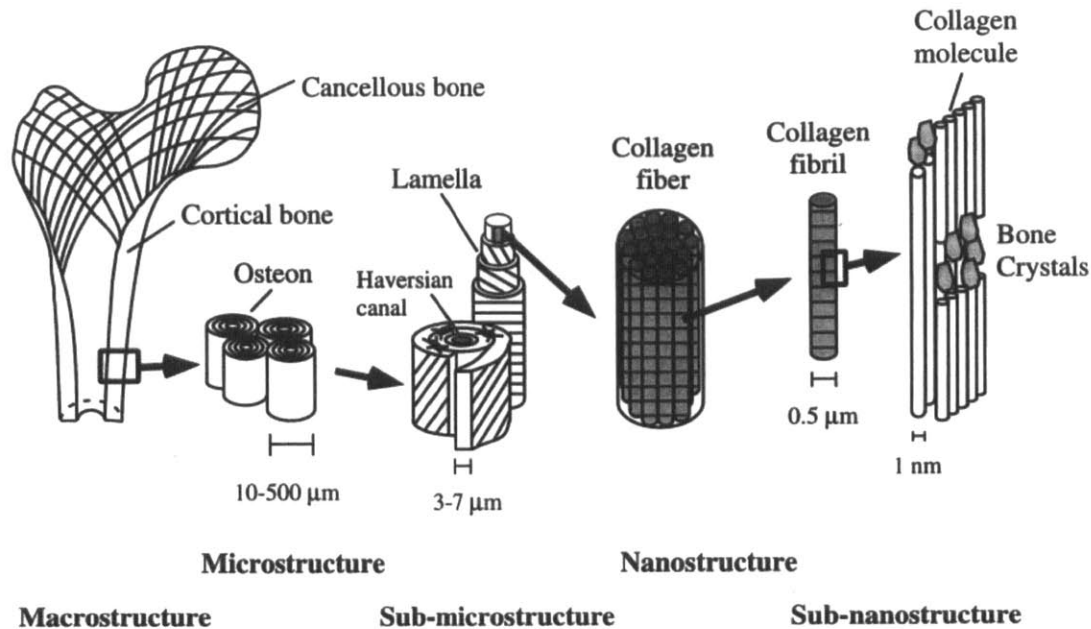


**Figure 4** Hierarchical structural organization of bone: (a) macrostructure: cortical and cancellous bone; (b) microstructure: osteons with Haversian systems; (c) sub-microstructure: lamellae; (d) nanostructure: collagen fiber assemblies of collagen fibrils; (e) sub-nanostructure: bone mineral crystals, collagen molecules, and non-collagenous proteins. Figure reprinted from [10], with permission of Elsevier.

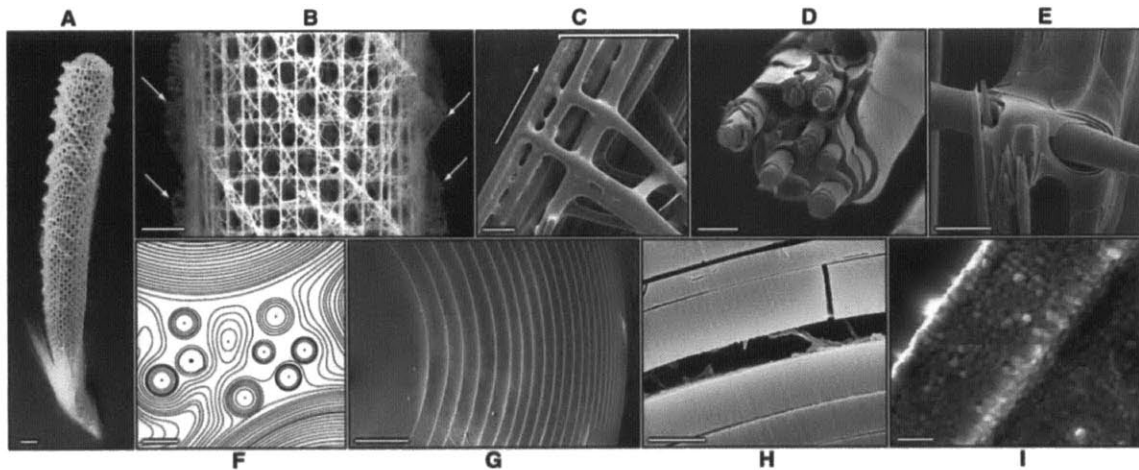


**Figure 5** Hierarchical structure of *Euplectella* sp. (A) Image of the entire structure, indicating cylindrical glass cage. Scale bar: 1 cm. (B) Close up of the cage structure portraying two square-grid lattices super imposed on each other at angled orientations. The arrows indicate stabilizing orthogonal ridges. Scale bar: 5 mm. (C) SEM image showing how each strut (enclosed by a bracket) is composed of a bundle of multiple spicules (arrow indicates the long axis of the skeletal lattice). Scale bar: 100  $\mu$ m. (D) SEM image showing the ceramic fiber-composite nature of a fractured and partially HF-etched single beam. Scale bar: 20  $\mu$ m. (E) SEM image showing the cemented nature of the HF-etched junction area. Scale bar: 25  $\mu$ m. (F) Contrast-enhanced SEM image of showing a cross section of a spicular strut. The micrograph reveals the large variety of sizes of spicule surrounded by a laminated silica matrix. Scale bar: 10  $\mu$ m. (G) SEM image of a spicule cross section, revealing the laminated structure. Scale bar: 5  $\mu$ m. (H) SEM of a fractured spicule, revealing an organic interlayer. Scale bar: 1  $\mu$ m. (I) Bleaching of biosilica surface revealing its consolidated nanoparticulate nature (25). Scale bar: 500 nm. Figure reprinted from [1], with permission of AAAS.

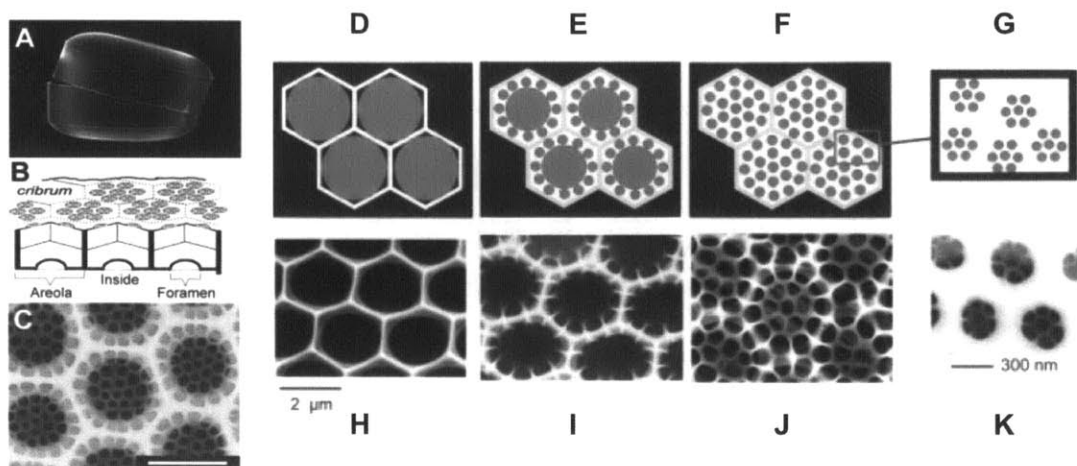


**Figure 6** (A) SEM image of a silica shell (*Coscinodiscus* sp.). (B) Schematic showing the structural set-up of the valve. (C) High-resolution SEM images of a valve seen in planar view from below (areolae, cribra, and cribella) from *Coscinodiscus radiatus*. Scale bar: 2.5  $\mu\text{m}$ . (D) to (G) shows a schematic drawing of the templating mechanism by the phase separation model proposed in [19]. (E) to (H) show SEM images of *C. wailesii* valves in the nascent state. (D) The monolayer of polyamine-containing droplets in close-packed arrangement within the SDV guides silica deposition. (E and F) Consecutive segregations of smaller (about 300 nm) droplets open new routes for silica precipitation. (G) Dispersion of 300-nm droplets into 50-nm droplets guides the final stage of silica deposition. Silica precipitation occurs only within the water phase (white areas). The repeated phase separations produce a hierarchy of self-similar patterns. Figure reprinted from [19], with permission of AAAS.

Further, although not as comprehensively described, the siliceous frustules of diatom algae also exhibit magnificent hierarchical structuring [19, 88]. Specifically, diatoms of the *Coscinodiscus* genus exhibit extraordinary silica patterning, with finely patterned arrangements of pores ranging in diameter from under 50 nm to more than 1.600  $\mu\text{m}$  [82]. In [19] Sumper presents the hierarchical structure of the *Coscinodiscus* as the self-similar silica porous patterns as shown in Figure 6. As illustrated through the figures and described in [19] the hierarchy originates from the walls of the honeycomb-like areola structure of the valve and consists of deposited silica in self-similar porous patterns of decreasing diameter. AFM imaging has further revealed that the siliceous layers are composed of silica nanoparticles, similar as for the glass sponge, thus constituting the lowest level of hierarchy [89].

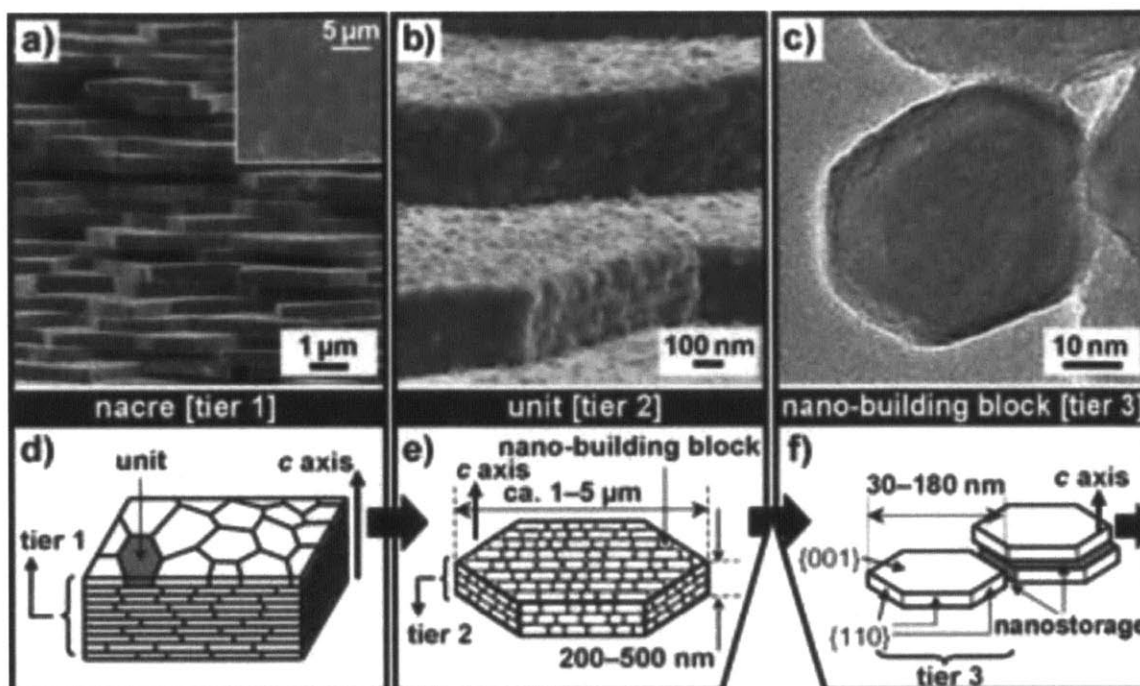


**Figure 7** Hierarchically organized structure of the nacreous layer of the Japanese pearl *Pinctada fuctata*. **a)** FESEM image of the highest level of hierarchy. Scale bar: 1  $\mu\text{m}$ . **b)** FESEM image of the second hierarchical level. Scale bar: 100 nm. **c)** FETEM image of the lowest level of hierarchy, the nano building block. Scale bar: 10 nm. Panels **d)** to **f)** show corresponding schematic drawings of the three levels of hierarchy. Figure adapted from [14], with permission of WILEY-VCH.

The fourth discussed biomineralized structure, nacre, also has a characteristic hierarchical nature; this is also a system that has been studied by several research groups, [14, 17, 18, 90]. The hierarchical structure of the nacreous layers of Japanese pearl *Pinctada fuctata* is presented [14]. Three distinct levels of hierarchy are shown in Figure 7, SEM images are presented in Figure 7a-c while Figure 7d-f show the corresponding schematic drawings. The hierarchical organization is seen to resemble a self-similar structure with the brick and mortar structure of aragonite platelets and organic interlayers repeated at progressively smaller scales from the microscale to the nanoscale over almost three orders of magnitude.

In Table 1 the various hierarchical levels of the structures introduced above are presented and summarized in an organized fashion.

**Table 1** Tabular representation of the subsystems of the hierarchical structure of the four biomineralized materials; human vertebrate bone, the hexactinellid sponge *Euplectella* sp., the siliceous frustule of the diatom algae genus *Coscinodiscus* and the nacreous layers of the Japanese pearl *Pinctada fuctata*.

Level of hierarchy	Characteristic length scale	Human vertebrate bone	<i>Euplectella aspergillum</i> (deep-sea sponge)	<i>Coscinodiscus</i> sp. (diatom algae)	<i>Pinctada fuctata</i> (nacre)
1	~ 1 nm	Collagen – HAp composite	Silica nanoparticles	Silica nanoparticles	
2	~ 10 nm	-	-	Porous structure in cribellum layer	Nano building block – hexagonal aragonite platelets (tier 3)
3	~ 100 nm	Collagen fibril	-	Porous structure in cribrum layer	-
4	~ 1 $\mu$ m	Collagen fiber	Laminated structure of silica and organic interlayer	Areola – honeycomb structure	Composite of nano building block and organic matrix (tier 2)
5	~ 10 $\mu$ m	Lamellae	Silica beams structured as ceramic-fiber composites		Nacreous structure (tier 1)
6	~ 100 $\mu$ m	Osteon with Haversian system	Bundle of spicules form struts		
7	~ 1 mm	-	Cage structure with two superimposed square grid lattices	Diatom frustule structure	
8	~ 1 cm	Cortical and cancellous bone	Hexactinellid sponge structure		

### 3 Methods

The hierarchical multiscale nature of biological materials spanning from the individual protein molecules at the nanoscale to precise the precise topological arrangement of bundles of spicules at the macroscale makes computational methods very appealing tools for their study. *In silica* studies allows access to all scales, notable also the atomistic scale, which cannot be effectively probed experimentally. While the last chapter of this thesis includes experimental work the main part of this work consists of computational investigations and thus that will be the focus of this methods chapter. Methods and models will be introduced and put into context here, while their detailed design tailored for the individual studies will be outlined in the accompanying chapters. Details on the manufacturing methods are given in this chapter while the details on the experimental testing are given in Chapter 6.

#### 3.1 Modeling mesoscale structures – spring bead models

As was outlined in Chapter 2, biomineralized materials exhibit intricate topological arrangements of softer and stiffer phases at the mesoscale. It is hypothesized here that these topological arrangements are of prime importance to the superior fracture mechanical properties exhibited by biomineralized composites and thus naturally the mesoscale plays an important role in this work. Indeed, appropriate modeling must be suitable for studying fundamental concepts of fracture at this this intermediate scale. In this work discrete lattice models are used to study mesoscale design principles of biocomposites. A schematic of a triangular lattice spring bead system is shown in Figure 8.

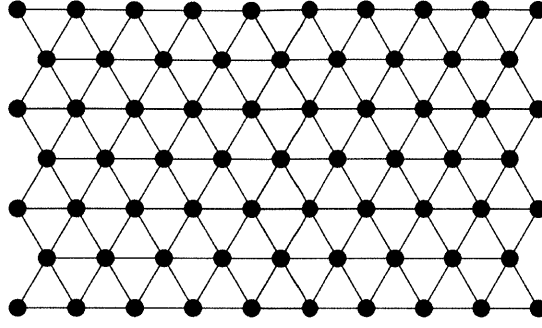


**Figure 8** Schematic overview of a spring bead triangular lattice system. The lattice is two-dimensional, matter is represented by discrete beads and the beads are connected to their nearest neighbors by springs.

Discrete lattice modeling techniques have been used widely for the study of fracture at meso length scales and have been validated by several independent research efforts [91-93]. This class of model received much attention in the late 1980's when used extensively to study the influence of randomness and disorder on the fracture behavior of various materials [94-96]. Further, in [91] in the context of fracture mechanics, triangular lattice spring bead models were shown to reproduce numerical continuum mechanical solutions for stress intensity factors in various systems. In the class of spring bead models employed here, springs, the bonds between the beads, are allowed to break if they extend beyond some critical length,  $r_c$ . This represents the initiation or growth of a crack and the system will fail if a crack, the breaking of bonds, percolates through the network. Two key features make this class of models attractive for use here. First of all, cracks are represented in a very intuitive way, simply as the breaking of bonds. Moreover, no explicit crack propagation criteria is required, this follows naturally as the breaking of bonds. These properties of the spring bead system provide significant advantages over conventional finite element methods where the propagation of cracks is a far more complex matter. Furthermore, despite their apparent simplicity triangular lattice spring bead models have a documented agreement with and good representation of continuum fracture mechanics concepts.

The respective phases of the investigated composites are modeled as homogeneous and thus the systems studied could be characterized as represented by an ordered heterogeneity. Similarly to the representations in [94-96] the beads represent a group of smaller particles/molecules, however in the current system the beads are assumed to be



large enough to neglect intrinsic disordered heterogeneity.

### 3.2 Material model – starting from bulk and nanoporous silica

Initially the goal is to show that tough composites can be assembled from the most brittle of building blocks simply by utilizing geometries as an active design tool. Thus the mesoscale model is informed with first principles derived full atomistic data on the constitutive behavior of two distinct forms of silica (the fundamental constituent of glass), bulk silica and nanoporous silica. This specific coarse-grained model is developed in [30] and is based on the atomistic simulations described in [97]. Excerpts of the results of this study are presented in Figure 9 showing the contrasting stress strain response of bulk silica and a nanoporous silica sample. The nanoconfinement of the silica structure induces a compliant and ductile response.

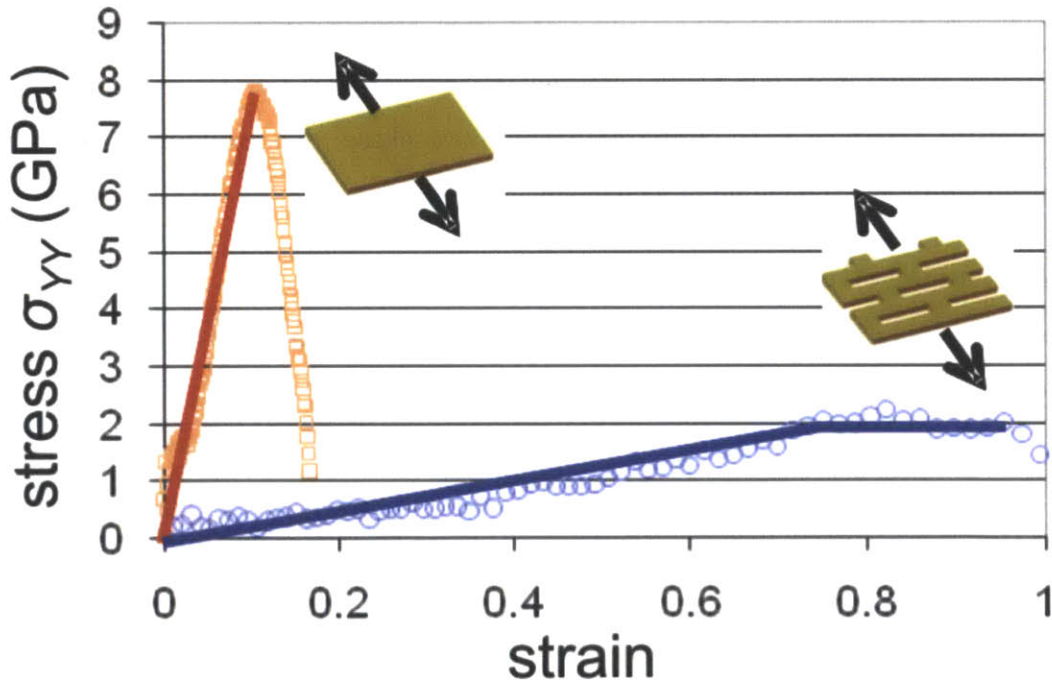


**Figure 9 (a)** ReaxFF derived stress-strain response for two of the tested geometries in [97], bulk silica and nanoporous silica with sidewall thickness  $w$  of 17 Å. Solid lines indicate lines of best fit. Figure adapted from [97] and reprinted with permission from the Nature Publishing Group.

The constitutive behavior displayed in Figure 9 is used to train the discrete particle lattice system shown in Figure 8 by application of the Cauchy-Born rule [30, 98, 99]. Further, to ensure a separation of scales between the atomistic simulations and the mesoscale simulations the equilibrium spacing between particles in Figure 8 was chosen to be 78

nm. Thus a mesoscale model was developed, containing first principles based full atomistic information, capable of simulating micrometer length scales. Once the influence of topologies has been extensively studied, new material models are designed and utilized in this work to explore further research questions. These are treated separately in the corresponding chapters.

As the models presented in this work are meant designed to highlight individual fundamental design mechanisms it is imperative that they are simple. Several interesting studies on mineralized structures attribute toughening mechanisms to interfacial sliding effects occurring at the interface of soft organics and the brittle mineral crystals [100]. However, this mechanism is not a focus in this work and thus the models are designed such as to exclude this effect. Therefore the adhesion at the interfaces of the system between the bulk and nanoporous silica (for the primary study and between the corresponding model materials for the subsequent studies) is chosen to be perfect. This implies that the interface is as strong as the weakest phase, thus excluding interfacial failure as an additional toughening mechanism.

### **3.3 Measuring stress in a discrete system**

Traditionally, stress has been most commonly utilized as a measure of loading in a continuous system. The Euler-Cauchy stress principle states,

*“Upon any surface (real or imaginary) that divides the body, the action of one part of the body on the other is equivalent (equipollent) to the system of distributed forces and couples on the surface dividing the body.”*

The internal forces across such a real or imaginary surface normalized by the area of said surface are exactly equal to the average of the internal stresses acting over said surface. As surfaces are more easily envisioned in continuous systems, the notion of stress is also more intuitive in regards to continuous matter. However, with the increased use of molecular dynamics accompanied by the larger focus on the nanoscale, discrete systems are becoming more commonplace. Moreover, along with the ambition to couple and exchange information between discrete systems and continuous systems, stress measures



have become an important concept also in particle mechanics. Specifically, focus has been directed towards developing a formulation of stress in a discrete system that can be proven equivalent to a continuous stress measure. To this end, the virial stress measure introduced by Tsai [101] has proven to be of great use.

### 3.3.1 The virial theorem and the virial stress

Initially introduced by Clausius in 1870 the virial theorem provided a link between the pressure and the potential energy of a homogenous discrete particle system in equilibrium. Over one hundred years later, in 1978 Tsai showed that identical results for the pressure calculation could be achieved by analyzing a stress like quantity that was subsequently termed the virial stress [101]. The measure introduced has a simple interpretation, which will be outlined below, and is understood neatly in connection with the conventional continuum Cauchy stress.

In this presentation of the virial stress it will be introduced as the superposition of two distinct terms and is thus written as

$$\sigma_{ij} = \sigma_{ij,1} + \sigma_{ij,2}. \quad (1)$$

The individual terms are due to distinct interactions and are more easily conceived separately. Figure 10 shows a cartoon of an imaginary surface across which particles interact and the virial stress is evaluated.

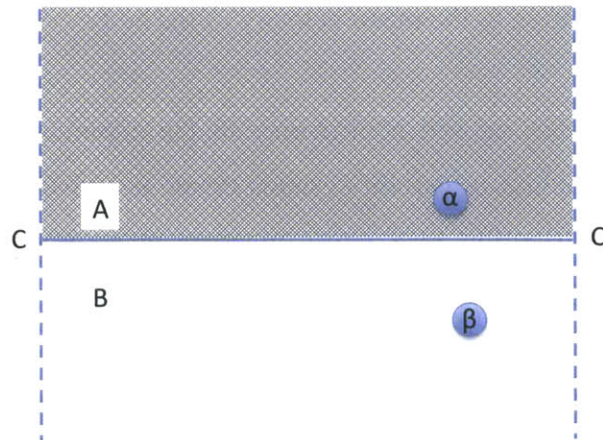


**Figure 10** Schematic indicating two particles,  $\alpha$  and  $\beta$ , interacting across an imaginary surface  $CC'$  at which the virial stress is evaluated.

The first of the two contributions to the virial stress,  $\sigma_{ij,1}$ , is the static equilibrium term derived from the virial theorem by Clausius. This contribution accounts for the forces acting between atoms across a certain surface and is expressed as follows

$$\sigma_{ij,1} = \frac{1}{2V} \sum_{\alpha, \beta, \alpha \neq \beta} \left( \frac{\partial \phi(r)}{\partial r} \frac{r_i}{r} r_j \right). \quad (2)$$

Here,  $V$  denotes the volume of the considered atomistic system, Greek letters alpha and beta are used to indicate atoms, subscript Roman letters are used to indicate the coordinate direction,  $\phi$  represents the interatomic potential and  $r$  indicates the radial distance from the center of mass of an atom. In a system in equilibrium such as the one analyzed by Clausius, where the mean velocity of the ensemble of particles is zero, this term fully accounts for the system pressure.

The second contribution to the virial stress comes in to effect in non-equilibrium systems, systems experiencing a net force. Specifically, in connection with the schematic in Figure 10 this term accounts for the forces exerted across the surface  $CC'$  due to momentum flux imparted by particles crossing the boundary and it is expressed as

$$\sigma_{ij,2} = -\frac{1}{V} \sum_{\alpha} m^{(\alpha)} v_i^{(\alpha)} v_j^{(\alpha)}. \quad (3)$$

Here,  $m^{(\alpha)}$  denotes the mass of atom  $\alpha$  while  $v_i^{(\alpha)}$  is the velocity of atom  $\alpha$  in the  $i$  coordinate direction relative to the mean velocity of the body.

This last kinetic term has caused controversy in the community and in [102] it was claimed that this term could in certain systems create negative stresses and was in fact non-physical as a contribution to a stress measure in a discrete system. Subsequent research efforts presented arguments claiming to disprove this view and in support of the virial stress as a stress measure equivalent to the continuum Cauchy stress [103, 104]. Furthermore, [103] computational simulations on full atomistic models were conducted supporting the virial stress as a discrete equivalent to the Cauchy stress. By regarding the kinetic term of the virial measure in the light in which it was presented here, as a momentum flux term, it is readily realized that this term is necessary to account for all force interactions across boundaries in the system. Moreover, it makes perfect physical

sense in a system where particles have non-zero velocities relative to the ensemble velocity of the system. It is further noted that the virial stress converges to the continuum measure only when averaged in space, hence only in microscopically large systems.

### 3.4 Strain measures for discrete lattices

As well as measuring local stresses in a discrete system it is desirable to be able to measure and track the local variations of local strain in a discrete system. Characterizing strains can provide many insights and educate about mechanisms occurring at the atomistic scale. Further, in order to have an effective framework in which the atomistic scale can be coupled with the continuum scale it is essential to have a consistent measure of strain that can create a bridge between the two approaches.

Two different descriptions of strains for discrete particle systems are presented in the following subsections. The descriptions are accompanied by examples and some discussion of their respective advantages and disadvantages. It is noted that the presented measures are, with certain exceptions (to be clarified), valid for general discrete systems, both atomistic and coarse-grained particle systems alike.

#### 3.4.1 An atomistic deformation gradient

In continuum mechanics deformation is conventionally characterized by relating the current configuration of a body to its reference configuration [105, 106]. The location of a point on a body in the undeformed configuration is typically denoted by an uppercase  $\mathbf{X} = \{X_1, X_2, X_3\}$  while the location of the same point in the deformed configuration is denoted by  $\mathbf{x} = \{x_1, x_2, x_3\}$ . The deformation can thus be characterized by relating the location of a point in the two different configurations through a mapping  $\mathbf{x} = \mathbf{x}(\mathbf{X}, t)$ . The derivative of this mapping with respect to the undeformed configuration is called the deformation gradient,

$$\mathbf{F} = \partial \mathbf{x} / \partial \mathbf{X}. \quad (4)$$

The deformation gradient in turn, serves as the basis of many strain measures [107]. In the past ten or so years several groups have approached the challenge of defining a continuum compatible atomistic strain by defining an atomistic deformation gradient, two of these groups arrived at very similar results [108, 109]. The expression developed by

Zimmerman and coworkers in [109] will be the one presented here. Further, the strain developed through this method will be subsequently termed the virial strain.

By assuming small displacements, including only the linear term in the Taylor expansion of the deformation gradient, and noting that the smallest measurable distance in the system is the distance to a neighboring atom, the equation for the deformation gradient in discrete system can be rewritten as

$$x_i^{\alpha\beta} - F_{ij}X_j^{\alpha\beta} = 0. \quad (5)$$

Here  $x_i^{\alpha\beta}$  and  $X_j^{\alpha\beta}$  represent the distance between atom  $\alpha$  and  $\beta$  in the deformed and reference configuration for coordinate direction  $i$  and  $j$  respectively. It is noted in [109] that this relation can only hold exactly for a single neighbor of a particular atom, thus it is required that the sum of squares of the errors for all neighboring atoms is a minimum. Further, performing some algebra on the least squares expression the following expression for the deformation gradient is obtained

$$F_{ij}^\alpha = \omega_{iM}^\alpha (\eta^\alpha)^{-1}_{Mj}, \quad (6)$$

where

$$\omega_{iM}^\alpha = \sum_{\beta=1}^n x_i^{\alpha\beta} X_M^{\alpha\beta}, \quad (7)$$

and

$$\eta_{jM}^\alpha = \sum_{\beta=1}^n X_j^{\alpha\beta} X_M^{\alpha\beta}. \quad (8)$$

Here  $n$  represents the number of nearest neighbors of the atom in question and again Greek letters indicate atoms while Roman letters indicate coordinate directions.

While this expression only considers displacements relative to nearest neighbors the expression developed by Horstemeyer and coworkers [108] also considers displacements relative to particles that are not nearest neighbors. The contribution of these displacements is controlled by the introduction of a weighing function that commonly decreases as more distant neighbors are considered. The formulation derived by Zimmerman *et. al.* can be viewed as a special case of that derived by Horstemeyer *et. al.*

where the weighing function is unity for nearest neighbors and vanishes for all other neighbors.

The functional form of weighting functions and cut-off radius affect the value of the computed strain and especially has an influence near strain localizations [110]. In the form in which it is presented here the deformation gradient has been shown to comply with the essential compatibility requirements enforced through continuum mechanics [109].

### 3.4.2 Moving least squares fit to displacement field

In an effort to create a framework for analyzing coupled atomistic-continuum systems Belytschko and coworkers developed what they termed a moving least squares (MLS) approximation to the displacement field in discrete systems [111, 112]. In short, the MLS scheme creates a continuous displacement field by interpolating the displacements of particles. With an appropriate finite difference scheme the displacement field can be utilized to compute an appropriate deformation gradient and any desired strain measure. The method will be presented in brevity below in accordance with its presentation in [112].

With the MLS approximation the displacement at *any* point  $\mathbf{x}$  is described by the continuous function

$$\mathbf{u}(\mathbf{x}) = \sum_{i=1}^m p_i(\mathbf{x}) \mathbf{a}_i(\mathbf{x}). \quad (9)$$

Here  $m$  is the number of basis functions  $p_i(\mathbf{x})$  and  $\mathbf{a}_i(\mathbf{x})$  are vector coefficients computed from the moving least squares approximation, to be described below. This form of expressing the displacement is similar to the methodology in continuum finite element methods; the basis functions  $p_i(\mathbf{x})$  can be regarded as equivalent to interpolation functions in FEM. The polynomial order of the basis functions is chosen based on desired order of the displacement function. The vector coefficients  $\mathbf{a}_i(\mathbf{x})$  are found by minimizing the weighted  $L_2$ -norm,  $q(\mathbf{x})$ , of the displacement field  $\mathbf{u}(\mathbf{x})$  and is given by the expression

$$q(\mathbf{x}) = \sum_{\alpha \in S_{\mathbf{x}}} (p_i(\mathbf{x}_{\alpha}) \mathbf{a}_i(\mathbf{x}) - \mathbf{u}_{\alpha})^T w^{mls}(\mathbf{x}_{\alpha} - \mathbf{x}) (p_j(\mathbf{x}_{\alpha}) \mathbf{a}_j(\mathbf{x}) - \mathbf{u}_{\alpha}). \quad (10)$$

In this expression a sum is implied over the repeated indices  $i$  and  $j$ , the total summation is performed for all atoms within the support  $S_{\mathbf{x}}$  and  $w^{mls}(\mathbf{x}_{\alpha} - \mathbf{x})$  is a weight function over the support region. The weight functions can assume many different forms and have a significant impact on the performance of the solution field, in general they should have large values close to the treated atom at point  $\mathbf{x}$  and smaller values for points further away. The support region is the region over which relative displacements are considered for a given atom and its size is commonly be tailored depending on the application [111].

### 3.4.3 Virial strain vs. MLS approximation – derivation and discussion

Now the respective methods for evaluating strain are tested, discussed and compared. First, however the expressions must be developed from the equations presented earlier.

#### 3.4.3.1 Derivation of expressions

Starting with the virial strain, appropriate algebraic manipulation of the deformation gradient leads to the following convenient expression for the left Cauchy Green tensor  $\mathbf{B} = \mathbf{F}\mathbf{F}^T$  for atom  $\alpha$

$$B_{ij}^{\alpha} = \frac{1}{\lambda} \sum_{\beta=1}^N \left( \frac{\Delta x_i^{\alpha\beta} \Delta x_j^{\alpha\beta}}{r_0^2} \right). \quad (11)$$

Here  $N$  indicates the number of nearest neighbors and  $\Delta x_i^{\alpha\beta} = x_i^{\beta} - x_i^{\alpha}$  and  $\Delta x_j^{\alpha\beta} = x_j^{\beta} - x_j^{\alpha}$  with  $x_i^{\alpha}$  signifying the  $i$ -th component of the coordinates of atom  $\alpha$  in the deformed configuration. Further,  $r_0$  is the equilibrium spacing of the lattice and  $\lambda$  a prefactor depending on the specific lattice chosen. For the employed triangular lattice with only nearest neighbor interactions it is given in [109] that  $\lambda = 3$ . It is noted that the left Cauchy-Green tensor is conveniently expressed solely in terms of the current positions of particles in contrast to the more involved expression for the deformation gradient  $\mathbf{F}$  as presented earlier.

Now, for the description of strain an engineering strain measure is employed, specifically

$$\boldsymbol{\varepsilon} = \sqrt{\mathbf{B}} - \mathbf{1}. \quad (12)$$

Here,  $\mathbf{1}$  is the identity tensor and the square root of  $\mathbf{B}$  is well defined in terms of its eigenvalues and eigenvectors, as it is a symmetric positive definite matrix

$$\sqrt{\mathbf{B}} = \sum_{i=1}^3 \sqrt{w_i} \mathbf{e}_i \otimes \mathbf{e}_i, \quad (13)$$

where

$$\mathbf{B} = \sum_{i=1}^3 w_i \mathbf{e}_i \otimes \mathbf{e}_i, \quad (14)$$

and  $w_i$  and  $\mathbf{e}_i$  are the eigenvalues and eigenvectors of the left Cauchy-Green tensor, respectively.

As for the description of strain through the MLS-approximation of the displacement field the employed weight functions  $w^{mls}$  are first presented. These weight functions are the same as those suggested in [112] and are expressed as

$$w^{mls}(r) = \begin{cases} \frac{2}{3} - 4r^2 + 4r^3 & \text{for } r \leq \frac{1}{2}, \\ \frac{4}{3} - 4r + 4r^2 - \frac{4}{3}r^3 & \text{for } \frac{1}{2} < r \leq 1, \\ 0 & \text{for } r > 1. \end{cases} \quad (15)$$

Here  $r$  is naturally the radial distance from the center atom. It is readily recognized that the given functional expression fulfills the requirements as outlined above. Further, linear basis functions are implemented and the support is restricted to four times the nearest neighbor distance as also suggested in [112]. Again an engineering strain measure is employed to characterize the strain field and the following familiar expressions are retrieved

$$\begin{aligned} \varepsilon_{xx} &= \frac{\partial u_x}{\partial x}, \varepsilon_{zz} = \frac{\partial u_z}{\partial z}, \varepsilon_{xz} \\ &= \frac{1}{2} \left( \frac{\partial u_x}{\partial y} + \frac{\partial u_y}{\partial x} \right). \end{aligned} \quad (16)$$

The derivatives are evaluated numerically with central differences as shown below for  $\partial u_x / \partial x$ ,

$$\left. \frac{\partial u_x}{\partial x} \right|_{x=x_i} \approx \frac{u_x|_{x=x_{i+1}} - u_x|_{x=x_{i-1}}}{2 \cdot h_x}. \quad (17)$$

### 3.4.3.2 Discussion

The test case that is used is a linear elastic model material, with and without a notch, subjected to pure longitudinal tension. The resulting longitudinal strain field plots are plotted with MATLAB and presented in Figure 11. As expected the longitudinal strain field is perfectly uniform with both descriptions for the unnotched case. Furthermore, both strain descriptions correctly allow the formation of a strain concentration around the crack tip in the notched case. Moreover, inspecting the respective coloring a very good quantitative correspondence is observed for the two descriptions. Now that the correspondence for this test case has been documented some details of the implementation of the two approaches are discussed.

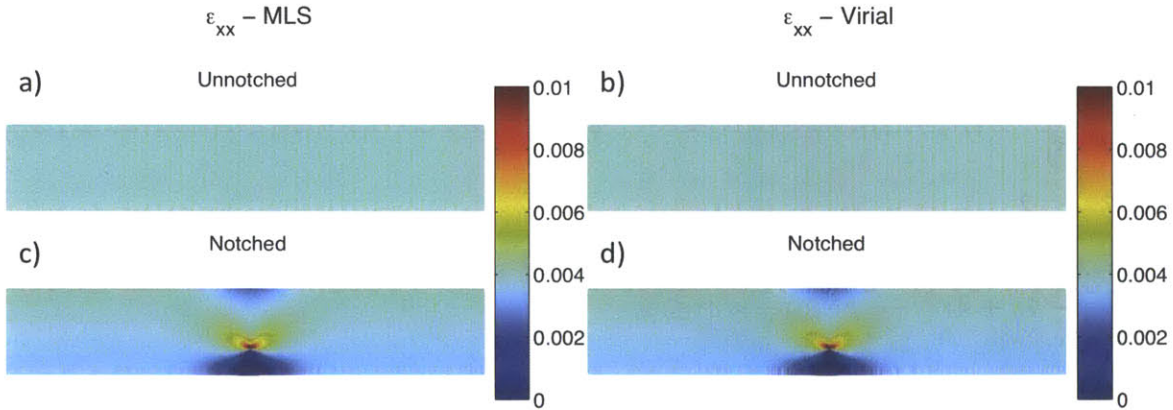


**Figure 11** Comparison of longitudinal strain fields from the MLS and virial description. **a)** MLS derived strain field for unnotched case, **b)** virial strain field for unnotched case, **c)** MLS derived strain field for notched case, **d)** virial strain field for notched case. The field plots show very good agreement indicating that the MLS description of displacements and virial strain agree well in terms of longitudinal strain.

The main difference between the two methods for the tested case lies in the computational effort. The virial strain description only considers the positions of nearest neighbors and thus the strain field is computed far more efficiently with this method. Reducing the size of the support region in the MLS-approximation to the displacement field can reduce the computing time significantly; however, it does this at the expense of the stability of the approximations. Support regions with radii of less than three lattice spacing's commonly lead to expressions with ill-conditioned matrices. Albeit computationally more intensive, the MLS method seems more appropriate for the



analysis of systems with discontinuities such as surface boundaries, material interfaces and cracks. The MLS-method is not constrained to systems with specific configurations or lattice structures and the support region can be tailored such as to express the displacement field around any particular particle surround by a host of discontinuities in a robust manner. For systems more involved than the one presented here, e.g. an amorphous solid, it is clear that the virial strain as derived by Zimmerman in [109] would be inapplicable whereas the MLS-approximation to the displacement field remains equally useful.

## **4 Designing tough composites from simple building blocks with bio-inspired topologies**

The previous discussion of bio-mineralized materials highlighted the heterogeneous distribution of their mechanical properties. Moreover, several examples were given illustrating careful arrangements of regions with distinct constitutive behavior in complex architectures. As studies of a variety of bio-mineralized structures has revealed these characteristics to be common for a range of biological mineralized materials in different environments it is interesting from a materials scientist's and structural engineers point of view to study these features in light of them being advanced design principles. Computational investigations at the micro-scale gain novel insights into the mechanics of bio inspired composites.

### **4.1 Introduction**

An intriguing characteristic of some well-studied mineralized materials such as nacre, bone, frustules of diatom algae and deep-sea sponges, is that they all, at some length scale, are composite materials consisting of stiff, less extensible regions and soft, deformable regions. The hypothesis to be explored here is that that ordering these softer and stiffer regions in specific geometrical arrangements is a powerful design principle for creating functional materials from inferior building blocks.

This study shows that the inclusion of a deformable nanoconfined silica phase in bulk silica structures can be sufficient if introduced and distributed in an appropriate manner. By studying the mechanisms of deformation and failure of model materials insights are gained in the detailed mechanisms by which deformable and brittle regions interact to form a fracture resistant composite, and which details of their structural configuration make their interaction advantageous for meso- and macroscale structures. Finally it is argued that the compliance of the second phase is the key attribute enhancing the overall

mechanical behavior of the composite and the specific mechanisms by which the response is enhanced depends on the geometrical configuration of the deformable phase.

## **4.2 Materials and the Material Model**

The specific model to be utilized in this study is the one outlined in Section 3.2 and it was designed and selected for use here with precise intentions. The simplicity of the model is a great strength and its key feature. The current study is aimed towards elucidating one specific design principle employed by nature in its assembly of bio-mineralized structures; the use of architecture and specific topological arrangements of softer and stiffer regions to create functional composites. Arrays of hierarchies, proteinaceous layers and interfacial effects which have all previously been claimed to be key for fracture resistance in mineralized materials, [29, 31, 36], are excluded from the model employed here in order to exclusively study the effect of geometry in an intelligible manner. All systems contain the same number of hierarchical levels. Secondly, the single building block of the composite system is the primitive silica, it occurs in bulk and nanoconfined form giving rise to two fundamentally different constitutive behaviors, see Section 3.2 and specifically Figure 9. Organic interlayers with hidden length, undergoing viscous deformation and dissipating vast amounts of energy are not included. Finally, the interfaces of the composite system are perfectly bonded and thus no dissipation occurs due any interfacial effects.

At this point it is important to highlight the following; it is not claimed that the listed mechanisms don't enhance material performance. On the contrary, as was also outlined in previous chapters, nature employs an array of structural features enabling an array of mechanisms to achieve desired material performance. However, it is hypothesized that also the very simple design mechanism of ordering phases with different constitutive behaviors can have a large impact on the meso- and macroscale material behavior and can be used to tailor material response. Moreover, in order to effectively prove the validity of this hypothesis it is seen as a necessity to utilize the simple model described.

### 4.2.1 Topologies and Experimental Setup

In order to study the influence on mechanical properties of the careful geometrical arrangement of softer and stiffer phases, four different intelligible topologies are chosen for investigation. First, as a benchmark, a bulk silica system is characterized. Thereafter, as pictured in Figure 12 a bio-calcite-like system Figure 12a, a bone-like system Figure 12b and a rotated bone-like system Figure 12c are also studied.

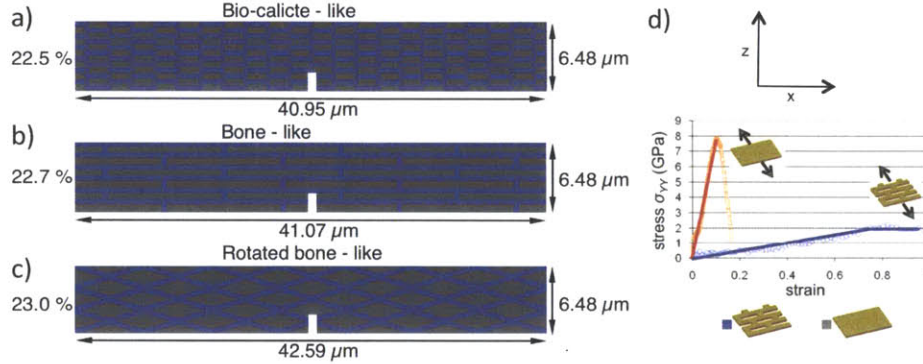


**Figure 12** Geometries of specimens, here shown with size parameter  $h = 6.48 \mu\text{m}$ . With the blue and gray phases representing the nanoporous and bulk silica, respectively, for (a) the bio-calcite-like geometry, (b) the bone-like geometry and (c) the rotated bone-like geometry. The specimens are loaded by imposing stepwise displacement on their right vertical faces, whilst holding the left hand sides still. Periodic boundary conditions are employed in the horizontal direction. (d) Constitutive laws for the nanoporous and bulk silica phase representing the compliant and brittle phase respectively in the material model (adapted from [31] with permission from Nature Publishing Group).

The two first geometries are examined for their simplicity and contrasting nature. The bio-calcite-like comprising of soft platelets dispersed in a stiff matrix and the bone-like consisting of stiff platelets staggered in a compliant matrix. These differences are hypothesized to define the fundamental mechanics of the structures, changing methods of longitudinal and shear, stress and strain transfer and thus having large implications on sensitivities to cracks and size dependences of strength. The third, rotated bone-like, geometry is included in an attempt to optimize strain transfer through the structures. By providing a continuous path for longitudinal strain transfer, it is hypothesized that one can induce ductility of the structure and eliminate the catastrophic nature of failure commonly associated with silica.

The mechanical characteristics of the geometries are tested by introducing initial cracks at midsection extending through a fourth of the height of the specimens (constant notch

length to sample size ratio) and loading them until failure. To investigate size dependences, crack sensitivities and the up scaling of strength four different size parameters for the specimens are chosen: 2.16, 6.48, 23.78 and 36.75  $\mu\text{m}$ . The lengths of the specimens and their volume fractions of the soft phase are indicated in Figure 12. The geometries were created such as to keep these parameters as similar as possible and the inescapable disparities present are viewed as within an acceptable bound such that the geometries and results are comparable.

The mechanical behaviors of the composites are a function of the volume fraction of the soft phase. Increasing the volume fraction of the soft phase naturally shifts the behavior of the composites towards that of the nanoporous silica while decreasing the volume fraction of the soft phase makes the composites behave more similar to bulk silica. A target volume fraction of around 20% is chosen with the aim of creating a composite that can combine the attractive mechanical features of both its constituents; thus combining appreciable stiffness, strength and fracture resistance. It is noted that the employed volume fraction was not tuned to form a composite with the optimal combination of these characteristics; rather a volume fraction was chosen that was believed to satisfy the given requirements.

The loading is introduced by applying a displacement boundary condition on the right vertical face and holding the left vertical face fixed, a simple tensile test is performed. After each displacement increment, the equilibrium positions of the beads are found by means of a conjugate gradient energy minimization technique. Hence, static loading is simulated. Furthermore, to avoid longitudinal size effects, periodic boundary conditions are employed in the  $x$ -direction whilst the surfaces facing the  $z$ -direction are free. Stress and strain data are calculated at each displacement increment by recording positions of the beads throughout the deformation.

### **4.3 Methods**

The simulations are conducted with the molecular dynamics package LAMMPS. The virial stresses as introduced above formed the basis of the stress analysis in this study. Virial stresses are output from LAMMPS and the quasi-static nature of the simulation

implies that only non-zero term is the static term with forces derived from the inter-particle potential (the inter-particle potential, force field, is back calculated from the constitutive behavior of the respective phases by integration). The LAMMPS package calculates stresses without dividing the expressions by atomic/particle volumes, output units for the presented study are  $\text{atm} \cdot \text{\AA}^3$ , and thus this must be done as a post-processing step as well as any unit conversions. Here stresses will be presented in MPa. For the analysis of strains the virial strain measure is employed due to its simple and rapid evaluation in the current system.

The computed stresses and strains are evaluated by visualization of stress and strain fields plotted in MATLAB. Stress and strain fields represent an important analysis tool in this study as they provide insight into the mechanisms of deformation and failure of the materials. These field plots can also provide insight into the role of the soft phase and its geometrical configuration in the context of strain and stress transfer. It should be noted that strains in the immediate vicinity of the crack tip might be inaccurate due to the inhomogeneity of deformation fields in this region. However, it is argued that the toughening mechanisms are mainly encountered away from the crack tip and hence the strain plots are meaningful. Finally, a global longitudinal strain is also defined for the purpose of characterizing the stress-strain response of the entire structure. Consistently with previously employed strain measures an engineering strain measure is chosen for this purpose, defined as

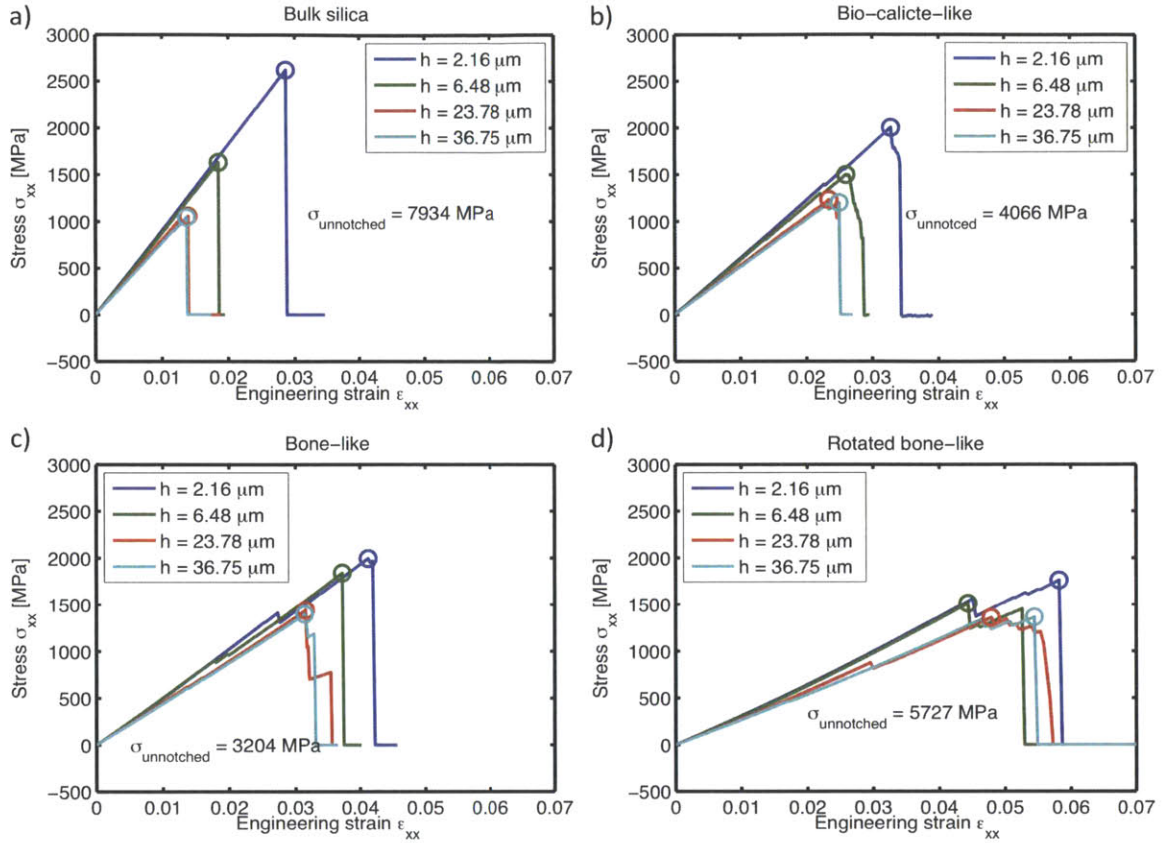
$$\epsilon_{xx} = \frac{\Delta L}{L_0}. \quad (18)$$

#### 4.4 Results

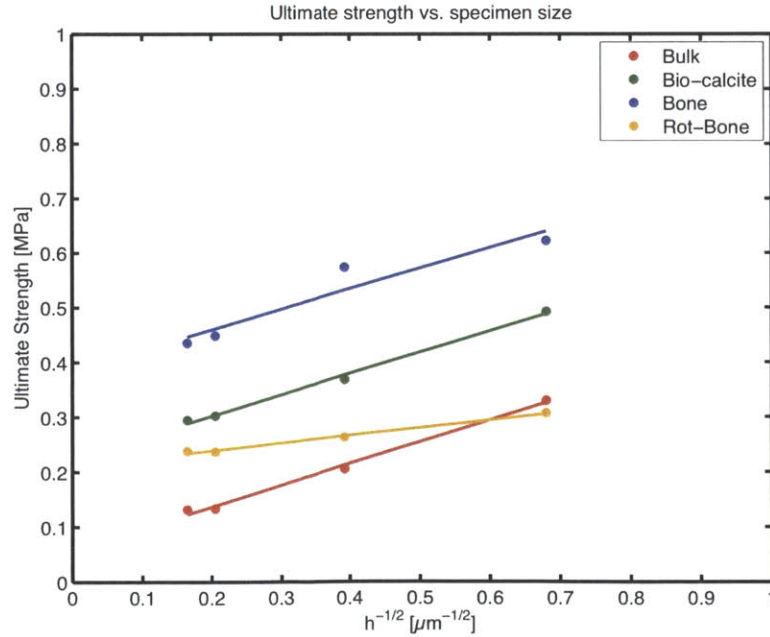
Stress versus strain trajectories of the loading, up to and including failure, of all four sizes of the four geometries is presented in Figure 13. Further, Figure 14 shows the normalized strength plotted versus the inverse square root of the size parameter of the specimens for all specimens tested. Here the stresses are normalized by the ultimate stresses for the respective unnotched specimens.

Figure 13 indicates that the bulk-silica system, the benchmark, behaves perfectly elastic up to a limiting strain at which point it fails in a brittle manner. Furthermore, the limiting strain/strength is seen to be strongly dependent on the size parameter. Comparing this behavior with that exhibited by the composites in Figure 13 and Figure 14 strong indications are given that the hierarchical topologies can significantly alter and enhance the mechanical performance of a material. Among other characteristics all three hierarchical systems exhibit a decreased size-dependency of strength. Furthermore the rotated bone-like specimens are seen to experience a yielding like behavior prior to failure through a deformation period of negligible stiffness. The stress-strain trajectories of the rotated bone-like samples seem to indicate that the composites fail in a stable fashion. Moreover, Figure 13 indicates that the composites maintain appreciable stiffness and strength with the humble volume fraction of compliant nanoporous silica chosen. Further considering Figure 14, the strengths of both the bio-calcite-like and bone-like geometry show a significantly lesser sensitivity to the presence of the crack.

In order to gain a more fundamental understanding of the mechanisms controlling the responses exemplified in Figure 13 and Figure 14, stress and strain field plots are plotted and investigated.



**Figure 13** (a) Stress-strain response for the bulk silica specimen, (b) the bio-calcite-like specimen, (c) the bone-like specimen and (d) the rotated bone-like specimen. Circular markers indicate the points at which the ultimate stress snapshots are taken.



**Figure 14** Normalized strength as a function of specimen size for all four investigated systems. The strengths are normalized with respect to the respective strengths of the unnotched samples.



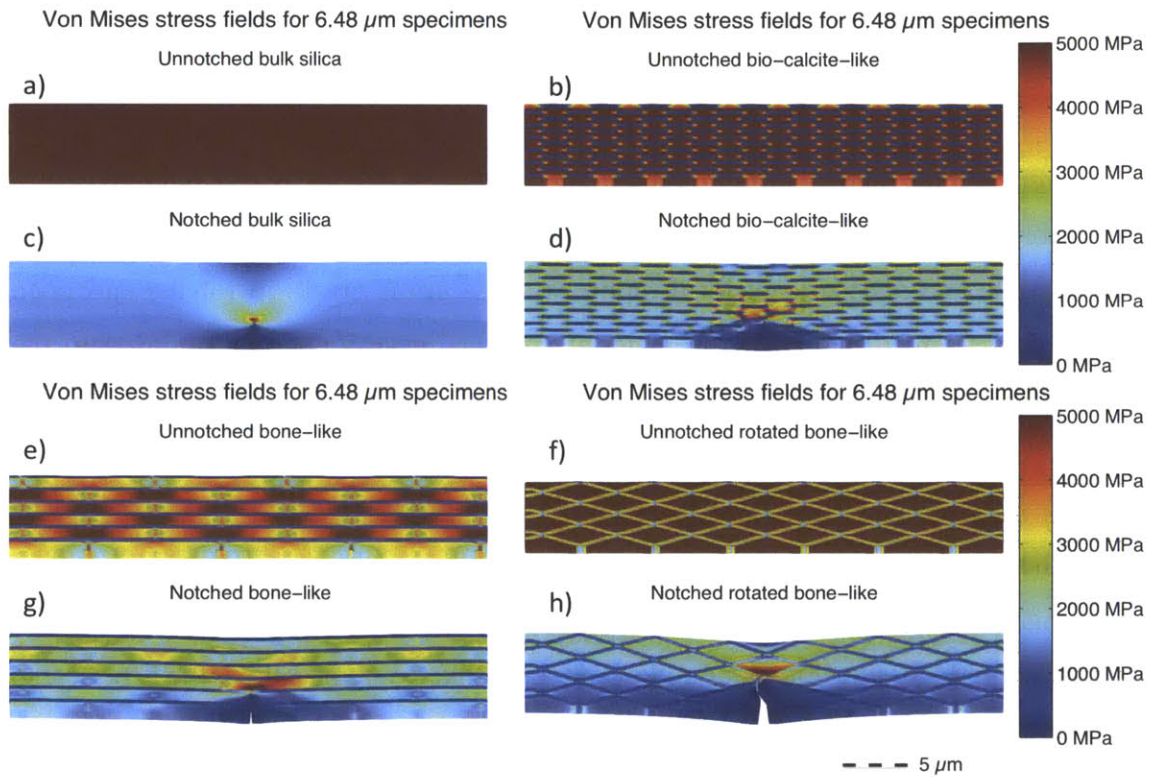
#### **4.4.1 Ordered arrangement of nanoporous silica – Decreasing sensitivity to cracks**

Figure 15 shows the Von Mises stress fields immediately prior to failure for the unnotched and notched specimens of the all 6.48  $\mu\text{m}$  systems, this corresponds to the points indicated by the circular markers in Figure 13. The panels clearly illustrate the reduced crack sensitivity exhibited by the hierarchical bio-calcite-like and bone-like geometry.

The reference, bulk silica system, Figure 15a, behaves just as one would expect a perfectly brittle system to behave. It displays a perfectly uniform stress distribution in the unflawed state and a significant localization of stress at the crack tip for the specimen with the flaw. Here the bulk of the material is virtually unstressed as opposed to the unnotched case and the stress field has completely changed as a result of the introduction of the crack.

On the other hand, the observed stress distributions in the composite systems indicate that toughening mechanisms are occurring. The specific geometrical arrangements of the deformable phase in the bio-calcite-like and bone-like systems allow the stresses to distribute throughout the entire specimens despite the flaws. These observations support the data presented in Figure 14 exhibiting the increased flaw tolerant behavior of the bio-calcite-like and bone-like system. In particular the bone-like geometry exhibits quite impressive behavior. Naturally, the stress level drops by introduction of the notch, however inspection and comparison of Figure 15e and g shows that the overall method of stress transfer is the same. The stress distribution is far less affected by the crack than any of the other geometries and the stress concentration at the crack tip is significantly less prevalent. The soft matrix arranged in the perpendicular grid with components perpendicular and parallel with the loading renders a far less sensitive response to the notch for the overall structure and a more efficient material usage, the bar plot depicted in Figure 16b underlines this point.

Figure 16 illustrates, for all notched geometries tested of 6.48  $\mu\text{m}$  size, the efficiency of material usage in an intelligible manner. It depicts the distribution of stress levels felt by the stiffer particles. Interpreting the mean of these stress levels as a measure of efficiency of material usage it is seen that both the bio-calcite-like and bone-like geometry far outperform the bulk silica specimen in this sense.



**Figure 15** Von Mises stress fields for 6.48  $\mu\text{m}$  (a) unnotched bulk silica, (b) unnotched bio-calcite-like, (c) notched bulk silica, (d) notched bio-calcite-like, (e) unnotched bone-like, (f) unnotched rotated bone-like, (g) notched bone-like and (h) unnotched rotated bone-like specimens at the instant immediately prior to failure. The unnotched bulk silica specimen shows the expected even distribution of stress throughout the sample while the notched specimen exhibits the strong characteristic stress concentration at the crack tip. The specific topologies have a visible effect on the stress distribution in the composites and the bio-calcite-like and bone-like specimen both exhibit significant delocalization of stresses in their flawed state. Specifically in the bone-like system the load path in both specimens, notched and unnotched, is seen to be very similar. This specific hierarchical geometry alleviates the stress tip concentration and maintains the same mechanism of load transfer despite the presence of the crack, thus reducing the specimen's sensitivity to the notch.

The configuration of the rotated bone-like geometry differs from the bone-like geometry only by the orientation and spacing of the grid, yet the analysis already unveils that the mechanics of the two systems are significantly different. Referring to Figure 14 the 6.48  $\mu\text{m}$  notched sample of the bone-like geometry is seen to reach almost 60 % that of its

theoretical strength, the strength of its unnotched counterpart, quite impressive as opposed to the notched bulk silica sample, which endures less than 20 % of its theoretical strength.

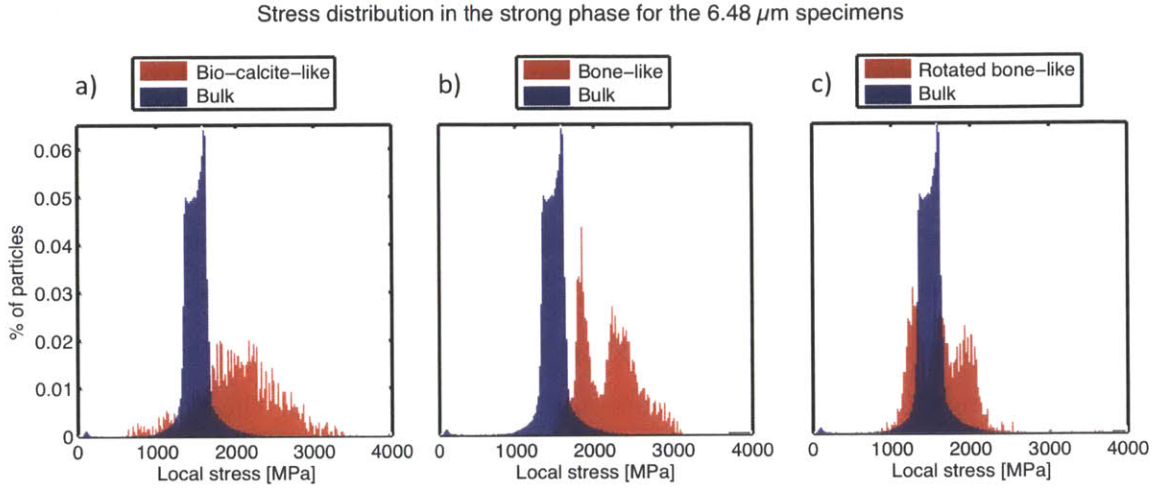


**Figure 16** Plots comparing the stress distribution in the notched bulk geometry with the stress distribution within the strong particles of the (a) notched bio-calcite-like geometry, (b) the notched bone-like geometry and (c) the notched rotated bone-like geometry for the 6.48  $\mu\text{m}$  specimens. The plot clearly shows how the strong particles in the bio-calcite-like geometry and the bone-like geometry are significantly higher stressed than their counterparts in the bulk-silica specimen, thereby supporting the claim that the stronger phase in these structures is more efficiently utilized after the introduction of the notch than in their bulk silica counterpart.

In this context it is noted that the vertical parts of the soft continuous phase in the bone-like geometry actually carry a significant stress, despite their compliance and weakness. Compare the stresses in this phase with the corresponding stresses in the deformable phase for the bio-calcite-like geometry and rotated bone-like geometry in Figure 15, the corresponding stresses in the bio-calcite-like geometry and the rotated bone-like geometry are far lower than for the bone-like geometry. This feature is again a direct effect of the specific architectural composition of the bone-like geometry. Significant longitudinal stresses will necessarily flow through the stiff platelets thus requiring a corresponding participation of the vertical soft phase in the stress transfer. This likely has an effect on the crack sensitivity of the geometry, i.e. the flaw tolerant size of the system.

As the term is used here, a structure with a large flaw tolerant size is less sensitive to cracks at larger length scales than a structure with a very small flaw tolerant size.

Specifically, the flaw tolerant size refers to the size dimension at which the geometry reaches its theoretical strength despite the presence of a flaw [26]. Regarding the tested specimens in this study as single edged notched tensile specimens, conventional linear elastic fracture mechanics predicts the flaw tolerant size to scale with the inverse square root of the strength of the material [113]. The specific geometrical configuration of the composite in the bone-like geometry thus increases the flaw tolerant size of the material for this loading condition by transferring significant stresses through the weak phase.

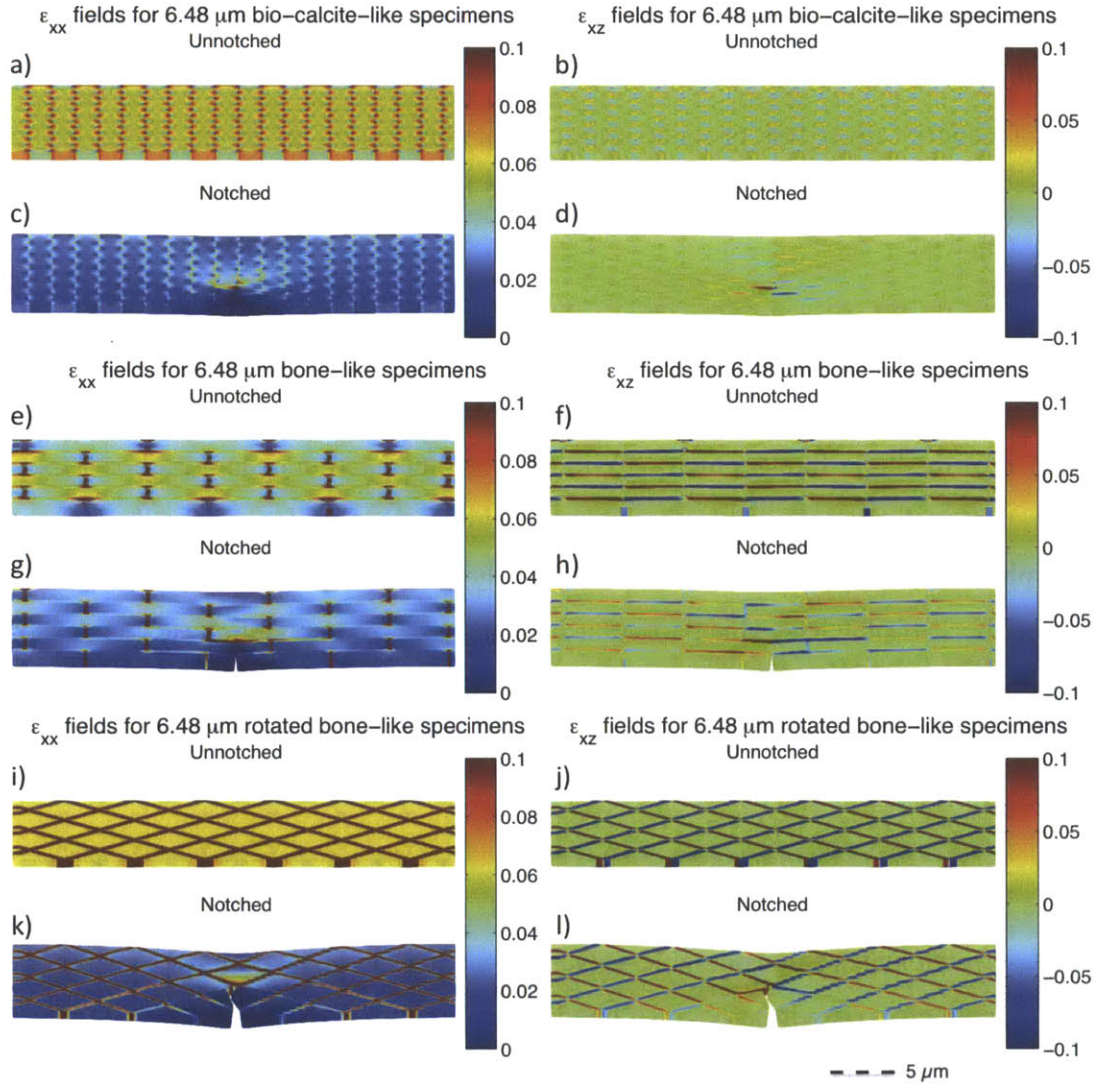
The compliance of the soft phase makes it well suited for absorbing deformation and studying longitudinal and shear strain fields of the respective geometries can identify further mechanisms induced by the various topologies. Figure 17 presents strain fields for unnotched and notched 6.48  $\mu\text{m}$  specimens of all composites studied. The strain fields for the bulk silica specimens are easily inferred from the stress fields and thus not presented here.

Figure 17a-l clearly indicate mechanisms explaining the results presented in Figure 14 and Figure 16. For the bio-calcite-like and bone-like systems the ordering of the deformable phase allows strains to spread more evenly through the structures despite the presence of the notch and thus forcing stresses to delocalize. Higher stress levels can be attained at regions further from the tip of the crack and a more efficient material usage is obtained. This behavior is directly linked to the compliance of the deformable phase.

Strain will naturally tend to concentrate in regions of least resistance. In very strong and rigid structures such regions are commonly represented by cracks where localizations of strains and stresses lead to sudden catastrophic failures, as exemplified by the notched bulk silica. Introducing a compliant weaker phase provides alternate regions for the strain to concentrate in and around. When appropriately arranged the softer phase is here shown to be able to make the effect of the crack less critical. It does this through employing its compliant nature to absorb significant strains away from the crack tip thereby more evenly distributing stresses throughout the sample and thus minimizing the effect of the notch. The specimen to some extent ‘forgets’ that it has a crack and strains and stresses



flow in similar ways as in the unnotched case. The geometrical configuration of the soft matrix decreases the sensitivity to the crack by means of its compliance and architecture. Thereby it is also clear that the specific architecture will determine the efficacy of the deformable phase. In light of this a more detailed discussion of the strain transfers in these two material systems is now given.



**Figure 17** (a) Longitudinal and (b) shear strain fields for unnotched bio-calcite-like geometry at the instant immediately prior to failure. (c) Longitudinal and (d) shear strain fields for notched bio-calcite-like geometry at the instant immediately prior to failure. (e) Longitudinal and (f) shear strain fields for unnotched bone-like geometry at the instant immediately prior to failure. (g) Longitudinal and (h) shear strain fields for notched bone-like geometry at the instant immediately prior to failure. (i) Longitudinal and (j) shear strain fields for unnotched rotated bone-like geometry at the instant immediately prior to failure. (k) Longitudinal and (l) shear strain fields for notched rotated bone-like geometry at the instant immediately prior to failure.

Considering the strain field plots for the bio-calcite-like geometry one can clearly observe that both the longitudinal and shear strain distribution is markedly different between the unnotched and notched case. At regions further from the crack tip longitudinal strain transfer, in both phases, only persists around the corners of the soft platelets. Furthermore it is observed that the shear strain transfer is in fact restricted to these areas also prior to introduction of the crack. Even though the dispersed deformable platelets clearly improve the mechanical behavior of the material over that of the benchmark system it is apparent that the stiff matrix does not provide optimal communication of strain through the system. Strain is not easily transferred between the compliant platelets due to the stiff nature of the matrix.

In contrast to this stands the method of strain transfer in the bone-like geometry. The mechanisms of strain transfer are essentially identical for the unnotched and notched 6.48  $\mu\text{m}$  specimen of the bone-like geometry. With the combined action of longitudinal strain transfer in the vertical compliant phase and shear strain transfer in the horizontal compliant phase strains (and stresses) are effectively communicated through the matrix and between the stiff platelets. This particular ordering of the compliant phase enables an attractive combination of the respective properties of the composite constituents even after the introduction of the notch, activating both the strength of the stiff phase and the deformability of the compliant phase.

Finally, the rotated bone-like geometry also exhibits a characteristic behavior. Whereas the stiff phase participates a considerable amount in the longitudinal strain transfer for the unnotched specimen it is virtually unstrained away from the crack tip in the flawed specimen. As also highlighted in Figure 14 the 6.48  $\mu\text{m}$  specimen of the rotated bone-like geometry actually experiences a larger sensitivity to the presence of the flaw than the benchmark bulk-silica system. The inclination of the deformable matrix allows longitudinal strains to flow continuously through this phase throughout the specimen. After introducing the crack, the geometrical configuration of the soft phase therefore does not induce significant strain transfer in the stiffer phase and this flawed composite cannot sustain as large forces as its flawed bio-calcite-like and bone-like counterparts.

#### 4.4.2 Introduction of weak links – stabilizing fracture

Failure and fracture of brittle materials such as silica and also silicon is well studied [114, 115]. Upon loading such materials build up large stress concentrations around flaws and crack tips. When these stress concentrations reach some critical value the cracks propagate catastrophically at very large speeds leading to complete failure of the materials. Such catastrophic fracture commonly occurs without warning and thus these types of failure are undesirable.

Figure 18 through Figure 20 illustrate the propagation of fracture through the tested samples with size parameter of  $23.78\ \mu\text{m}$ . The cracks propagate rapidly without large increments in strain for both the bio-calcite-like geometry in Figure 18 as well as for the bone-like geometry in Figure 19. The potential for sustaining loading also drops quickly as fracture progresses in these geometries. For the bone-like geometry in Figure 19 the stress level endured by the sample as a whole has dropped to half its maximum level in Figure 19c and the specimen has essentially failed. The rotated bone-like specimen on the other hand, presented in Figure 20 exhibits contrasting and quite attractive fracture characteristics and the following discussion will highlight the mechanisms behind this and connect them to the topology of the system.

The visualizations of the fracture propagation provided in Figure 20a-d show desirable stable crack propagation through the  $23.78\ \mu\text{m}$  rotated bone-like specimen. The titles of the individual panels indicate the strain state at which the snapshots are taken: 4.79%, 5.17%, 5.40%, and 5.54%, respectively. The strain increment at each step of the simulation for this particular geometry is 0.047%. Fracture occurs gradually and stably, significant increasing deformations can be sustained and the specimen endures a high level of stress despite the propagating crack. Inspect these panels in connection with Figure 13b; the fracture propagation corresponds to the yielding plateau of the stress strain response. The key here is the inclination of the soft phase. The inclination allows the longitudinal strains to flow continuously throughout the specimens, as opposed to the other inspected geometries, see Figure 21, thus enabling the crack to be entrapped in the soft phase. Consequently, the crack tip is blunted and as stress concentrations scale with

the inverse square root of the crack tip radius the severity of the crack lessens and a stable propagation of fracture is achieved. The ordered geometry of the nanoporous silica phase introduces significant toughening mechanisms in a composite with silica as its building block, a material commonly known as very brittle.

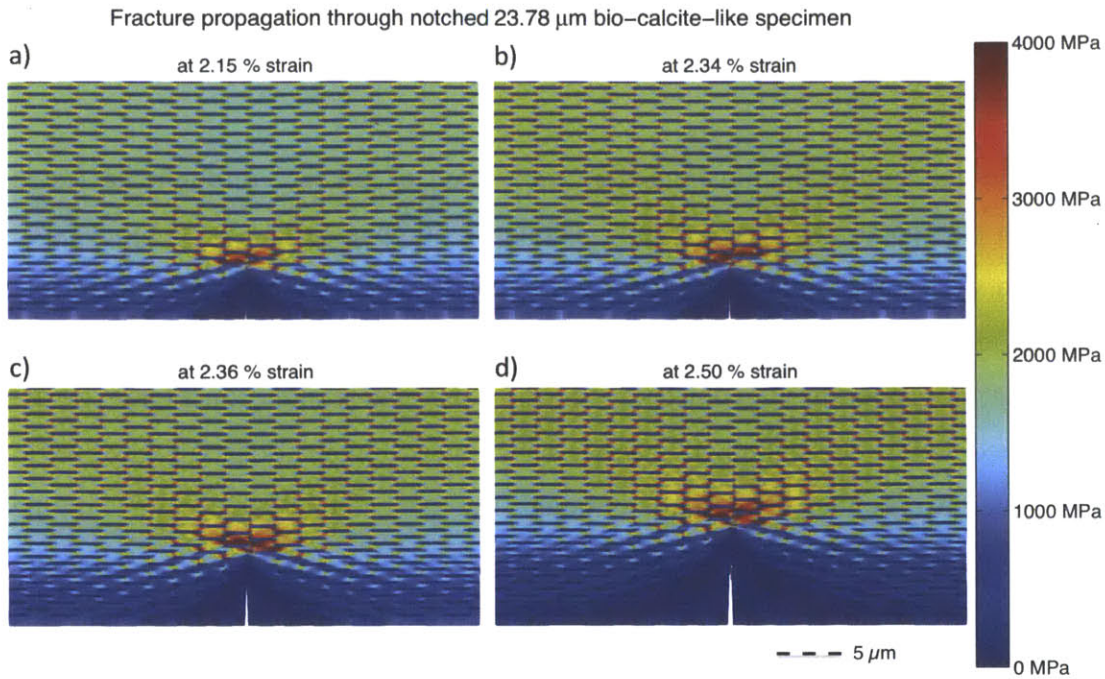


**Figure 18** Crack propagation through the 23.78  $\mu\text{m}$  bio-calcite-like specimen. Snapshots are taken at (a) 2.15% strain, (b) 2.34% strain and maximum loading, (c) 2.36% strain and (d) 2.50% strain and immediately prior to complete failure of the specimen. Strain increments are 0.017%. To visualize details in the distribution of stresses the maximum limit of the color bar was lowered to 4000 MPa.



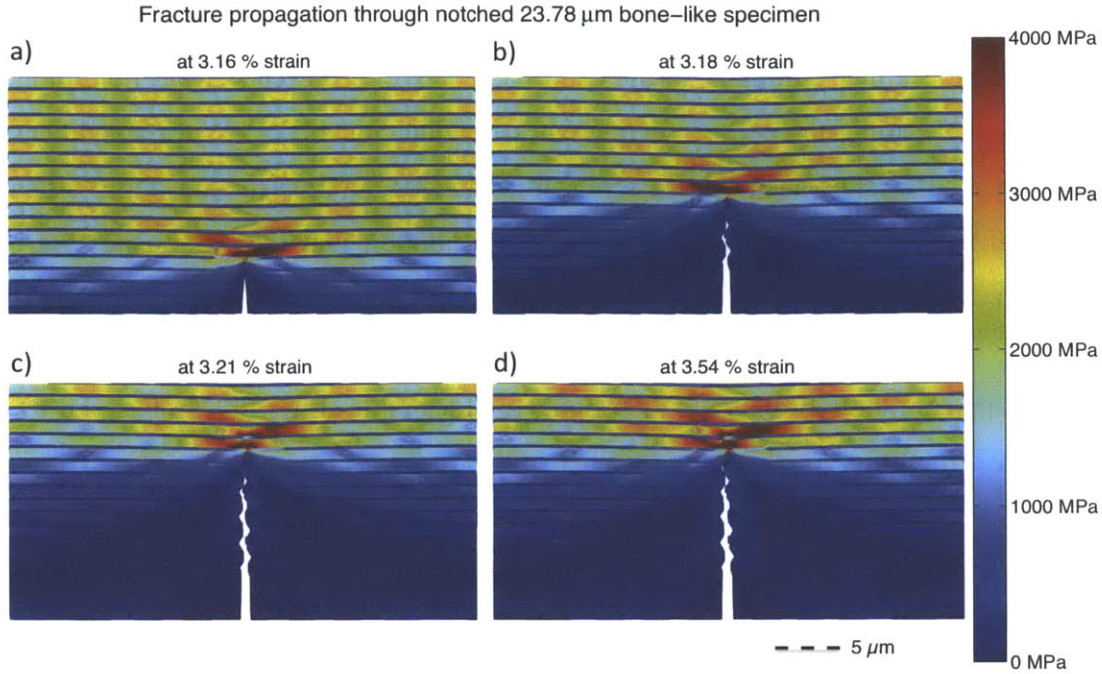


**Figure 19** Crack propagation through the 23.78  $\mu\text{m}$  bone-like specimen. Snapshots are taken at (a) 3.16% strain and maximum loading, (b) 3.18% strain, (c) 3.21% strain and (d) 3.54% strain and immediately prior to complete failure of the specimen. Strain increments are 0.019%. To visualize details in the distribution of stresses the maximum limit of the color bar was lowered to 4000 MPa.

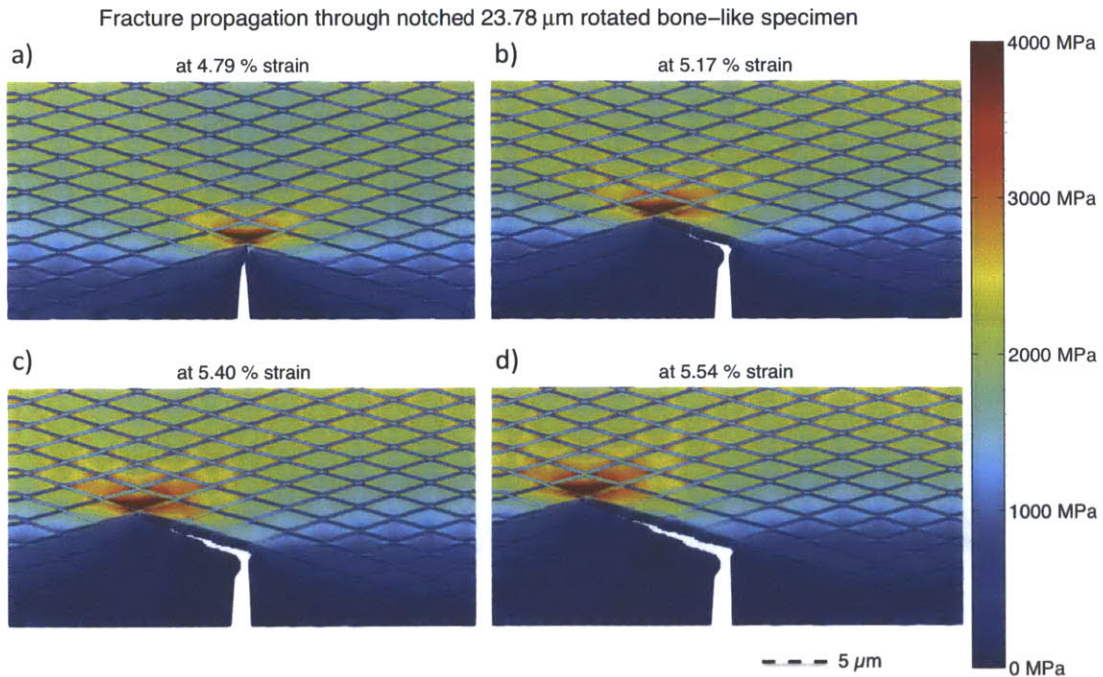


**Figure 20** Snapshots showing stable crack propagation through the 23.78  $\mu\text{m}$  rotated bone-like specimen. Snapshots are taken at (a) 4.79% strain, (b) 5.17% strain, (c) 5.40% strain and (d) 5.54% strain and immediately prior to unstable crack propagation. Strain increments are 0.047%. To visualize details in the distribution of stresses the maximum limit of the color bar was lowered to 4000 MPa.

#### 4.4.2.1 Comparing strain transfer in 23.78 $\mu\text{m}$ specimens – summarizing findings

Figure 21 serves as a nice summary of the discussion above. It presents strain field plots at the instant the geometries endure their greatest loading for all 23.78  $\mu\text{m}$  specimens studied. Figure 21a shows the large concentrations of strains in the bulk silica configuration, the unfavorable benchmark strain distribution that the composites were meant to outperform.

Figure 21b-d present the more evenly distributed and desirable strain fields observed for the composite structures. As also stated earlier, the soft phases present new areas where strains tend to develop, thus forcing strains to distribute in accordance with its arrangement and delocalizing loading from the crack. Significant strains are observed throughout the structures and all of the flawed 23.78  $\mu\text{m}$  composite samples attain a considerably larger fraction of their theoretical strength than the bulk silica specimen, see Figure 14.

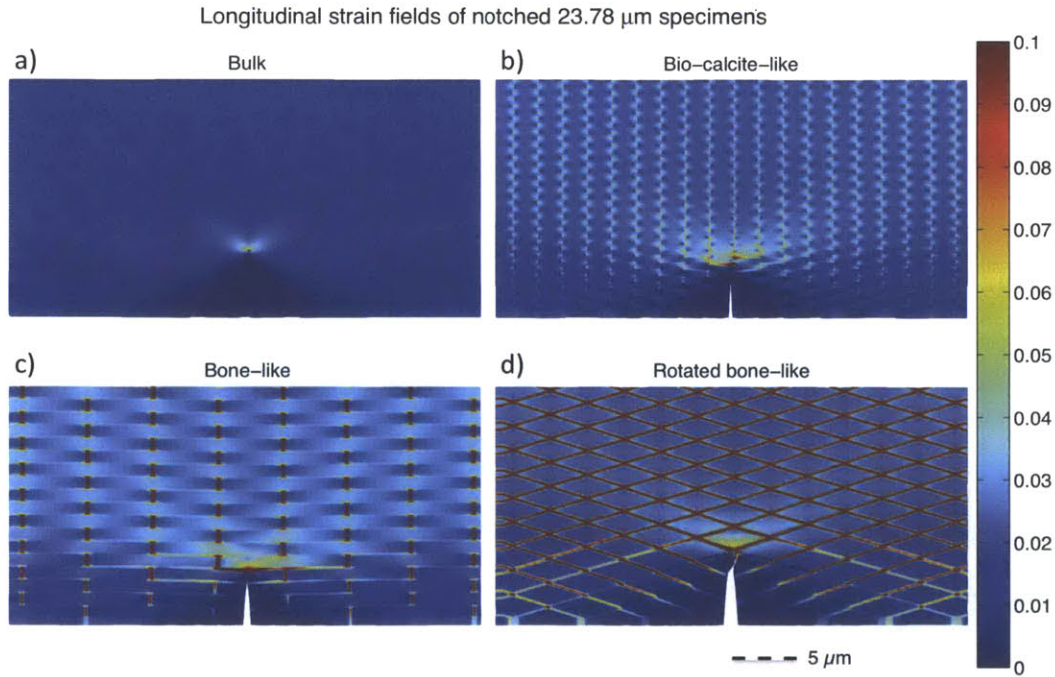


**Figure 21** Longitudinal strain fields for 23.78  $\mu\text{m}$  (a) bulk-silica, (b) bio-calcite-like, (c) bone-like and (d) rotated bone-like notched specimens at the instant where each of the specimens reach their maximum loading. The plots illustrate how the distribution of the soft phases controls the pattern of the strain transfer, and thereby enable a distinct mechanism of deformation and failure.

Comparing the behaviors in Figure 21b-d the large influence of the specific geometries is apparent. It is readily observed that the strain transfer in the bio-calcite like geometry in

Figure 21b is obstructed by poor communication of strain through the stiff matrix. On the other hand, the geometries with a continuous soft phase in Figure 21c, d show a superior strain distribution and higher strain levels despite constituting of the same building blocks. Further, the large longitudinal strain achieved in the vertical compliant phase of the bone-like geometry actively employs the stiff platelets in the transfer of strain thereby giving the structure a robust response independently of the presence of the flaw. Finally, the inclined nature of the deformable phase in the rotated bone-like geometry allows the longitudinal strain to flow continuously throughout the specimen. Flaws thereby become trapped within this phase, preventing catastrophic failure and stabilizing fracture.

#### **4.5 Scalability of results**

Much effort has been devoted to creating artificial mimics of mineralized structures with geometries similar to the composites discussed in this study [39, 116, 117]. One of the biggest challenges is the dominance of nanosized structural features characteristic of these materials. Despite many advances, a large-scale cost-effective production method of such synthetic structures is still out of reach. An upswing of focus on self assembly techniques as highlighted in [116] provides exciting outlooks. Despite the clear advantage of nanoscale structural features in terms of increased flaw tolerance one may argue that the results presented here could show that nature's design principles are applicable and useful at a range of length scales, length scales at which large-scale cost-effective production methods do exist. A spring bead model as the one utilized for this analysis is applicable at the nanoscale as well as the macroscale [95] with the appropriate adjustment of constitutive relations for the springs. Further the employed constitutive relations are quite generic and neither are they limited to certain length scales. Thus one may also expect the presented results are applicable at a range of length scales and valid for geometries with features at length scales beyond the nanoscale.

#### **4.6 Conclusions**

The study reported here has investigated the mechanics and deformation mechanisms of mesoscale structures composed of phases with contrasting constitutive behavior ordered in specific configurations. By conducting this study with a simple model in a systematic

manner, exploring the effect of different geometries and sizes and the effect of the presence of flaws, fundamental insight into intelligible principles employed by nature in its design of mineralized materials have been gained.

The mechanism by which a simple compliant phase can improve the mechanical behavior of a flawed structure at the mesoscale can desensitize a structure to a flaw simply by means of its soft nature. As opposed to a stiff and strong material where stresses concentrate around flaws like cracks or voids, the soft phase in the bio inspired composites presented here provides an alternate route for deformation and the methods of strain transfer and mechanisms of failure depend on its geometrical distribution. A brick and mortar like distribution of the stiff and soft phase was shown to give a far more efficient material usage in the presence of a crack, while an inclined continuous soft phase was shown to inhibit catastrophic propagation of fracture. Further, showing that such attractive characteristics can be reached without a vast energy dissipation mechanism such as protein unfolding and without the addition of additional hierarchies exemplifies the importance of a detailed study of the particular design principles observed in nature. Only through such a study can one attain fundamental insights into these principles and gain a complete understanding of their potential.

## **5 Designing tougher composites by elucidating simple interactions between composite constituents**

The previous chapter served to highlight the important contribution of topologies in controlling the fracture mechanical response of composites. Indeed, composites exhibiting a wide range of mechanical behaviors were assembled using the same building blocks, bulk and nanoporous silica, in the same number of hierarchical arrangements. As discussed in the introductory chapters toughness and strength are two widely desired material properties that material scientists strive to combine in synthesized materials. In Chapter 4 the bone-like topology was shown to exhibit an exceptional combination of these two properties, with toughness highlighted by the large length scale of flaw-tolerance and the significant stress delocalization. In the context of the bone-like topological arrangement a new fundamental question is raised; how do the specific constitutive behaviors of the composite constituents control the fracture mechanical response of the composite?

Furthermore, this chapter aims to highlight whether purely elastic effects can induce large-scale toughening and if a range of composites can be obtained by simply tuning the constitutive relations of the constituents. To investigate this issue a simple molecular mechanics model, similar to that previously employed is applied. The model is not intended to describe the full complexity of natural composites, but rather, it is meant to examine purely elastic effects on large-scale toughening, as outlined above.

It is further hypothesized stiff composite can be assembled with superior toughness at ‘minimal cost’ by combining two building blocks, whose fully elastic constitutive laws are intimately correlated, exhibiting the identical inferior toughness. Previous



computational and theoretical studies have shown that small stiffness ratios can lead to crack tip shielding [29] and indeed for vanishing stiffness-ratios, crack tip driving forces have been shown to disappear completely in stratified structures [32, 33]. However, at a disappearing stiffness-ratio, and a finite extensible compliant phase, the failure mechanism transitions to failure by delamination, and other mechanisms are necessary to ensure structural reliable materials. Here, by adapting another bio-inspired topology the aim is to combine the concept of vanishing stress concentrations at low stiffness ratios with structural reliability and propose novel design mechanisms for superior tough composites.

## 5.1 Materials and Methods

For the purpose of investigating the interactions between composite constituents that control the fracture mechanical behavior of the composite structural system, model materials are designed. These model materials are intended to model general material and composite systems, rather than a specific natural or synthetic system. Again, a triangular lattice spring-bead model is employed and the interactions between beads are governed by springs following a linear Hookean force extension law derived from a harmonic potential (Figure 22a). Here the springs, the bonds between the beads, respond in a linear Hookean manner up to a critical extension  $r_c$ , upon which they break and a crack either nucleates or grows. The bone-like topology along with the experimental setup is illustrated in Figure 22b.

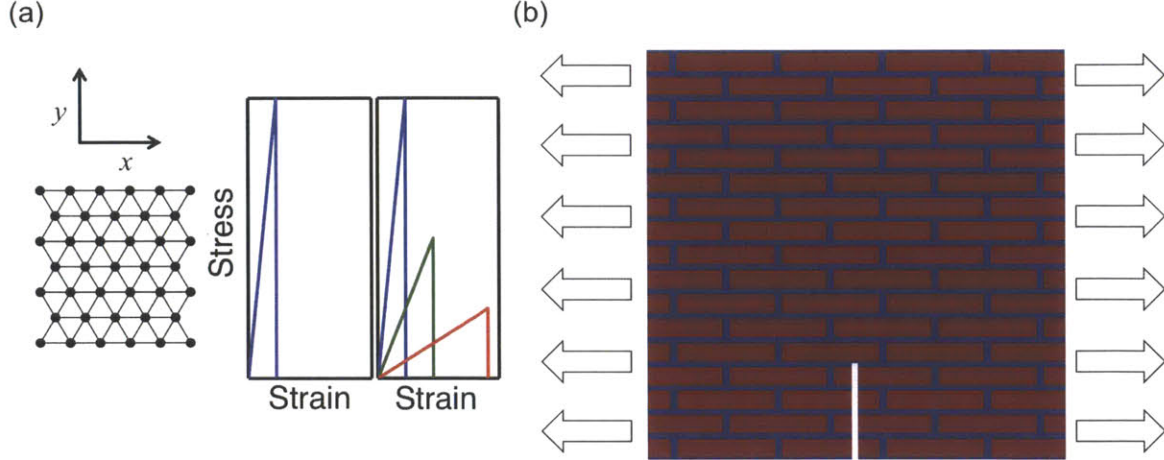


**Figure 22** (a) Triangular lattice spring-bead material representation to describe a coarse-grained model of the material. All lines are of identical length. The constitutive relations for stiff phase are presented along with three example constitutive relations for the soft phase, representing the first three combinations of elastic properties listed in Table 1. The area under all four curves drawn is identical. (b) Brick and mortar composite topology considered here. Platelets are drawn in red while matrix phase is represented with blue. The notch and mode I loading condition used here is also represented.

**Table 2** Overview of variables, dimensions and their definitions. Dimensions are given in terms of the base dimensions  $M$ ,  $L$  and  $T$ .

Variable	$k$	$r_c$	$E$	$\epsilon_c$	$\rho$	$D$
Dimension	$\frac{M}{T^2}$	$L$	$\frac{M}{L \cdot T^2}$	$\frac{L}{L}$	—	$\frac{M}{L \cdot T^2} \cdot \frac{L^2}{L^2}$
Definition	Spring stiffness.	Critical spring extension.	Young's modulus.	Critical/failure strain.	Stiffness ratio.	Toughness modulus.

The constitutive relation of the platelets, the phase colored in red in Figure 22b, is kept constant throughout the study, and this phase will henceforth often be referred to as the stiff phase. The matrix phase, colored in blue in Figure 22b, will be referred to as the softer phase.

The fundamental aim here, is to show that purely elastic materials with appropriate elastic constants can be combined in a generic composite topology, such as the brick and mortar geometry, to create tough composites. Although an energy dissipating matrix phase is indeed suited for the assembly of tough composites, the hypothesis that this is not

necessary is pursued here. In concert with this hypothesis, constitutive relations of the stiff and soft phase are designed to have identical toughness modulus. The force extension law of the springs is parameterized with a spring constant  $k$  and a critical extension  $r_c$ . By use of the Cauchy-Born rule and geometrical considerations the spring stiffness and critical spring extension are readily translated to an equivalent Young's modulus,  $E$ , and failure strain,  $\epsilon_c$  [98]. It is easily validated that

$$\frac{r_{c,\text{soft}}}{r_{c,\text{stiff}}} = \quad \text{and} \quad \frac{k_{\text{soft}}}{k_{\text{stiff}}} = \frac{E_{\text{soft}}}{E_{\text{stiff}}}. \quad (19)$$

Introducing the parameter  $\rho$  to represent the stiffness ratio,

$$\rho = \frac{k_{\text{soft}}}{k_{\text{stiff}}} = \frac{E_{\text{soft}}}{E_{\text{stiff}}}. \quad (20)$$

Furthermore, enforcing the constraint that any two phases have the same toughness modulus leads to a scaling law relating the stiffness ratio and failure strains:

$$r_{c,\text{soft}} = r_{c,\text{stiff}} \sqrt{\frac{1}{\rho}}, \quad \epsilon_{c,\text{soft}} = \epsilon_{c,\text{stiff}} \sqrt{\frac{1}{\rho}}. \quad (21)$$

The two equalities in **Equation (3)** are identical.

Figure 22a shows the constitutive relation of the stiffer phase as well as three examples of employed constitutive relations of the softer phase. Table 2 presents an overview of all variables listed with their respective definitions, and Table 3 summarizes the ensemble of constitutive laws used in this study. It is highlighted that the study presented here makes no attempt to model specific natural systems or any particular material. It is thus convenient to express the parameters and results in non-dimensional units.



**Table 3** Elastic constants for the stiff (platelets) and soft phase (matrix) of the composite. Constants are expressed in normalized units,  $E \cdot \epsilon_c^2 = \text{const.}$

Stiff Phase		Soft Phase	
$E_{stiff}$	$\epsilon_{c,stiff}$	$E_{soft}$	$\epsilon_{c,soft}$
1	1	1	1
1	1	0.7901	1.125
1	1	0.6400	1.25
1	1	0.5289	1.375
1	1	0.4444	1.5
1	1	0.2500	2
1	1	0.1111	3
1	1	0.0625	4
1	1	0.0400	5
1	1	0.0204	7

As indicated in Figure 22b the samples can be regarded as single edged notched tensile specimens. The crack extends to a tenth of the specimens length in the  $y$ -direction and maintains the same length for all tested samples. Periodic boundary conditions in the  $x$ -direction are implemented to prevent boundary effects at the location of load application. Each system is tested four times, each time with different displacement increments, to ensure that the energy minimization works properly, does not cause the system to diverge from a global minimum, for a given displacement increment. The four strain increments used are 0.42, 0.84, 1.69 and  $3.38 \cdot 10^{-5}$ .

The softer phase comprises approximately 20% of the entire volume of the structure. This volume fraction is chosen, as it enables the modeling of a minimal volume fraction of the matrix phase at a low computational cost. Experimentations with composite modeling using spring bead triangular lattices indicated that a certain minimal number of adjacent beads are required in each phase for the system to be well behaved. Restricting the volume fraction of the more compliant phase is critical as a basic goal of this study is to create a composite combining appreciable stiffness with toughness.

## 5.2 Results

The range of composite behaviors achieved by tuning the interactions between the two phases with perturbations of the constitutive law of the matrix phase is visualized in Figure 23. Stress versus strain responses of four representative samples are presented; the stiff bulk system, included as a baseline, and three composite structures with stiffness ratios,  $\rho = 0.64, 0.44$ , and  $0.02$ . The bulk baseline system, with the same constitutive relation for both phases, behaves perfectly linear elastic and exhibits brittle failure, as expected. The three composite systems exhibit three fundamentally different behaviors.

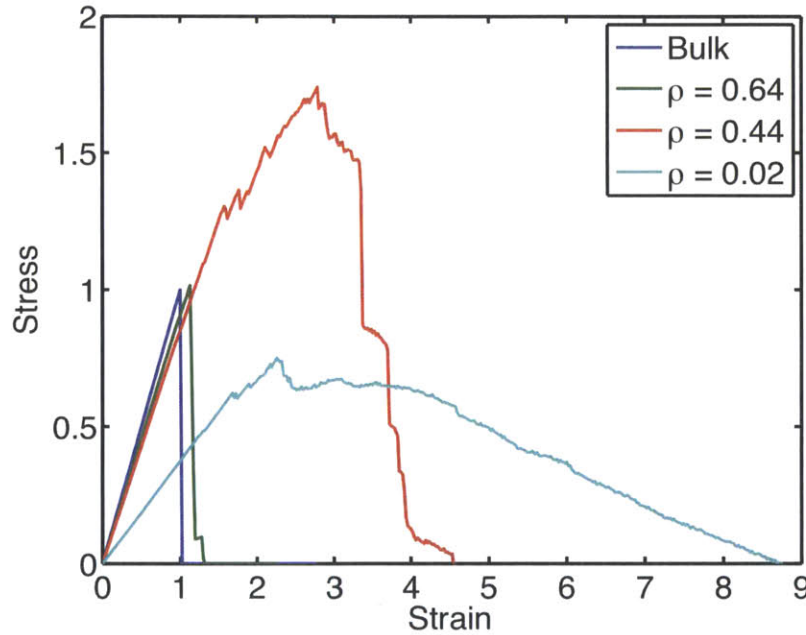


**Figure 23** Stress-strain responses for the bulk system and three composite structures,  $\rho = 0.64, 0.44$  and  $0.02$  (recall that  $\rho = E_{\text{soft}}/E_{\text{stiff}}$ ). The strain and the stress are normalized by the maximum strain and stress of the brittle bulk system. Graphs indicate the rapid change in composite behavior as the stiffness ratio is varied.

The first thereof, indicated in green, is a system that behaves very similarly to the bulk system; a negligible increase in peak stress and a virtually unchanged Young's modulus are recorded. The second composite system whose response is indicated in red in Figure 23, reaches a peak stress almost twice as large as the baseline system while compromising only a fraction of the bulk stiffness. Finally, the third presented composite, indicated in cyan, is the most compliant of the three and exhibits a ductile response with a gradual stable failure.

The simple tuning of the constitutive law of the matrix phase, constituting only 20% of the sample volume, has had a large influence on the composite structural response and has given rise to three fundamentally different composite behaviors. Furthermore, it is seen that, in addition to post-peak mechanisms, the two latter composites attain larger macroscopic strain levels by prolonging their pre-peak elastic response. These observations give strong indications that the composites exhibit reduced stress concentrations while retaining structural reliability with very simple building blocks, akin to mineralized bio-composites. In an effort to gain a more fundamental understanding of the mechanical principles governing these composite responses, stress and strain fields of the samples are now analyzed.

Figure 24 shows strain and stress field plots, drawn at the instant the structures endure their peak loading, for the three composite systems as well as the stiff bulk system. Figure 24b, f clearly illustrates that the  $\rho = 0.64$  system behaves very similarly to the perfectly brittle bulk system shown in Figure 24a, e. This stiffness ratio proves insufficient to significantly redistribute strain and stress from the crack-tip and the large localization of stress and strain at the tip of the flaw is maintained. However, once the stiffness ratio drops below 0.5 to  $\rho = 0.44$  (Figure 24c and g) a fundamental change in deformation mechanisms occurs. For the current geometrical configuration, the mismatch in stiffness is sufficient to accommodate a delocalization of strains from the ‘critical’ flaw to the softer matrix. Thereby, strains are spread throughout the system and the entire composite is incorporated in the strain and stress transfer, leading to a more beneficial structural response. Taking the stiffness mismatch one step further, the responses shown in Figure 24d and h are obtained and a new shift in the composite deformation mechanism is observed. Now the compliance of the matrix phase is so large that the matrix phase adsorbs a large share of the deformation of the entire structure and the stress level in the stiffer platelets is significantly reduced. The overall structural response is thus significantly more compliant and the system can also reach larger levels of strain.

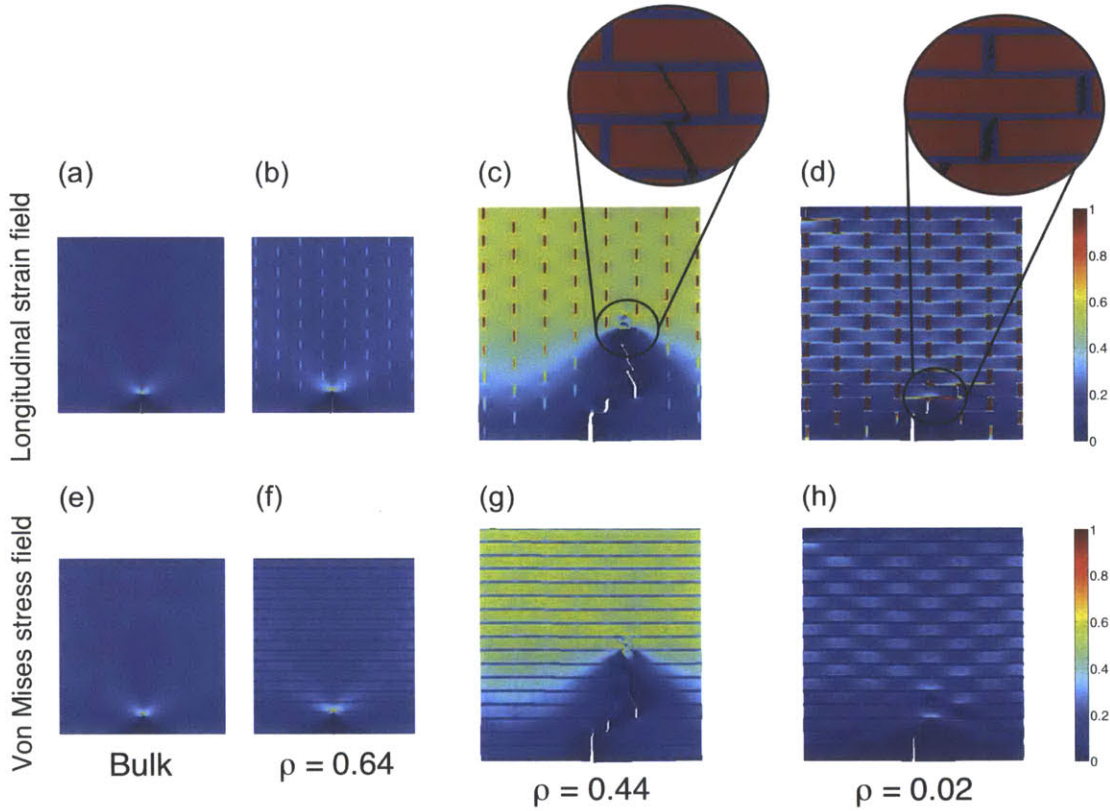


**Figure 24** Longitudinal strain fields and Von Mises stress fields for the bulk system, (a) and (e); the composite structures with stiffness ratios  $\rho = 0.64$ , (b) and (f);  $\rho = 0.44$ , (c) and (g); and  $\rho = 0.02$ , (d) and (h). The longitudinal strain field plots clearly show the softer phase taking an increasing portion of the strain as the stiffness-ratio decreases accompanied by a delocalization of stress and strain from the crack tip and increased stress and strain in regions far from the crack tip. Panels (c) and (g) clearly exhibit the superior performance of the  $\rho = 0.44$  composite structures. Insets for panels (c) and (d) indicate a transition in fracture mechanism.

Moreover, the insets in Figure 24 show that the fracture mechanism also changes as the stiffness ratio decreases from  $\rho = 0.44$  to  $\rho = 0.02$ . Whereas the fracture propagates through both the platelet and matrix phase for the composite with  $\rho = 0.44$ , it has become energetically more favorable for the fracture to move solely through the matrix phase in the softer system with  $\rho = 0.02$ . The fracture mechanism has transitioned to a platelet pullout mechanism akin to biological brick and mortar systems [68]. In a true biological system such as nacre, with a stiffness ratio similar to this composite system, platelet pullout is a favorable failure mechanism as it activates additional toughening mechanisms such as frictional dissipation from interfacial sliding, breaking of nanoasperite bridges, and protein unfolding in the organic matrix. These findings indicate that nature designs the stiffness ratio between the mineral and organic phase in bio-

mineralized composites such as to accommodate platelet pullout. Furthermore, it is noted that in the modeled composite system the softer phase does not just act as an isolator shielding the platelets from load concentrations; on the contrary, it serves to transmit significant stresses and strains. This is a key factor contributing to the reliability of this structural system; even regions below the crack tip still have significant contributions to the overall mechanical response (Figure 24).

To compare the fracture properties of the composites their toughness modulus is compared. The toughness modulus is defined as the area under a stress-strain curve, the strain energy density required to fracture a specimen. The toughness modulus is a typical metric of fracture resistance in biological materials as they do not obey conventional linear elastic fracture mechanics (LEFM) [9] (in which case the J-integral would be a natural method for characterizing fracture toughness [118]).

In Figure 25 the normalized toughness modulus  $T/T_{\text{stiff}}$  is plotted versus stiffness ratio  $\rho$  for all four tensile tests of the nine different composite systems. The toughness moduli are normalized by the toughness of the flawed bulk system whose response is indicated with a black data point in the figure. The legend identifies points on the graph with the different displacement increments that are utilized in the respective simulations, one through four representing  $0.42$  through  $3.38 \cdot 10^{-5}$ . No consistent trend associated with the decrease in displacement increment is observed and thus the results are deemed to reliably represent the behavior of the model system subjected to quasi-static displacement induced loading.

Figure 25 nicely represents the consequences of the deformation mechanisms observed in Figure 24. The first few composite systems with  $\rho > 0.6$  notice barely any change in toughness modulus with varying stiffness ratio, whilst for  $0.4 < \rho < 0.6$  a rapid, almost eight-fold increase of the toughness modulus is observed. This large sudden transition supports the view of a fundamental change in the deformation mechanism of the composite, as was suggested above. The interesting point here, worth underlining, is that this first shift in mechanical behavior, from traditional brittle bulk behavior to strong and



tough composite behavior, occurs with such a small perturbation in the constitutive law of the matrix phase. The dramatic shift is made possible with a 30% decrease in stiffness accompanied by a 20% increase in failure strain. Figure 25 illustrates that further decreases in  $\rho$ , accompanied by increases in  $\varepsilon_c$ , do not have as large an influence on the toughness modulus. The key inter-constituent interaction that facilitates increases in toughness modulus of the flawed composite is the cooperative deformation that alleviates the stress localization at the crack tip (Figure 24).

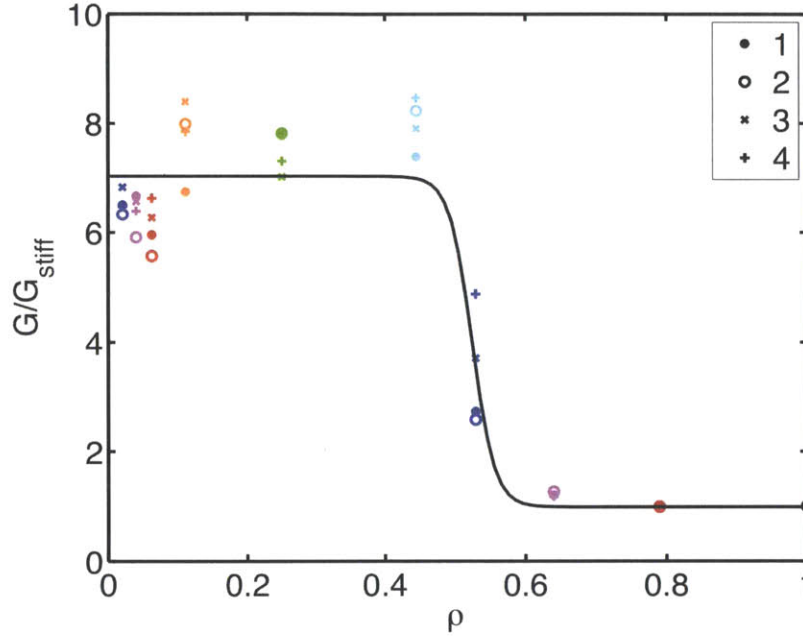


**Figure 25** Normalized toughness modulus  $G_{norm}$  plotted versus stiffness-ratio  $\rho$  for all four tests on the ten specimens. The legend identifies the markers indicating the results for the simulations with the various displacement increments, 1 through 4 indicating displacement increments of  $0.42$  through  $3.38 \cdot 10^{-5}$ . The fitted curve is a sigmoid function described by  $f(\rho) = 1 + 6 \exp(-63\rho + 33) / (1 + \exp(-63\rho + 33))$ . The parameters for this fit were found by method of penalized least squared errors.

Figure 25 displays a sigmoidal function fit to the toughness data. Analyzing the limiting cases of the system motivates this functional form for the toughness evolution. In the limit as the stiffness ratio approaches the maximum value,  $\rho \rightarrow 1$ , the composite behaves entirely as a brittle bulk material and the system achieves its minimum toughness modulus, the toughness is bounded from below. On the other hand, considering systems with very compliant matrix phases in the context of stress delocalization, and recalling that the constituents have constant fracture energy the toughness modulus of the composite system has an upper bound as  $\rho \rightarrow 0$ .

For composites with a laminated geometry at the crack tip the stress concentration at the tip of the crack is predicted to vanish as the stiffness ratio between the compliant and stiff phase decreases [32, 33]. In [32] the critical stiffness ratio is given as a function of the volume ratio of the softer phase, for a volume fraction of 20% the critical stiffness ratio is  $\sim 0.25$ . In the system studied here, the brick and mortar structure will serve to alleviate the stress concentration at a higher stiffness ratio as the strain is given a continuous path through the matrix phase (Chapter 4.4.2.1), thus motivating that the transition occurs at a larger stiffness ratio,  $\rho \sim 0.5$  (Figure 25).

The limiting cases are revisited to produce an estimate of the maximum attainable toughness in the studied system. As the stress concentration decreases, the deformation delocalizes completely and strain distributes throughout the entire structure. As the stiffness ratio decreases further, strain concentrates in the matrix phase and at the asymptotic limit of a vanishing stiffness ratio it is postulated that the deformation of the entire structure will be completely absorbed by the softer phase. The energy required to fracture the softer matrix phase will thus account for the entire toughness modulus of the system. By design, all constituents have the same toughness modulus and the energy required to fracture the compliant matrix as  $\rho \rightarrow 0$ , can be evaluated by investigating the theoretical limit of the toughness modulus for the homogeneous system. This theoretical limit is readily evaluated by analyzing the behavior of a perfectly homogeneous defect free system. Again the fact that all phases require the same energy to fracture is utilized.

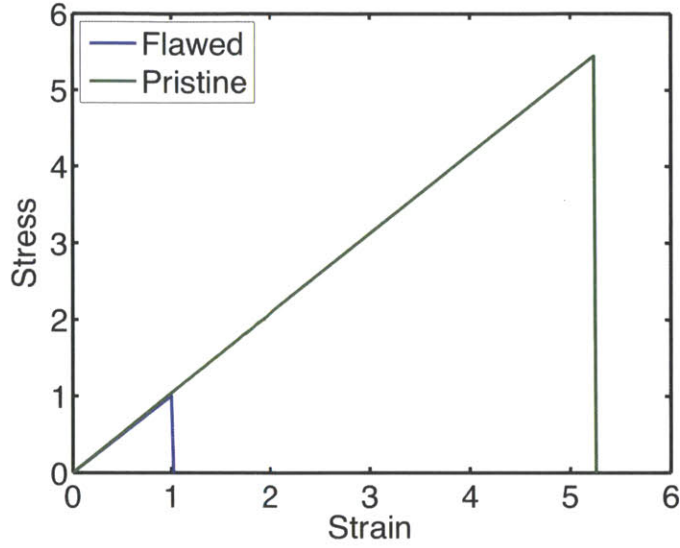


**Figure 26** Stress versus strain response of pristine and flawed system. Again, both stresses and strains are normalized by the maximum values of the flawed bulk sample. The pristine sample is seen to fail at a stress  $\sim 5.5$  times larger than the flawed bulk sample.

As shown in green in Figure 26, this defect-free homogeneous system fails at a stress approximately five and a half times larger than the flawed bulk system whose response is indicated in blue; the stiffness of the pristine system is marginally larger than that of the notched system. It follows that

$$D_{th} = \frac{1}{2} \frac{\sigma_{th}^2}{E} \approx \frac{1}{2} \frac{(5.5\sigma_{br})^2}{E} \approx 30D_{br}, \quad (22)$$

where the subscripts “th” denotes theoretical, and “br” brittle, respectively. As the soft phase constitutes 20% of the volume and has the same fracture energy as the stiff phase by construction, the toughness in the limiting case  $\rho \rightarrow 0$ , can be estimated as as,

$$D_{lim} \approx 0.2D_{th} = 6D_{br}. \quad (23)$$

In the intermediate case the load and deformation will be shared by the stiff and compliant phase and thus the gain in toughness is expected to exceed this limiting value  $D_{lim}$ . In agreement with the prediction by this model the composite systems with smaller stiffness ratio  $\rho$  exhibit approximately a seven-fold increase in toughness modulus over the brittle system.

This study was motivated by the question of whether it is possible to create a composite with simple interactions that combines the properties of superior stiffness and toughness. In Figure 27 an Ashby plot of normalized Young’s modulus and normalized toughness



modulus of the composites studied is shown, red data points correspond to constituents and blue data points represent composite systems. Furthermore, blue circular markers indicate composites systems with  $\rho > 0.5$ , while the blue star markers denote composite systems with  $\rho < 0.5$ . The figure clearly displays that all composite systems studied here outperform their constituent materials in terms of toughness modulus. Furthermore, a class of the composites reaches superior toughness at significant stiffness, with the toughest system retaining over 80% of the stiffness of its stiffest constituent.

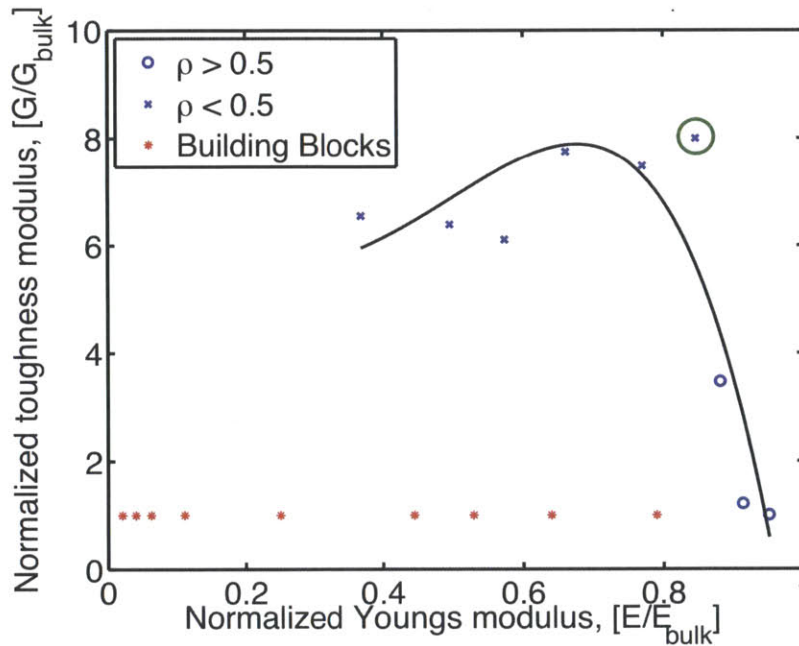


**Figure 27** Ashby plot of normalized toughness modulus versus normalized Young's modulus plotted together with corresponding representative Ashby plots of synthetic and biological materials. Stiffness' are normalized versus the stiffness of the bulk system and toughness' are normalized versus the toughness of the bulk system. Markers for composite systems with stiffness ratios  $\rho > 0.5$  are drawn with blue circles while those for systems with  $\rho < 0.5$  are drawn with blue crosses. The modulus-toughness combinations of the building blocks are indicated with red stars (same for all cases, by design). The superior toughness of the composite systems with respect to the individual blocks is clearly exhibited. The impressive performance of the stiffest  $\rho < 0.5$  system is clearly seen, circled in green, with an eightfold increase in toughness accompanied with a stiffness of over 80 % of the stiff bulk system. The fitted curve is a fifth-degree polynomial fitted by minimizing residual squared error, again with a non-zero regularization term. The curve clearly indicates that the composite structures span the Ashby area in a similar fashion as biological composites [119]. **Figure 24** exhibits the deformation mechanisms underlying the various mechanical performances indicated here.

Finally, it can be seen that the way in which the interactions between the two composite phases are tuned produces a set of composites that span the Ashby area in a similar way to biological composites, as both sets of these data points are best summarized by a

concave trend line [119]. This may indicate that the fundamental interactions in biological composites that control their superior mechanical properties are in fact governed by the stiffness ratio between the two phases as was hypothesized here.

It was previously established that stiffness ratios could be tuned to make stress concentrations vanish [32, 33]. Here it has been shown that by tuning constitutive laws one can further make structurally reliable systems with superior toughness. In systems where a softer matrix phase is included to alleviate stress concentrations it is clear that this matrix phase must be able to store a certain level of deformation energy in order to effectively redistribute loading before failing. The results presented here demonstrated that a compliant matrix in a brick-and-mortar structure can induce a significant toughening effect in a composite even though its fracture energy is limited to that of the stiff and brittle platelet phase. In this light one can view the class of composite structures designed in this study as ‘minimal cost’ structures. In mineralized biological structures where there are many more toughening mechanisms, structures can clearly achieve yet greater toughness values.

**Table 4** Summary of key mechanisms induced by changes to the constitutive laws. Three regimes are identified;  $\rho > 0.6$ ,  $0.3 < \rho < 0.5$ , and  $\rho < 0.3$ . The regime  $0.5 < \rho < 0.6$  is as indicated in **Figure 25** a transition regime and is therefore not discussed here.

Regime	Deformation mechanism	Failure Mechanism
$\rho > 0.6$	The composite behaves largely as a bulk material, exhibiting a stiff response and a large stress concentration at the crack tip. Further, strains are approximately uniformly distributed in regions far from the flaw with minimal preferential localization in the matrix phase.	The systems fail in a brittle manner with cracks propagating instantly and catastrophically through the system. The composites exhibit no significant increase in toughness modulus w.r.t. the bulk system.
$0.3 < \rho < 0.5$	The compliance of the matrix phase is optimally tuned to maintain a stiff system response and delocalize deformations and loads from the crack tip spreading stresses and strains uniformly throughout the entire composite. The entire system participates equally in load transfer and the two constituent phases cooperate efficiently.	As there is practically no stress concentration the dominant crack propagates in a stable manner allowing the composite to sustain increased loads as the system is deformed. The crack path is markedly jagged and alternates between passing through the stiffer and softer phase. The composite exhibits ductile failure with a significant increase in toughness modulus.
$\rho < 0.3$	The matrix phase dominates the mechanics of the system leading to an overall compliant response. The soft nature of the matrix effectively delocalizes stresses and strains from the crack tip. However, deformations concentrate in the matrix phase and the stiffer platelets are not optimally utilized.	Again, stable crack propagation is induced by the absence of a stress concentration and the composite exhibits ductile failure with a significant increase in toughness modulus. However, now the crack propagates exclusively through the matrix phase leading to large crack deflection.

### **5.3 Discussion**

By using a simple mesoscale bead model implemented in a molecular mechanics framework the mechanics of bio-inspired composite materials with a brick and mortar topology have been investigated. The fundamental mechanical interactions between the composite constituents were studied by tuning the constitutive law of the matrix phase, with the aim of identifying structurally reliable composites materials with high toughness and stiffness. The studies showed that the specific elastic behavior of the matrix phase controls the response of the composite and with small perturbations in the elastic behavior of this phase dramatic shifts in deformation and fracture mechanisms can be obtained (Table 4). Furthermore, it was shown that by tuning these simple elastic interactions structures combining significant stiffness with superior toughness as well as composites reproducing fracture mechanisms observed in mineralized biological materials could be designed. Moreover, a range of composite behaviors was produced filling an Ashby area in a similar fashion as biological structures, leading to the conclusion that the elastic interactions elucidated here are indeed fundamental design mechanisms in nature.

## **6 From Computer Models to Synthesized Composites – Closing the Loop**

Computer modeling and computer simulation have offered significant insights to the mechanisms controlling fracture mechanical response in bio-inspired structures. Indeed, optimal topological arrangements of soft and stiff phases have been identified and the fundamental interactions between the composite constituents controlling structural reliability have been elucidated. One question naturally arises; can these composites be manufactured? Driven by this question, the method of 3D printing for creating functional composites is explored.

Three-dimensional (3D) printing has as of late been gaining much attention due to its many possible applications in a wide range of industries; indeed exploring the areas of applicability of the technique is still an active area of research [120-127]. With the latest 3D printers capable of printing materials with widely contrasting mechanical behavior simultaneously in complex geometries at micrometer resolutions, the potential of this technology is growing. Advanced printing technology now offers the possibility to create complex topologies with fine features composed of a multitude of materials with varying mechanical properties quickly, cheaply and at a large scale. The specific geometries printed are a bone-like geometry, bio-calcite-like geometry and a rotated bone-like geometry consisting of a stiff and a compliant phase with a ~20% volume fraction of the softer phase (Figure 28).

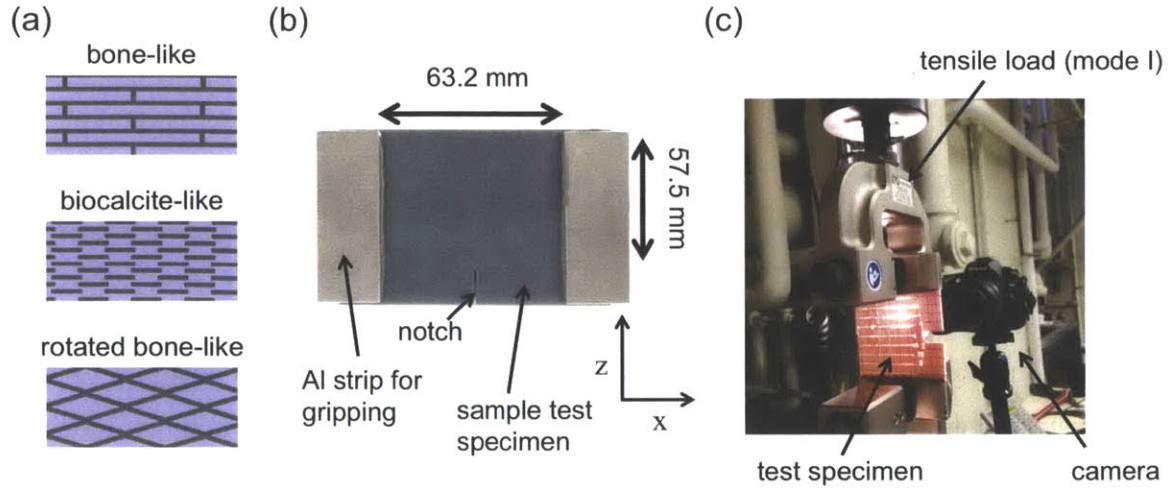


**Figure 28** Panel (a) shows schematics of the three investigated topologies. Panel (b) shows the setup of test specimens with relevant dimensions and coordinate system indicated. Panel (c) shows an image of the setup of the experiment. A specimen of the bone-like geometry is being tested in the picture, shown here as an example.

## 6.1 Materials and Methods

### 6.1.1 Experimental approach: Synthesis

All specimens used in the study are printed at Objet Inc., in Billerica, MA, USA using an Objet Connex500<sup>TM</sup> multi-material 3D printer. In a single print composites composed of two base materials, VeroWhitePlus and TangoBlackPlus, with strongly contrasting material properties are manufactured (Figure 29) [128]. Both VeroWhitePlus and TangoBlackPlus are photopolymers, based upon proprietary acrylic-based photopolymer resins, and will henceforth be referred to as material **A** and material **B**, respectively [129]. Consistently with the presentation in previous chapters, the lighter phase in Figure 28a represents the stiffer constituent and is printed with material **A**, and the darker phase represents the compliant constituent and is printed with material **B**. Figure 28 indicates the planar dimensions of the test specimen. The through thickness of all geometries is 3.125 mm.

The composites are printed with a dual material jetting technology allowing two distinct materials to be printed simultaneously. Each material, residing in cartridges, is funneled through a liquid system connected to the printing block consisting of eight printing heads. Two printing heads, each containing 96 nozzles with 50  $\mu\text{m}$  diameters, are reserved for

each of the two base materials, while the remaining four printing heads are used for printing a support material. The printing heads are followed by a UV light that immediately cures the printed material allowing new layers to be printed instantaneously [129]. Three specimens of each composite system detailed in Figure 28 are printed and one of each geometrical configuration is used as test specimens to arrive at a suitable experimental approach. The remaining six samples are used for mechanical testing and investigation of deformation and fracture mechanisms.

As the materials cure *in-situ* upon printing, they adhere to each other perfectly, *i.e.* the adhesion is as strong or stronger than the weakest phase. This is confirmed by the experimental observation that failure never initiates nor ever occurs at the interface of the base materials. The smallest feature size of the compliant phase in the prints is 250  $\mu\text{m}$  and is identical for all samples; the compliant phase is indicated in black in Figure 28a. The nozzle diameter controls the accessible length scale of the 3D printing. Since the specific topological arrangements of the base materials strongly influence the composites mechanical response, it is essential to ensure precise printing, thus justifying the feature size being a multiple of the nozzle diameter. This implies a larger length scale than that associated with the previous computational investigations, raising the issue of scalability of results. This was discussed in 4.5 and further comments are given below.

### **6.1.2 Experimental approach: Fracture testing**

To investigate the fracture mechanical response of the specimens, they are tested as single edged notched tensile specimens. The notches in the samples are cut so that all samples have an identical effective size in the dimension parallel to the crack direction, *i.e.* the uncracked length in the z-direction is the same for all samples (Figure 28). The notches are cut with a 1/32" thick carbide-slitting saw with a 60 degree included angle. When testing the sample specimens, initial crack propagation always occurs at the crack tip, thus indicating that the machined notches are sufficiently sharp.

For optimal gripping of the specimens in the testing apparatus, four aluminum strips are attached to each sample with Loctite E-90FL epoxy, two on either face of the planar specimen. The aluminum is roughed with sand paper to ensure optimal adhesion of the

Loctite epoxy and the epoxy is allowed to cure for 36 hours. The aluminum strips are positioned such that all samples have the same effective length, (Figure 28).

The 3D printed specimens are tested in an Instron 5582 Universal Testing machine with an Instron 100 kN, static load cell and displacement boundary conditions are applied. The boundary is loaded at a displacement rate of 3 mm/min. The compliant base material is very extensible and a much slower loading rate would require an exorbitant amount of time for testing. Typically, a high strain rate leads to brittle response of testing specimens; while the observation of stable crack propagation in the samples assures us that we still capture essential deformation and fracture mechanisms with the testing procedure.

The samples are clamped in place with serrated hardened steel grip faces attached to steel vice action grips. The load capacity of the grips is 100 kN and the spring stiffness of the entire testing device far exceeds the stiffness of the printed specimens. The specimens are attached firmly in the grips and the uncracked length of the geometries is centered with the force applied through the vice action grips to ensure pure tension in the specimens prior to initial crack propagation. However, it is clear that upon initial crack propagation, the specimen will no longer be subjected to pure tension. The force will be acting with an eccentricity on the remaining uncracked length of the test specimen. The moment induced by the eccentricity influences the near tip stress field of the geometries and thus leads to a different loading than a pure tension boundary condition would.

It is emphasized that the testing procedure adopted in this study is not meant to emulate a standard procedure as outlined in ASTM; rather an approach is designed that is both similar to the previous computational investigations and suited for investigating fracture and deformation mechanisms. The main focus here, is to keep the testing procedure consistent and similar to a setup that can be emulated with the presented computational model, as the main insights gained from this study derive from a comparative study of the deformation mechanisms of the manufactured specimens and simulated specimens.



### **6.1.3 Material properties of base materials**

Selections of bulk mechanical properties of the Objet printable materials have already been made available [128]. The referenced data indicates that of the materials available for printing, the two employed in this study represent the most contrasting mechanical behavior. Although this causes some difficulties for the computational modeling, material **A** and material **B** were still utilized as this made for a more straightforward printing. In future work it would be very interesting to explore more material combinations. No previous data exists on the stiffness of material **B** and thus mechanical tests are performed on both base materials in order to supply data to the computational model. A fundamental interest in this study is also the fracture response of the base materials and thus specimens of material **A** and **B** are prepared as fracture specimens as detailed above. Images of the samples pre- and post-testing along with their stress-strain responses are presented in Figure 29. The figure clearly shows the widely contrasting constitutive behavior of the two materials. Indeed, the modulus of the compliant material **B** is three orders of magnitude lower than the stiffer material **A**, by a factor of  $\sim 1,500$ . Furthermore, the more compliant base material fails at an order of magnitude higher strain than its less compliant counterpart, and both samples fail in a brittle manner immediately upon crack propagation.

### **6.1.4 Computational modeling**

In order to accommodate the new constitutive behavior of the 3D printed materials the constitutive relations in the computational model need to be re-parameterized. Independent studies have shown that spring-bead models are still sensible for the purpose of investigating fracture mechanics at the length scale of the composites printed here [91, 95]. In the following the material model utilized is presented along side with the rationale motivating it.

#### **6.1.4.1 Computational material model**

As the base materials cure during printing there is likely a certain amount of mixing present at the interface. With the small relative size of the compliant phase and the large difference in modulus of the two materials, the effective stiffness ratio is clearly far less than what is portrayed in Figure 29. In a simplified model the effective compliant phase

can be viewed as a layered composite of material **A** and material **B** and Voigt's rule of mixtures can be utilized to find the true stiffness. Assuming an approximate 3-4% mixing of the two base materials at the interface an effective stiffness ratio between 45 and 60 is estimated, as apposed to  $\sim 1500$ . A stiffness ratio of 50 is used for the computational model. The true stiffness of the compliant phase could be measured directly with the use of a micro- or nanoindenter. Using a test-apparatus with sufficient resolution would also give insight to the amount of interfacial mixing of the base materials. However, in an effort to keep the model simple it is found more appropriate to represent the system with the Voigt's rule derived effective stiffness ratio discussed above. In future work the model could be extended to account for the true stiffness distribution in the compliant phase as measured by indentation.

Independent mechanical tests report extensibilities of material **A** and material **B** ranging from 10-25% and 170-220% respectively [128]. From a purely geometrical perspective it is quite clear that the utilized triangular lattice becomes highly non-linear and unstable at such large deformations and it is advantageous to restrict the allowable deformation. That being said, it is also clear (and it has been discussed in detail above) that the deformability of the compliant phase is an essential feature of the composite and indeed plays an active role in the mechanics of natural mineralized materials. Experience with harmonic spring bead triangular lattice models indicates that 5% is a suitable minimal breaking strain. In order to maximize the extensibility of the compliant phase without compromising the stability of the model, this failure strain is thus adopted for the computational equivalent of material **A**. Furthermore the deformability of the compliant phase is chosen such that the toughness modulus of the composite constituents is identical, similarly as in Chapter 5. The resulting extensibility of the computational representation of material **B** is thus 35%, and the notched stress strain responses of the two model materials are given in Figure 29b.

The base materials used in this study are photopolymers, and although they behave linearly under the presence of a pre-crack (Figure 29b), their bulk constitutive relations are highly nonlinear. As this study represents a first effort to predict the behavior of the

3D printed system, the computational material model is restricted to linear elasticity (Figure 29b). A main focus in this study is to predict and understand trends in the deformation and fracture response of the printed composites and therefore it is sensible to start with such a simplified model. Although the specific nonlinearities of the photopolymers will clearly influence the particular crack propagation, it is argued that the dominating fracture and deformation mechanisms will mainly depend on the stiffness ratio and relative extensibilities of the composite constituents, thus validating the model selection. In future works the model can be extended to account for the nonlinearities of the printed materials and thus could be used for quantitative predictions of the printed systems response.

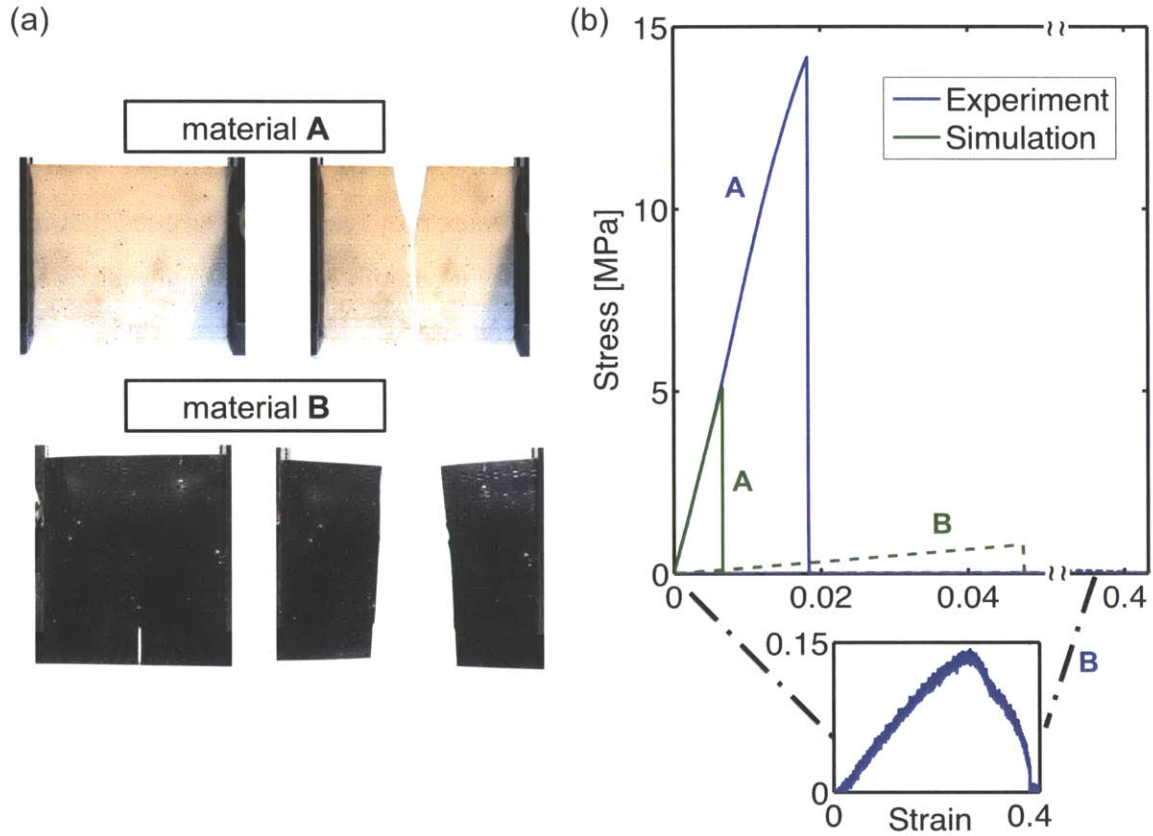


**Figure 29** Images of samples at the start of testing, the end of testing and graphs of stress-strain response for base materials, material A and material B, as well as their computational equivalents. **(a)** Images of test specimens of material A and material B before and after testing. Pictures indicate brittle catastrophic failure of the base materials. **(b)** Stress versus strain behavior of experimental and computational base materials drawn in blue and green respectively. The modulus of computational equivalent of material A is seen to match with its experimental counterpart. Further, the extreme compliance of material B makes it barely visible on the original plot and thus its notched stress strain response is included in an inset of the figure. The computational equivalents of material A and B are designed to fail at lower strains to avoid geometrical instabilities in the model. Further, the computational equivalent of material B is designed with a more humble compliance to avoid instabilities in the simulation, and to also more closely resemble the average mechanical properties of the printed compliant phase.

## 6.2 Results

In the following the mechanical response of the 3D printed specimens will first be compared with the computational predictions. Thereafter, the fracture mechanisms of the printed geometries will be analyzed independently of the simulations.

### 6.2.1 Comparison of Computational Predictions with Experiment

#### 6.2.1.1 Comparing mechanisms: the bone-like topology

Figure 30 presents a representative set of images comparing the deformation and fracture mechanisms of the 3D printed bone-like sample (Figure 30a) with the corresponding

mechanisms of the simulated specimen (Figure 30b). As predicted by the computational model this specific topological arrangement induces significant stress and strain delocalization, which is confirmed in the 3D printed system. The non-localized failure of the vertical compliant phase, exhibiting damage throughout the entire specimen, highlights this. The continuous compliant matrix phase distributes stress and strain effectively throughout the sample inducing a more robust mechanical response of the geometry. For the simulation results depicted in Figure 30b the delocalization is visualized in terms of snapshots of the longitudinal strain fields of the specimen. The vertical portion of the compliant phase adsorbs the bulk portion of longitudinal strain whilst the horizontal portion of the softer matrix binds the system together through shear strain action. This deformation mechanism exhibited by the computational and synthetic system is characteristic of mineralized natural materials such as bone and nacre [26].

In the inset of Figure 30a, a further remarkable trait of the 3D printed specimens is highlighted. As noted above, the interfacial adhesion of the constituent materials is so strong that the composites do *not* fail at the interfaces. This is compatible with the design of the computational model and underlines the significance of the topological arrangements for the mechanical behavior. Indeed, it is argued that the particular topological arrangements of the constituent materials are solely responsible for the impressive observed fracture mechanical characteristics.

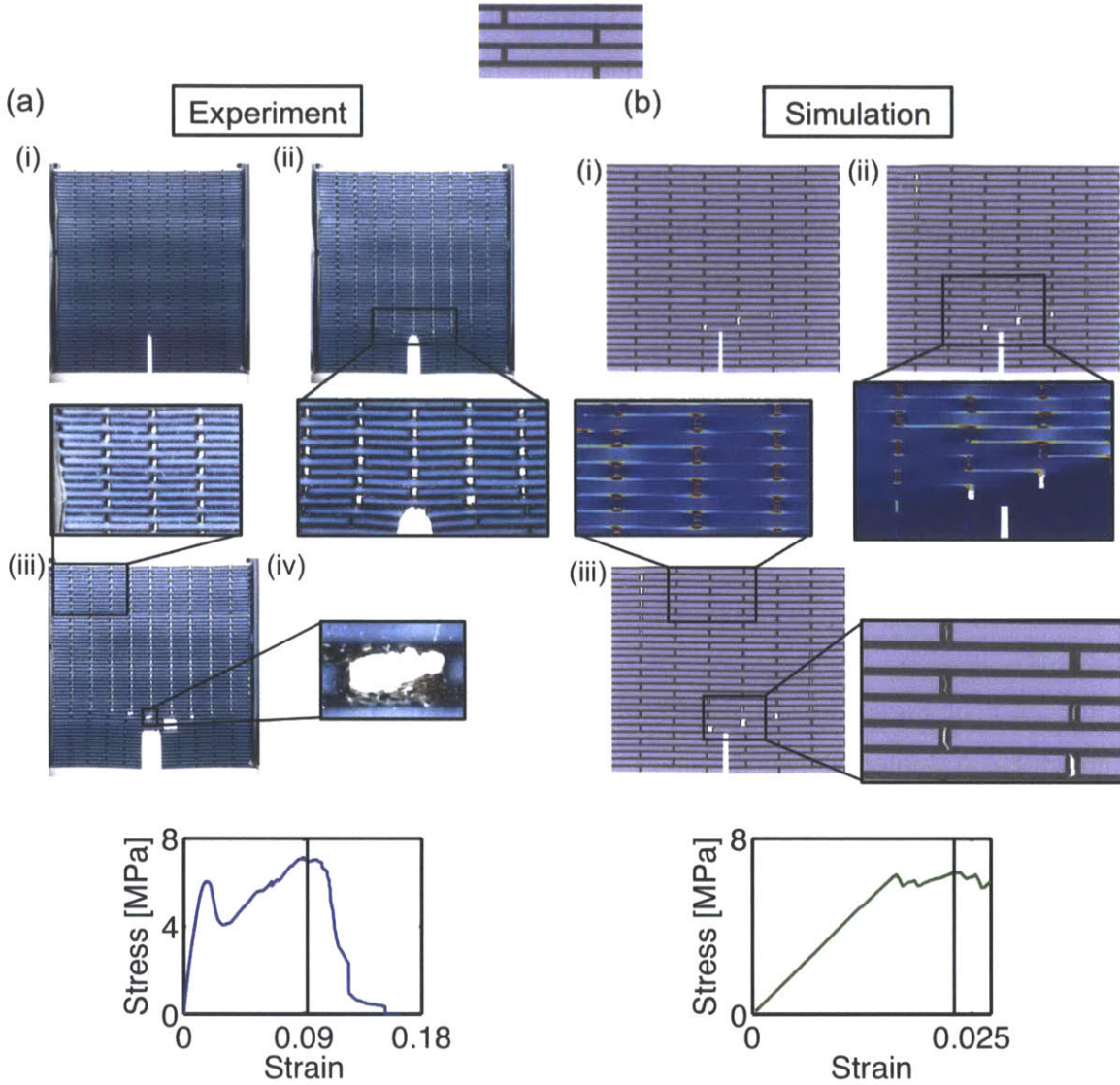


**Figure 30** Snapshots are presented displaying deformation and fracture mechanisms for (a) the 3D-printed and (b) simulated specimen of the bone-like topology, in direct comparison. The two samples exhibit very similar deformation and fracture mechanisms up to a certain point at which the change of boundary conditions in the experiment and the nonlinearities of the photopolymers start dominating. This instant is indicated with a vertical line in the stress versus strain plots. The figure shows that in both the synthetic and computational system the soft phase absorbs the bulk of the deformation and acts to delocalize the stress concentration around the notch. For the computational case shown in panel (b) the longitudinal strain fields are plotted in insets to make this clearer. Furthermore, the inset in panel (a) (iii) displays the strong interfacial adhesion of material A and material B with failure nucleating through the compliant material B instead of at the interface. This is consistent with the results of the computational model.

Upon further crack propagation the simulation predictions diverge from the experimentally observed behavior. As noted in Chapter 6.1.2, crack propagation induces eccentricity in the experimental loading conditions, whilst the computational boundary conditions remain constant throughout the simulation. The crack tip region in the

experimental setup is therefore subjected to a different stress field and thus producing an incompatible effect on crack propagation. Furthermore, as also discussed in Chapter 6.1.2, the specific constitutive relation of the experimental materials is highly nonlinear, as opposed to the fully linear constitutive laws of the model materials in the computational model. Once the crack propagates through the 3D printed phases the nonlinearities come in to play and are expected to have a significant effect on crack-propagation.

#### **6.2.1.2 Comparing mechanisms: the rotated bone-like and bio-calcite-like topology**

Next the agreement between simulation and experiment regarding the fracture and deformation mechanisms exhibited by the 3D printed bio-calcite-like and rotated bone-like topology samples is analyzed. Figure 31 compares the computationally predicted results with the experimentally obtained behavior for these two composite systems. First, analyzing the rotated bone-like system in Figure 31a, the images clearly portray that the 3D printed sample exhibits impressive mechanical characteristics in terms of stable fracture propagation. Again the longitudinal strain fields are plotted along with snapshots from the simulation to identify the underlying mechanical mechanisms controlling the failure of the specimen. The characteristic initial zigzag fracture path through the compliant phase exhibited by both the experimental and the computational system is seen to be explainable by the continuous transfer of longitudinal strain in the soft matrix. As it is energetically favorable for cracks to propagate through a more compliant material, and the stiffness mismatch is so significant, the fracture propagates solely through the matrix. Further, as the crack-tip is blunted in the low-stiffness region and the soft matrix delocalizes the loading, the crack propagates in a stable fashion through the system allowing the specimen to sustain increased deformation and significant loading throughout large portions of the fracture process.

Analyzing the further images of Figure 31a, it is noted that the second row of images from experiment and simulation indicate a diverging fracture path. The boundary condition that acts eccentrically upon initial crack propagation induces the inclined driving force on the crack and leads the fracture towards the boundary.



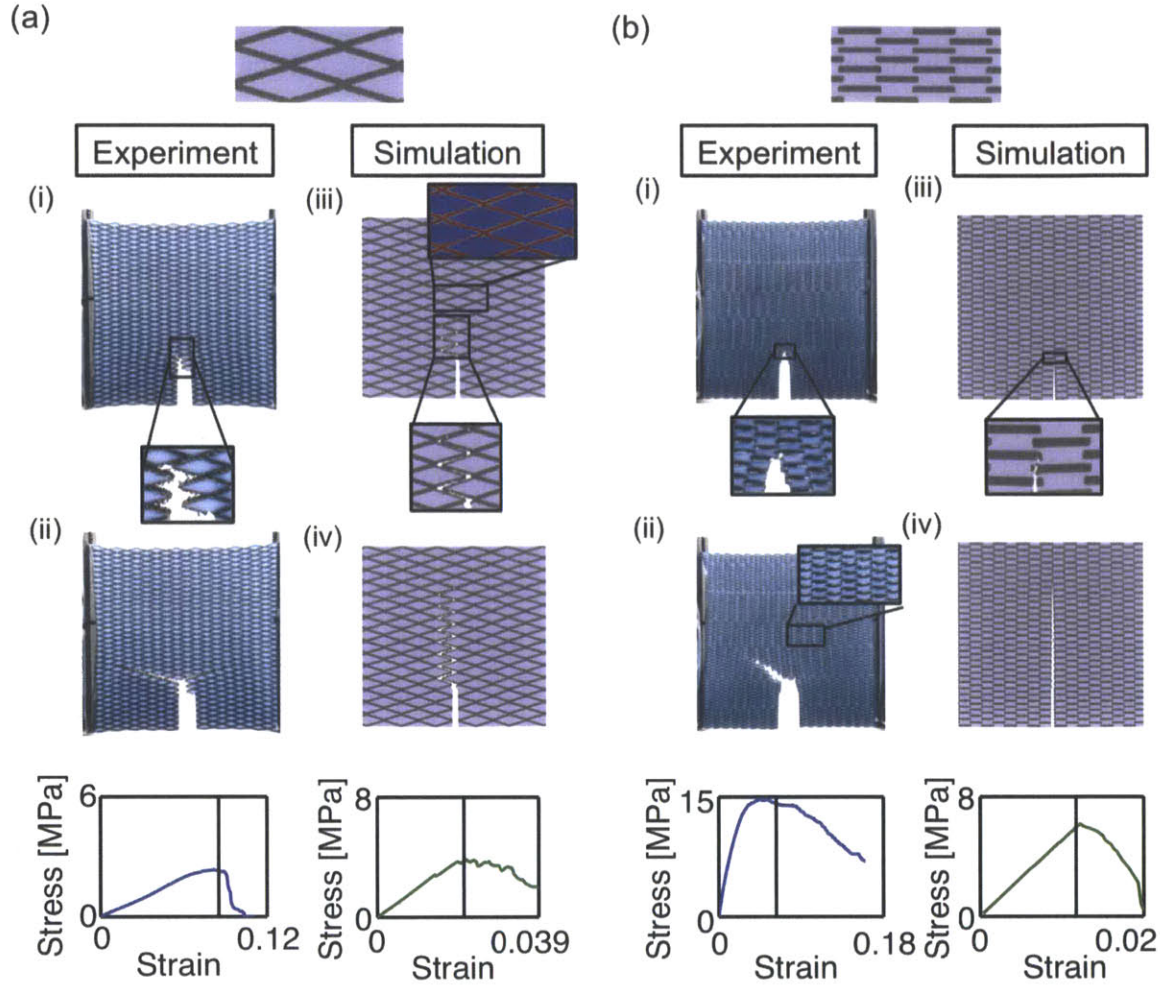


**Figure 31** Visualization of dominating deformation and fracture mechanisms in experiment and simulation for **(a)** the rotated bone-like geometry and **(b)** the bio-calcite-like geometry in addition to the respective stress-strain responses, again with blue and green indicating results from experiment and simulation respectively. Schematics of the topologies are included at the top. Panel **(a)** displays the characteristic zigzag fracture path observed both in the simulation and for the initial propagation in experiment. As the effective length of the sample decreases the eccentricity of the applied load increases, changing the boundary conditions and thus causing predictions from experiment and simulation to diverge. As is apparent from the displayed images, for both simulation and experiment, the compliant phase forces the crack to take a longer path thus inducing toughening in the rotated bone-like specimen. The stress strain responses also reveal that a very compliant behavior of this topology is correctly predicted. Panel **(b)** indicates that the simulation predictions and experimental observations for the bio-calcite-like topology do not overlap very well. The inset in panel **(b)** (ii) shows inaccuracies in the printing that are likely a contributing factor. Nonetheless, a similar toughening mechanism is observed in experiment and simulation in that both systems show an initial crack arrest and crack blunting in a soft inclusion; (i), (iii).

In Figure 31b simulation predictions and experimental observations for the response of the bio-calcite like topology are compared and contrasted. Although it is observed that the topology has not been replicated well by 3D printing (likely due to limitations with

respect to the resolution), the properties of the synthesized sample are still worth discussing. The images clearly portray that the 3D printed sample possesses fracture mechanical characteristics superior to its constituents exhibiting both stable crack propagation and significant crack tip blunting prior to main crack propagation. The latter toughening mechanism is highlighted in the inset of the figure showing that the initial fracture propagation leads the crack to a soft inclusion where the extreme compliance blunts the crack tip and delays further crack propagation. Once the crack does propagate, it is again observed to angle out to the boundary due to the resulting eccentricity of the applied load.

Due to the inaccuracies of printing for the bio-calcite-like topology, significant agreement between simulation and experiment for this case is not expected (Figure 32), although the snapshots from simulation do provide some overlapping mechanisms. In future work there are several ways to refine the approach outlined here to ensure a better agreement between topologies in experiment and simulation. The most apparent strategy is to increase the feature size at printing. Another, and possibly more appealing, solution is to print the samples vertically, with their thinnest dimension parallel with the ‘build tray’ as the machines perform with higher precision in this dimension [129].

Both the prediction of the computational model and the experimental result for the response of the bio-calcite-like system presented here differs from that presented in Chapter 4, where the composite system had a lower stiffness ratio and a brittle fracture of the system was predicted. This is consistent with the study outlined in Chapter 5 concluding that composites exhibit sudden transitions in deformation and fracture mechanisms as the constitutive relations of their constituents are tuned.

#### **6.2.1.3 Comparing trends in mechanical properties**

Figure 32 displays bar plots comparing select fracture mechanical characteristics of the various experimentally tested and simulated specimens respectively. The comparison is performed using data from experiment and simulation up to the point in which the two systems exhibit diverging mechanisms, *i.e.* the specimens reach even higher toughness modulus values and extensibilities than those indicated here. With exception of the bio-

calcite-like geometry (for reasons stated above), the trends of the mechanical properties have a very good agreement between experiment and simulation. The simulation prediction agrees with the experimental observation that the rotated bone-like topology is the most compliant and the most extensible. Furthermore, the predictions about the relative strength of the bone-like geometry and rotated bone-like geometry are also compatible with experiment. Finally, the computational model is able to correctly identify the toughest topological arrangement as the bone-like geometry, and the experiment shows that this system achieves a toughness modulus more than 20 times that of its constituents, a truly impressive result.

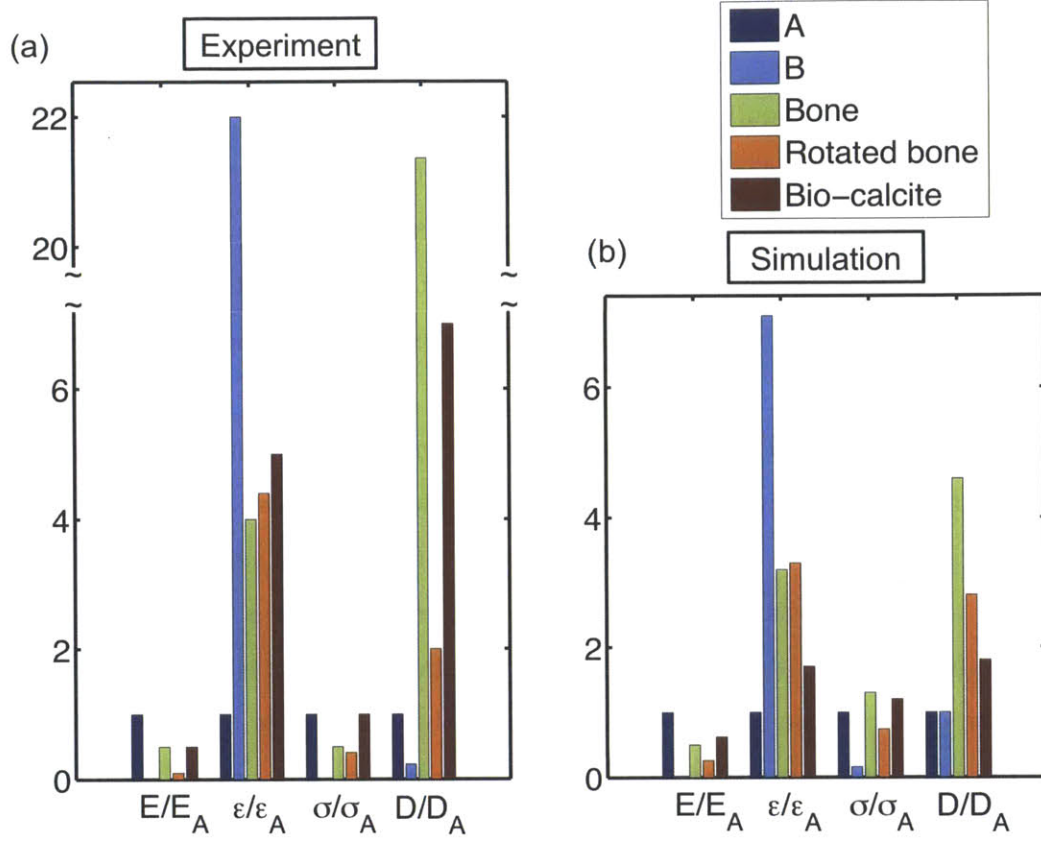


**Figure 32** Bar plot indicating trends of mechanical properties for the base materials and the various topologies studied in both (a) experiment and (b) simulation. A comparison is performed using data from experiment and simulation up to the point in which the two systems exhibit diverging mechanisms; these instants are displayed in Figure 4 and 5. For the simulation data, A and B refer to the computational equivalents of material A and material B as presented in Figure 3. The mechanical properties plotted are stiffness  $E$ , maximum strain  $\epsilon$ , maximum stress  $\sigma$ , and toughness modulus  $D$ . In panel (a) the data is, as indicated, normalized by the respective values for the base material A while in panel (b) the data is normalized by the respective values for the computational equivalent of the base material A. The figure portrays that, with the exception of the bio-calcite-like sample for reasons stated above, the mechanical properties of the simulated materials exhibit the same trends as those of the synthesized materials, *i.e.* the models predict the correct composite to be the most extensible, strongest and toughest. Furthermore, the largely impressive fracture toughness of the synthesized bone-like specimen is observed, exceeding that of its fundamental building blocks by a factor larger than 20.

## 6.2.2 Focus: experimentally observed fracture mechanisms

### 6.2.2.1 The bone-like topology

Snapshots of the entire fracture process of the bone-like specimen are presented in Figure 33. Figure 33c shows the crack propagating in a step pattern around the stiff platelets and through the continuous compliant matrix. Simple energy principles predict that a crack will choose the path of least resistance, *i.e.* the most energetically favorable path. Furthermore, by applying linear elastic fracture mechanics to the sample at hand one

realizes that in order to satisfy the above principle, the crack path will result as a trade-off between the minimum crack deflection angle and the path of least stiffness. Figure 33c shows that the crack, initially propagates perpendicularly to its original orientation, choosing a longer path and propagating exclusively through the compliant matrix with stable crack propagation as a result. By the considerations above, this toughness mechanism is clearly activated by the combination of the major stiffness mismatch between material **A** and material **B** and their specific topological arrangement.

Furthermore, in Figure 33d the boundary is seen to influence fracture propagation as its presence seemingly inhibits the initial mechanism, detailed above, to continue and the crack suddenly propagates through a set of rows of stiff platelets. At this point, the sample has incurred substantial damage, and platelets away from the crack tip break. Further confirmation is thus obtained that the stress field is strongly delocalized, indicating an efficient usage of the material throughout the sample. Furthermore, Figure 33e and f display repetitions of the initial fracture mechanism observed in Figure 33c and d. The composite exhibits impressive toughness (Figure 32a). The failure process exhibited by the bone-like sample, detailed here and portrayed in Figure 33, is reminiscent of the mechanical failure of natural mineralized composites [3, 6, 10, 17, 32]. In future studies, structures could be printed with more repeat units of the topological unit cells to avoid the boundary interfering with the fracture path.



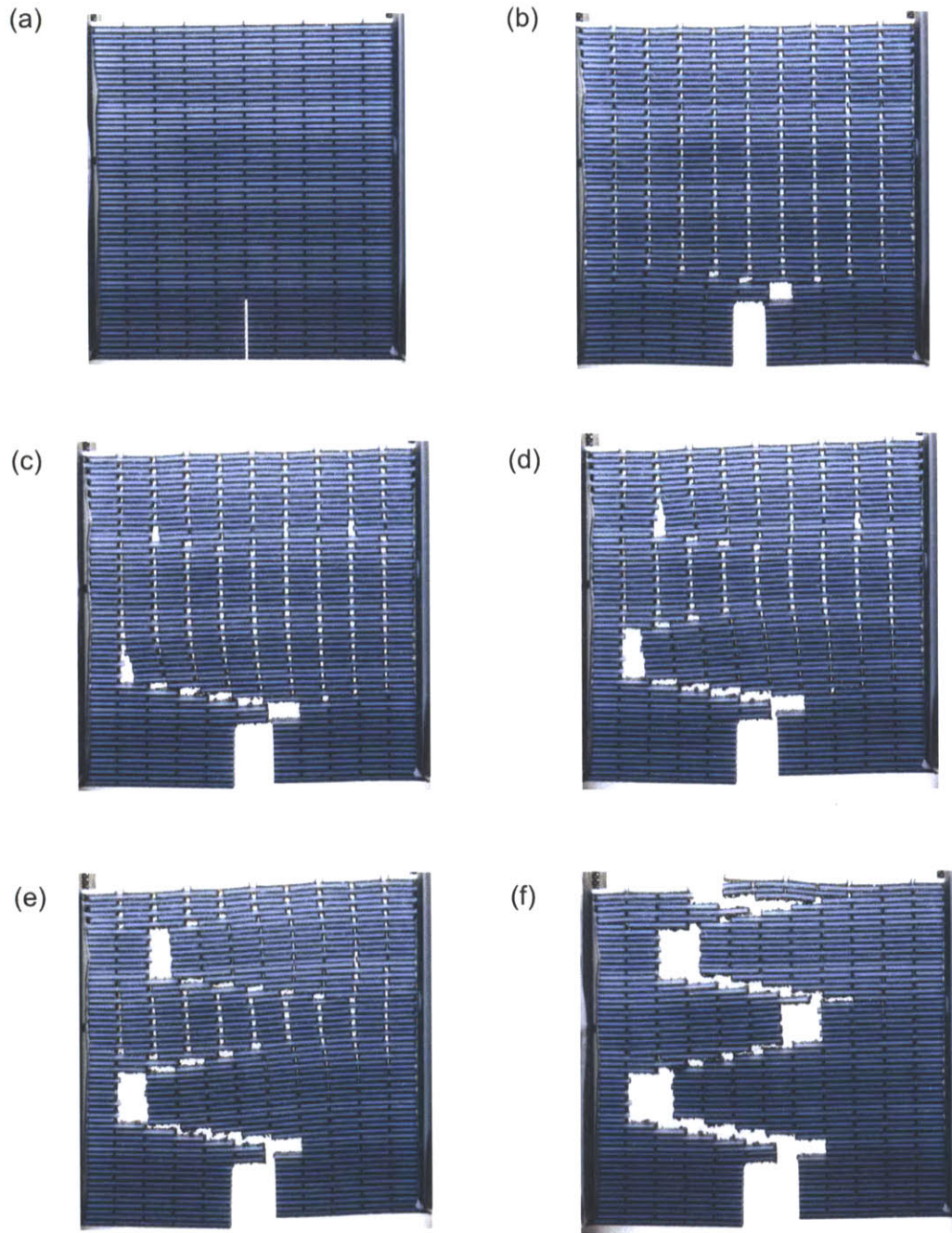


**Figure 33** Snapshots of fracture propagation in the synthesized bone-like specimen. Images clearly show two dominating toughening mechanisms exhibited by the printed composite. The second snapshot indicates a delocalized load transfer in the topology with damage being sustained away from the crack tip. Furthermore, a pronounced crack deflection mechanism is observed, induced by the particular topological arrangement of the two base materials with widely contrasting constitutive behavior. This causes the crack to take a long path through the specimen thus dissipating large amounts of energy on the way. Moreover, as the fracture mainly propagates through the extremely compliant base material B the crack is blunted, leading to a lesser stress concentration at the crack tip and thus stable fracture propagation.

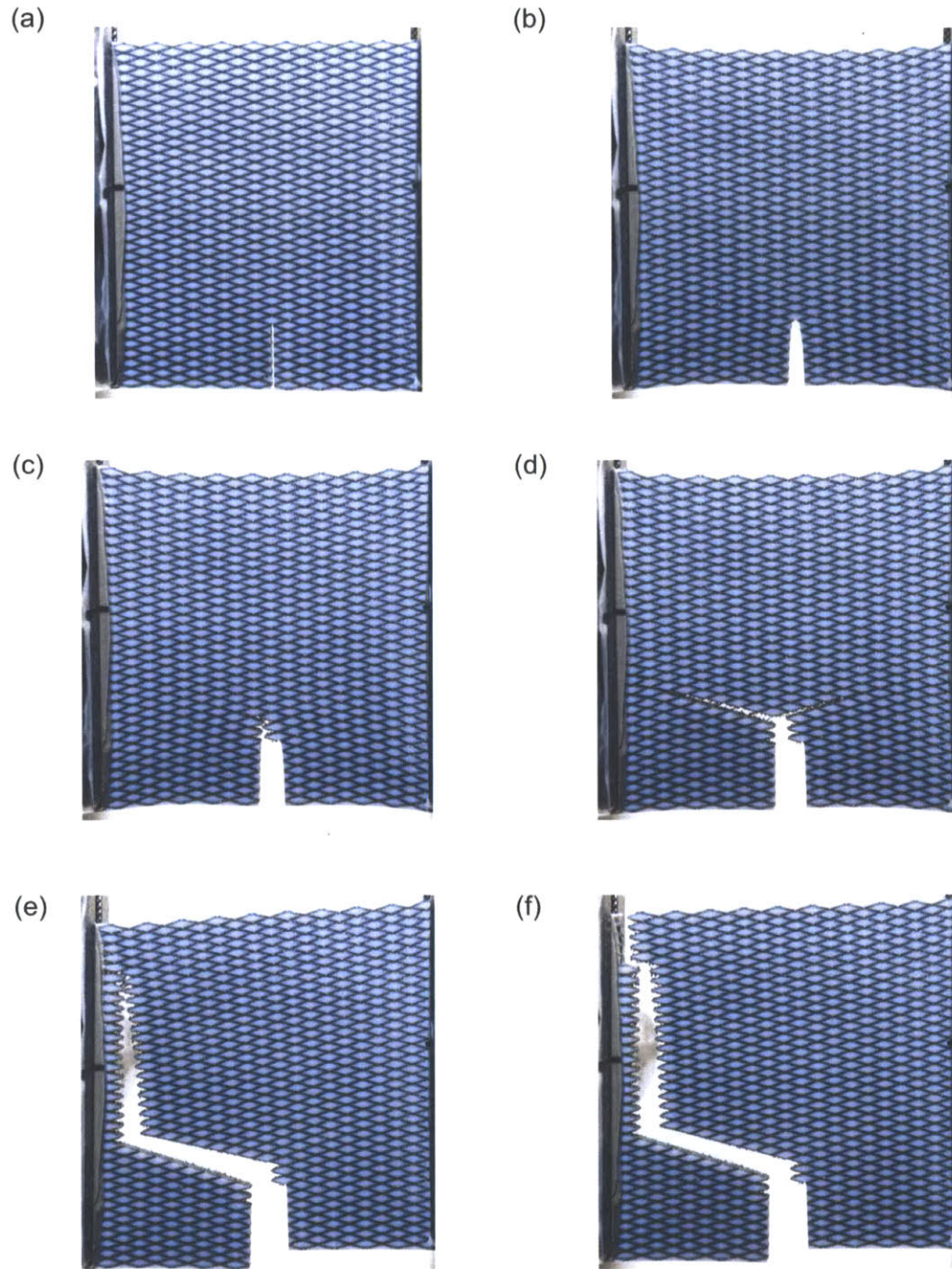


**Figure 34** Snapshots of fracture propagation in the synthesized rotated bone-like specimen. The second snapshot indicates the significant deformability of the composite in the presence of the crack; an apparent blunting of the crack-tip highlights this. Furthermore, the characteristic zigzag pattern of fracture propagation in panel (c) is observed, made possible by the extreme compliance of the matrix phase combined with the specific composite topology. As the eccentricity of the applied load increases crack branching is observed (d), followed by a dominating crack propagating to and along the boundary in panel (e) resulting in complete failure of the composite.



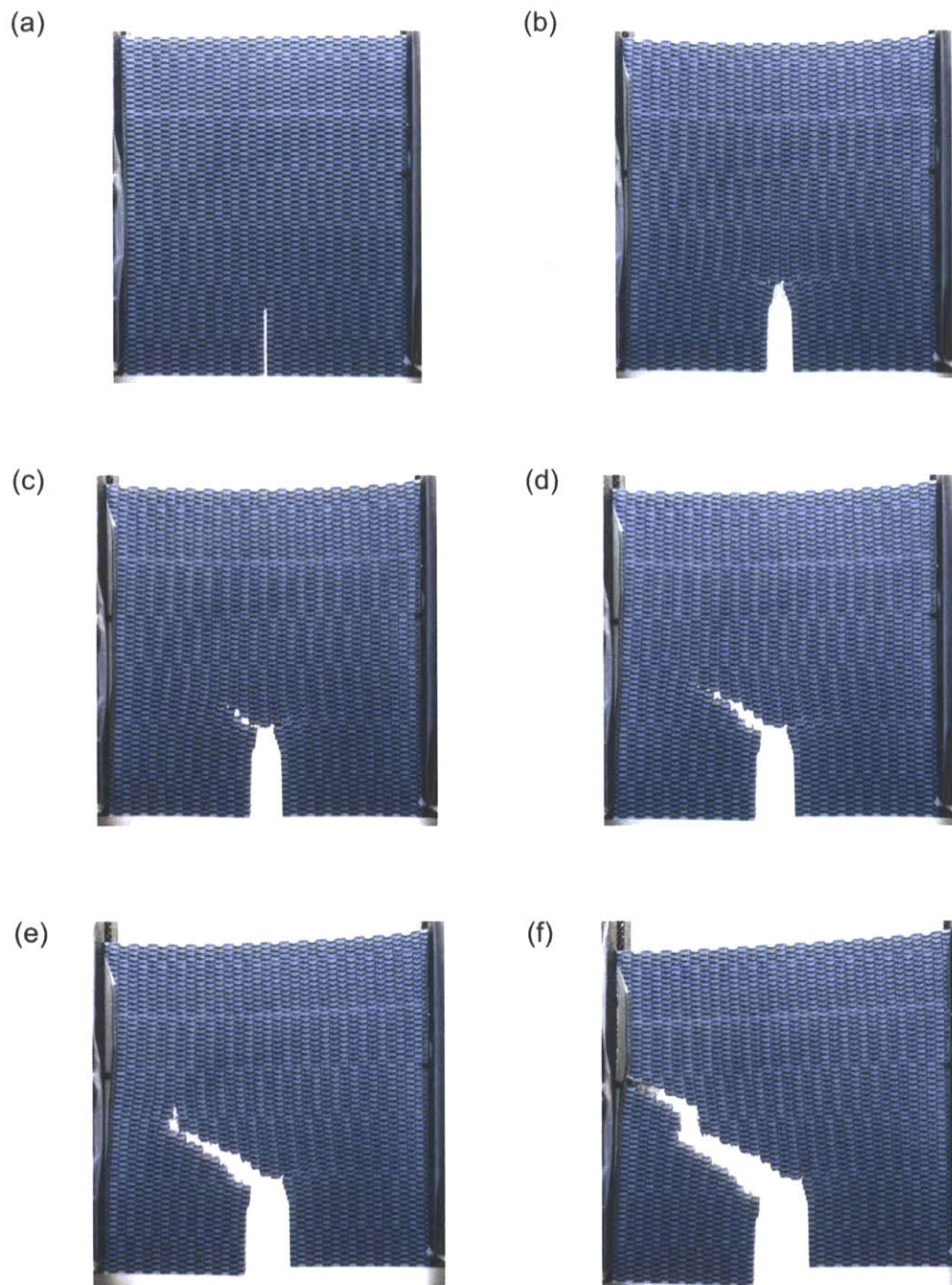


**Figure 35** Snapshots of fracture propagation in the bio-calcite like specimen. As for the rotated bone-like specimen the specimen is observed to undergo significant deformation prior to major crack propagation, enabled by the crack-tip blunting displayed in panel (b), this was also highlighted in Figure 5. In panel (c) the crack has started to propagate towards the boundary and eventually reaches it in panel (f). The crack propagates slowly through the sample undergoing significant deformation in the process. It is clearly observed that the compliant phase influences the crack propagation path and leads to toughening in the composite indicated by the resulting rough fracture surface.

### **6.2.2.2 The rotated bone-like topology**

Figure 34 displays the fracture process in the rotated bone-like specimen. The influence of the compliant phase in postponing the main fracture event through blunting of the crack tip is clearly visualized in Figure 34b. As the stress concentration scales with the inverse square root of crack tip radius, the compliant phase acts to reduce the intensity of the stress field at the notch. Upon reaching a critical deformation the fracture propagates and does so in a characteristic zigzag pattern. Again, as for the bone-like specimen, it is energetically more favorable for the crack to propagate through the compliant matrix and thus is forced through the longer route around the stiff rhombus shaped inclusions, contributing to additional energy dissipation. As the crack propagates, the eccentricity of the applied load increases, resulting in additional moment loading on the sample. This leads to crack branching, where the fracture propagates from the crack tip along diagonals through the compliant matrix (Figure 34d). Eventually, one of the crack branches starts to dominate and propagates through to the boundary quickly resulting in complete failure of the composite (Figure 34e, f).

### **6.2.2.3 The bio-calcite-like topology**

Finally, snapshots of the complete fracture process in the bio-calcite-like specimen are presented in Figure 35. Unlike the bone-like specimen and the rotated bone-like specimen, in the bio-calcite-like topology the stiff phase is the matrix. This has a marked effect on crack propagation. There is no continuous soft phase for fracture to propagate through and it is thus forced to move through the stiffer matrix. The crack attempts to minimize the distance it travels through the stiffer phase thus resulting in a rugged fracture surface, the fracture propagates in a staccato like manner with consecutive crack arrest and crack propagation. Eventually the crack propagates into the boundary and the specimen is unloaded. As is displayed in Figure 32a, these mechanisms lead to the impressive fracture mechanical characteristics of the specimen, a toughness modulus eight times that of the toughest constituent material.

## **6.3 Conclusions and outlook**

Here, 3D printed composites were printed whose fracture mechanical behavior agreed well with the predictions obtained by simulation. Notably, the synthesized composites

exhibited fracture mechanical properties such as toughness modulus an order of magnitude larger than their fundamental building blocks. By printing composites from base materials (that have widely contrasting constitutive behavior and which each exhibit brittle fracture behavior) in specific topological arrangements, structures that feature significant toughening mechanisms and stable crack propagation were created.

Further studies to understand the connection between experimental and computational results are needed, including an analysis of the effects of different stiffness ratios between the two phases. Moreover, several refinements have been identified here, both to the manufacturing process and the computational modeling, which could improve the agreement between simulation and experiment, thereby resulting in a system in which the designer can more accurately design composite materials with the required mechanical properties.

## 7 Discussion and Conclusion

With the aim of optimizing synthetic material design and creating high performance materials at a low cost it is essential to exploit the full potential of every design principle employed, where the designs developed based on such paradigms encompass a merger of the concepts of structure and material [130] and could find widespread applications that range from architecture [131] to the design of innovative surfaces [132] or novel impact mitigating materials [133]. In this work biological mineralized composites have been investigated at a fundamental level providing novel insight into powerful design principles. By investigating mesoscale hierarchical structures with brittle silica as the fundamental building block and with inspiration from biomineralized composites the precise topological ordering of stiff and soft phases was identified as a powerful structural design mechanism. Computational simulations exemplified that appropriate architectures could render flawed composites far less sensitive to cracks with a notched bone-like topology retaining almost 70% of its theoretical strength, as compared to the mere 30% retained by flawed bulk silica. Moreover, a rotated bone-like topology was introduced, capable of transferring both longitudinal and shear strain continuously throughout its area virtually unaffected by a crack. Computational single edge notched tensile tests revealed that this highly delocalized strain field induced stable crack propagation in the composites composed solely of silica. Furthermore, composites with a single geometrical ordering with model materials as constituents were designed to investigate the fundamentals controlling the interactions between composite constituents. A detailed study revealed that simple elastic interactions were sufficient to conceive a composite with a fracture toughness modulus eight times larger than its constituents. Additionally, it was shown that such simple interactions composites could be designed that spanned an Ashby area of toughness and stiffness in a very similar fashion as biocomposites, namely characterized by a concave curve. These results indicated that elucidated elastic interactions, defined through a stiffness ratio, indeed might be essential design mechanisms employed by nature. Finally, having identified key aspects of biomineralized materials with essential contributions to their advanced fracture

mechanical properties, three-dimensional printing was employed as a rapid manufacturing technique to synthesize the designed composites. The knowledge of the influence of topological arrangements was combined with insights on the potential of optimal stiffness ratios to produce robust systems free of stress concentrations to synthesize bio-inspired composites with fracture toughness moduli an order of magnitude larger than the fundamental building blocks. Moreover, the predictive power of the employed computational tools was exhibited by the agreement in deformation and fracture mechanisms observed in experiment and simulation as well as the similar trends in fracture mechanical material properties exhibited by the two methods.

The approach adopted in this thesis provides an exciting outlook for future material and structure design, especially in the context of producing composite systems with superior fracture mechanical characteristics. Indeed the ability to predict optimal design of composites and print them rapidly at fine length scales is very intriguing and certainly, with refinements to both the computational approach and the synthesis a better quantitative predictive behavior can be obtained. The research presented here represents a first iteration on this approach and with many potential refinements to the employed methods already identified the potential in this new realm of design is clearly large. As 3D printers evolve, designers will seize more control over the manufacturing process allowing composites to be synthesized at even finer length scales, with more details and increased control of constituent material properties, opening the doors for the rapid manufacturing of structurally advanced complex multi-hierarchy biomimetic materials with applications in a large range of engineering disciplines. Certain specialized three-dimensional printers are already able to print structures at nanoscale resolution. Combining this capability with multi-material printing technology and possibly even allowing the simultaneous printing of biomimetic proteinaceous engineered materials could clearly open a whole new design space for multipurpose materials. Wild ideas such as nanoengineered concrete, with dispersions of mechanotunable proteinaceous organics, exhibiting fracture toughness and strength far superior to conventional concrete suddenly seems more realizable.

Further research should focus on exploring the limits of 3D printing and improving the predictive capability of the computational models. While pushing 3D printing technology further will lead to the ability to create far more complex structures, the refinement of the computational tools and models will narrow the gap between prediction and reality thus empowering the design process immensely. As other current manufacturing processes, 3D printing is indubitably exposed to uncertainty and inaccuracies. On this note, stochastic computational models may thus play an important role in the context of uncertainty quantification and the direct modeling of heterogeneity. The possible improvements of the methods are as the potential of the approach, vast. Future work on these topics could have sustainable impacts on a range of engineering disciplines.

# Bibliography

- [1] J. Aizenberg, J. C. Weaver, M. S. Thanawala, V. C. Sundar, D. E. Morse, and P. Fratzl, Skeleton of *Euplectella* sp.: Structural hierarchy from the nanoscale to the macroscale. *Science*, **2005**, 309, 5732.
- [2] N. Almqvist, Y. Delamo, B. L. Smith, N. H. Thomson, Å. Bartholdson, R. Lal, M. Brzezinski, and P. K. Hansma, Micromechanical and structural properties of a pennate diatom investigated by atomic force microscopy. *Journal of Microscopy*, **2001**, 202, 3.
- [3] F. Barthelat, Nacre from mollusk shells: a model for high-performance structural materials. *Bioinspir Biomim*, **2010**, 5, 3.
- [4] M. J. Buehler, Molecular nanomechanics of nascent bone: fibrillar toughening by mineralization. *Nanotechnology*, **2007**, 18, 29.
- [5] M. J. Buehler, Tuning weakness to strength. *Nano Today*, **2010**, 5, 5.
- [6] P. Fratzl, H. S. Gupta, E. P. Paschalis, and P. Roschger, Structure and mechanical quality of the collagen-mineral nano-composite in bone. *J Mater Chem*, **2004**, 14, 14.
- [7] H. S. Gupta, J. Seto, W. Wagermaier, P. Zaslansky, P. Boesecke, and P. Fratzl, Cooperative deformation of mineral and collagen in bone at the nanoscale. *P Natl Acad Sci USA*, **2006**, 103, 47.
- [8] C. E. Hamm, R. Merkel, O. Springer, P. Jurkojc, C. Maier, K. Prechtel, and V. Smetacek, Architecture and material properties of diatom shells provide effective mechanical protection. *Nature*, **2003**, 421, 6925.
- [9] G. Mayer, Rigid biological systems as models for synthetic composites. *Science*, **2005**, 310, 5751.
- [10] J. Y. Rho, L. Kuhn-Spearing, and P. Zioupos, Mechanical properties and the hierarchical structure of bone. *Med Eng Phys*, **1998**, 20, 2.
- [11] M. J. Buehler and T. Ackbarow, Fracture mechanics of protein materials. *Mater Today*, **2007**, 10, 9.
- [12] H. Gupta, S. Krauss, J. Seto, W. Wagermaier, M. Kerschnitzki, G. Benecke, P. Zaslansky, P. Boesecke, S. S. Funari, H. O. K. Kirchner, and P. Fratzl, Nanoscale deformation mechanisms in bone. *Bone*, **2009**, 44,
- [13] A. Miserez, J. C. Weaver, P. J. Thurner, J. Aizenberg, Y. Dauphin, P. Fratzl, D. E. Morse, and F. W. Zok, Effects of laminate architecture on fracture resistance of sponge biosilica: Lessons from nature. *Adv Funct Mater*, **2008**, 18, 8.
- [14] K. Oaki and H. Imai, The hierarchical architecture of nacre and its mimetic material. *Angew Chem Int Edit*, **2005**, 44, 40.
- [15] H. Peterlik, P. Roschger, K. Klaushofer, and P. Fratzl, From brittle to ductile fracture of bone. *Nat Mater*, **2006**, 5, 1.
- [16] S. Weiner and H. D. Wagner, The material bone: Structure mechanical function relations. *Annu Rev Mater Sci*, **1998**, 28,
- [17] S. Kamat, X. Su, R. Ballarini, and A. H. Heuer, Structural basis for the fracture toughness of the shell of the conch *Strombus gigas*. *Nature*, **2000**, 405, 6790.
- [18] H. Kessler, R. Ballarini, R. L. Mullen, L. Spearing, and A. H. Heuer, A biomimetic example of brittle toughening .1. Steady state multiple cracking (vol 5, pg 157, 1996). *Comp Mater Sci*, **1996**, 6, 4.



- [19] M. Sumper, A phase separation model for the nanopatterning of diatom biosilica. *Science*, **2002**, 295, 5564.
- [20] R. Ballarini, R. Kayacan, F. J. Ulm, T. Belytschko, and A. H. Heuer, Biological structures mitigate catastrophic fracture through various strategies. *Int J Fracture*, **2005**, 135, 1-4.
- [21] M. J. Buehler and Z. P. Xu, Materials Science Mind the Helical Crack. *Nature*, **2010**, 464, 7285.
- [22] B. J. F. Bruet, J. H. Song, M. C. Boyce, and C. Ortiz, Materials design principles of ancient fish armour. *Nat Mater*, **2008**, 7, 9.
- [23] J. D. Currey, Materials science - Hierarchies in biomineral structures. *Science*, **2005**, 309, 5732.
- [24] P. Fratzl and R. Weinkamer, Nature's hierarchical materials. *Prog Mater Sci*, **2007**, 52, 8.
- [25] M. A. Meyers, P. Y. Chen, A. Y. M. Lin, and Y. Seki, Biological materials: Structure and mechanical properties. *Prog Mater Sci*, **2008**, 53, 1.
- [26] H. J. Gao, B. H. Ji, I. L. Jager, E. Arzt, and P. Fratzl, Materials become insensitive to flaws at nanoscale: Lessons from nature. *P Natl Acad Sci USA*, **2003**, 100, 10.
- [27] A. P. Garcia, N. Pugno, and M. J. Buehler, Superductile, Wavy Silica Nanostructures Inspired by Diatom Algae. *Adv Eng Mater*, **2011**, 13, 10.
- [28] B. H. Ji and H. J. Gao, Mechanical properties of nanostructure of biological materials. *J Mech Phys Solids*, **2004**, 52, 9.
- [29] B. H. Ji and H. J. Gao, A study of fracture mechanisms in biological nanocomposites via the virtual internal bond model. *Mat Sci Eng a-Struct*, **2004**, 366, 1.
- [30] D. Sen and M. J. Buehler, Atomistically-Informed Mesoscale Model of Deformation and Failure of Bioinspired Hierarchical Silica Nanocomposites. *Int J Appl Mech*, **2010**, 2, 4.
- [31] D. Sen and M. J. Buehler, Structural hierarchies define toughness and defect-tolerance despite simple and mechanically inferior brittle building blocks. *Sci Rep-Uk*, **2011**, 1,
- [32] P. Fratzl, H. S. Gupta, F. D. Fischer, and O. Kolednik, Hindered crack propagation in materials with periodically varying Young's modulus - Lessons from biological materials. *Adv Mater*, **2007**, 19, 18.
- [33] K. Okumura and P. G. de Gennes, Why is nacre strong? Elastic theory and fracture mechanics for biocomposites with stratified structures. *Eur Phys J E*, **2001**, 4, 1.
- [34] B. L. Smith, T. E. Schaffer, M. Viani, J. B. Thompson, N. A. Frederick, J. Kindt, A. Belcher, G. D. Stucky, D. E. Morse, and P. K. Hansma, Molecular mechanistic origin of the toughness of natural adhesives, fibres and composites. *Nature*, **1999**, 399, 6738.
- [35] G. E. Fantner, T. Hassenkam, J. H. Kindt, J. C. Weaver, H. Birkedal, L. Pechenik, J. A. Cutroni, G. A. G. Cidade, G. D. Stucky, D. E. Morse, and P. K. Hansma, Sacrificial bonds and hidden length dissipate energy as mineralized fibrils separate during bone fracture. *Nat Mater*, **2005**, 4, 8.

- [36] R. Z. Wang, Z. Suo, A. G. Evans, N. Yao, and I. A. Aksay, Deformation mechanisms in nacre. *J Mater Res*, **2001**, 16, 9.
- [37] G. Decher, J. D. Hong, and J. Schmitt, Buildup of Ultrathin Multilayer Films by a Self-Assembly Process .3. Consecutively Alternating Adsorption of Anionic and Cationic Polyelectrolytes on Charged Surfaces. *Thin Solid Films*, **1992**, 210, 1-2.
- [38] W. Tan and T. A. Desai, Layer-by-layer microfluidics for biomimetic three-dimensional structures. *Biomaterials*, **2004**, 25, 7-8.
- [39] Z. Y. Tang, N. A. Kotov, S. Magonov, and B. Ozturk, Nanostructured artificial nacre. *Nat Mater*, **2003**, 2, 6.
- [40] Z. Y. Tang, Y. Wang, P. Podsiadlo, and N. A. Kotov, Biomedical applications of layer-by-layer assembly: From biomimetics to tissue engineering. *Adv Mater*, **2006**, 18, 24.
- [41] Y. Wang, A. S. Angelatos, and F. Caruso, Template synthesis of nanostructured materials via layer-by-layer assembly. *Chem Mater*, **2008**, 20, 3.
- [42] S. M. Douglas, H. Dietz, T. Liedl, B. Hogberg, F. Graf, and W. M. Shih, Self-assembly of DNA into nanoscale three-dimensional shapes. *Nature*, **2009**, 459, 7245.
- [43] J. D. Hartgerink, E. Beniash, and S. I. Stupp, Self-assembly and mineralization of peptide-amphiphile nanofibers. *Science*, **2001**, 294, 5547.
- [44] W. A. Lopes and H. M. Jaeger, Hierarchical self-assembly of metal nanostructures on diblock copolymer scaffolds. *Nature*, **2001**, 414, 6865.
- [45] G. M. Whitesides and B. Grzybowski, Self-assembly at all scales. *Science*, **2002**, 295, 5564.
- [46] G. Pahl and W. Beitz, Engineering design : a systematic approach 1996, London ; New York: Springer. xxx, 544 p.
- [47] A. P. Jackson, J. F. V. Vincent, and R. M. Turner, The Mechanical Design of Nacre. *P Roy Soc Lond B Bio*, **1988**, 234, 1277.
- [48] A. Bergander and L. Salmen, Cell wall properties and their effects on the mechanical properties of fibers. *J Mater Sci*, **2002**, 37, 1.
- [49] L. Han, L. F. Wang, J. H. Song, M. C. Boyce, and C. Ortiz, Direct Quantification of the Mechanical Anisotropy and Fracture of an Individual Exoskeleton Layer via Uniaxial Compression of Micropillars. *Nano Lett*, **2011**, 11, 9.
- [50] J. W. C. Dunlop and P. Fratzl, Biological Composites. *Annual Review of Materials Research*, Vol 40, **2010**, 40,
- [51] C. Darwin, The origin of species by means of natural selection, or, The preservation of favored races in the struggle for life 1896, New York: D. Appleton.
- [52] Y. Bar-Cohen, Biomimetics : biologically inspired technologies 2006, Boca Raton, FL: CRC/Taylor & Francis. xviii, 527 p., 32 p. of plates.
- [53] J. M. Benyus, Biomimicry : innovation inspired by nature. 1st ed 1997, New York: Morrow. 308 p.
- [54] M. Sarikaya, C. Tamerler, A. K. Y. Jen, K. Schulten, and F. Baneyx, Molecular biomimetics: nanotechnology through biology. *Nat Mater*, **2003**, 2, 9.
- [55] K. Autumn, Y. A. Liang, S. T. Hsieh, W. Zesch, W. P. Chan, T. W. Kenny, R. Fearing, and R. J. Full, Adhesive force of a single gecko foot-hair. *Nature*, **2000**, 405, 6787.

- [56] F. Vollrath and D. P. Knight, Liquid crystalline spinning of spider silk. *Nature*, **2001**, 410, 6828.
- [57] T. S. Wong, S. H. Kang, S. K. Y. Tang, E. J. Smythe, B. D. Hatton, A. Grinthal, and J. Aizenberg, Bioinspired self-repairing slippery surfaces with pressure-stable omniphobicity. *Nature*, **2011**, 477, 7365.
- [58] S. G. Zhang, Emerging biological materials through molecular self-assembly. *Biotechnol Adv*, **2002**, 20, 5-6.
- [59] S. Weiner and L. Addadi, Design strategies in mineralized biological materials. *J Mater Chem*, **1997**, 7, 5.
- [60] J. M. Gosline, P. A. Guerette, C. S. Ortlepp, and K. N. Savage, The mechanical design of spider silks: From fibroin sequence to mechanical function. *J Exp Biol*, **1999**, 202, 23.
- [61] G. Falini, S. Albeck, S. Weiner, and L. Addadi, Control of aragonite or calcite polymorphism by mollusk shell macromolecules. *Science*, **1996**, 271, 5245.
- [62] J. C. Weaver, J. Aizenberg, G. E. Fantner, D. Kisailus, A. Woesz, P. Allen, K. Fields, M. J. Porter, F. W. Zok, P. K. Hansma, P. Fratzl, and D. E. Morse, Hierarchical assembly of the siliceous skeletal lattice of the hexactinellid sponge *Euplectella aspergillum*. *J Struct Biol*, **2007**, 158, 1.
- [63] D. Losic, J. G. Mitchell, and N. H. Voelcker, Diatomaceous Lessons in Nanotechnology and Advanced Materials. *Adv Mater*, **2009**, 21, 29.
- [64] F. Barthelat and H. D. Espinosa, An experimental investigation of deformation and fracture of nacre-mother of pearl. *Exp Mech*, **2007**, 47, 3.
- [65] D. Losic, K. Short, J. G. Mitchell, R. Lal, and N. H. Voelcker, AFM nanoindentations of diatom biosilica surfaces. *Langmuir*, **2007**, 23, 9.
- [66] G. A. Jeffrey, An introduction to hydrogen bonding. Topics in physical chemistry 1997, New York: Oxford University Press. vii, 303 p.
- [67] P. E. Marszalek, H. Lu, H. B. Li, M. Carrion-Vazquez, A. F. Oberhauser, K. Schulten, and J. M. Fernandez, Mechanical unfolding intermediates in titin modules. *Nature*, **1999**, 402, 6757.
- [68] F. Song, A. K. Soh, and Y. L. Bai, Structural and mechanical properties of the organic matrix layers of nacre. *Biomaterials*, **2003**, 24, 20.
- [69] R. Menig, M. H. Meyers, M. A. Meyers, and K. S. Vecchio, Quasi-static and dynamic mechanical response of *Haliotis rufescens* (abalone) shells. *Acta Mater*, **2000**, 48, 9.
- [70] P. Roschger, B. M. Grabner, S. Rinnerthaler, W. Tesch, M. Kneissel, A. Berzlanovich, K. Klaushofer, and P. Fratzl, Structural development of the mineralized tissue in the human L4 vertebral body. *J Struct Biol*, **2001**, 136, 2.
- [71] W. J. Landis, The Strength of a Calcified Tissue Depends in Part on the Molecular-Structure and Organization of Its Constituent Mineral Crystals in Their Organic Matrix. *Bone*, **1995**, 16, 5.
- [72] W. J. Landis, K. J. Hodgins, M. J. Song, J. Arena, S. Kiyonaga, M. Marko, C. Owen, and B. F. McEwen, Mineralization of collagen may occur on fibril surfaces: Evidence from conventional and high-voltage electron microscopy and three-dimensional imaging. *J Struct Biol*, **1996**, 117, 1.

- [73] M. J. Xu, G. M. Gratson, E. B. Duoss, R. F. Shepherd, and J. A. Lewis, Biomimetic silicification of 3D polyamine-rich scaffolds assembled by direct ink writing. *Soft Matter*, **2006**, 2, 3.
- [74] W. Suchanek and M. Yoshimura, Processing and properties of hydroxyapatite-based biomaterials for use as hard tissue replacement implants. *J Mater Res*, **1998**, 13, 1.
- [75] A. Gautieri, S. Vesentini, A. Redaelli, and M. J. Buehler, Viscoelastic properties of model segments of collagen molecules. *Matrix Biol*, **2012**, 31, 2.
- [76] P. Fratzl, K. Misof, I. Zizak, G. Rapp, H. Amenitsch, and S. Bernstorff, Fibrillar structure and mechanical properties of collagen. *J Struct Biol*, **1998**, 122, 1-2.
- [77] J. D. Currey, Mechanical-Properties of Mother of Pearl in Tension. *P Roy Soc Lond B Bio*, **1977**, 196, 1125.
- [78] J. B. Phelps, G. B. Hubbard, X. Wang, and C. M. Agrawal, Microstructural heterogeneity and the fracture toughness of bone. *J Biomed Mater Res*, **2000**, 51, 4.
- [79] T. L. Norman, D. Vashishth, and D. B. Burr, Fracture-Toughness of Human Bone under Tension. *J Biomech*, **1995**, 28, 3.
- [80] C. Levi, J. L. Barton, C. Guillemet, E. Lebras, and P. Lehuède, A Remarkably Strong Natural Glassy Rod - the Anchoring Spicule of the Monorhaphis Sponge. *J Mater Sci Lett*, **1989**, 8, 3.
- [81] M. Hildebrand, Diatoms, biomineralization processes, and genomics. *Chemical Reviews*, **2008**, 108, 11.
- [82] D. Losic, R. J. Pillar, T. Dilger, J. G. Mitchell, and N. H. Voelcker, Atomic force microscopy (AFM) characterisation of the porous silica nanostructure of two centric diatoms. *J Porous Mat*, **2007**, 14, 1.
- [83] J. C. Weaver, L. I. Pietrasanta, N. Hedin, B. F. Chmelka, P. K. Hansma, and D. E. Morse, Nanostructural features of demosponge biosilica. *J Struct Biol*, **2003**, 144, 3.
- [84] I. C. Gebeshuber, J. H. Kindt, J. B. Thompson, Y. Del Amo, H. Stachelberger, M. A. Brzezinski, G. D. Stucky, D. E. Morse, and P. K. Hansma, Atomic force microscopy study of living diatoms in ambient conditions. *J Microsc-Oxford*, **2003**, 212,
- [85] I. C. Gebeshuber, H. Stachelberger, and M. Drack, Diatom bionanotribology-biological surfaces in relative motion: Their design, friction, adhesion, lubrication and wear. *J Nanosci Nanotechnol*, **2005**, 5, 1.
- [86] H. A. Simon, The Architecture of Complexity. *Proceedings of the American philosophical society*, **1962**, 106, 6.
- [87] S. Keten, Z. P. Xu, B. Ihle, and M. J. Buehler, Nanoconfinement controls stiffness, strength and mechanical toughness of beta-sheet crystals in silk. *Nat Mater*, **2010**, 9, 4.
- [88] M. Sumper and E. Brunner, Learning from diatoms: Nature's tools for the production of nanostructured silica. *Adv Funct Mater*, **2006**, 16, 1.
- [89] F. Noll, M. Sumper, and N. Hampp, Nanostructure of diatom silica surfaces and of biomimetic analogues. *Nano Lett*, **2002**, 2, 2.

- [90] F. Barthelat, H. Tang, P. D. Zavattieri, C. M. Li, and H. D. Espinosa, On the mechanics of mother-of-pearl: A key feature in the material hierarchical structure. *J Mech Phys Solids*, **2007**, 55, 2.
- [91] W. A. Curtin and H. Scher, Mechanics Modeling Using a Spring Network. *J Mater Res*, **1990**, 5, 3.
- [92] H. J. Gao and P. Klein, Numerical simulation of crack growth in an isotropic solid with randomized internal cohesive bonds. *J Mech Phys Solids*, **1998**, 46, 2.
- [93] G. N. Hassold and D. J. Srolovitz, Brittle-Fracture in Materials with Random Defects. *Phys Rev B*, **1989**, 39, 13.
- [94] P. D. Beale and D. J. Srolovitz, Elastic Fracture in Random Materials. *Phys Rev B*, **1988**, 37, 10.
- [95] W. A. Curtin and H. Scher, Brittle-Fracture in Disordered Materials - a Spring Network Model. *J Mater Res*, **1990**, 5, 3.
- [96] M. Sahimi and J. D. Goddard, Elastic Percolation Models for Cohesive Mechanical Failure in Heterogeneous Systems. *Phys Rev B*, **1986**, 33, 11.
- [97] A. P. Garcia, D. Sen, and M. J. Buehler, Hierarchical Silica Nanostructures Inspired by Diatom Algae Yield Superior Deformability, Toughness, and Strength. *Metall Mater Trans A*, **2011**, 42A, 13.
- [98] M. J. Buehler, Atomistic modeling of materials failure 2008, New York: Springer.
- [99] M. S. Daw and M. I. Baskes, Embedded-Atom Method - Derivation and Application to Impurities, Surfaces, and Other Defects in Metals. *Phys Rev B*, **1984**, 29, 12.
- [100] R. Z. Wang and H. S. Gupta, Deformation and Fracture Mechanisms of Bone and Nacre. *Annu Rev Mater Res*, **2011**, 41,
- [101] D. H. Tsai, Virial Theorem and Stress Calculation in Molecular-Dynamics. *J Chem Phys*, **1979**, 70, 3.
- [102] M. Zhou, A new look at the atomic level virial stress: on continuum-molecular system equivalence. *P Roy Soc Lond a Mat*, **2003**, 459, 2037.
- [103] A. K. Subramaniyan and C. T. Sun, Continuum interpretation of virial stress in molecular simulations. *Int J Solids Struct*, **2008**, 45, 14-15.
- [104] W. G. Hoover, C. G. Hoover, and J. F. Lutsko, Microscopic and macroscopic stress with gravitational and rotational forces. *Phys Rev E*, **2009**, 79, 3.
- [105] L. E. Malvern, Introduction to the mechanics of a continuous medium. Prentice-Hall series in engineering of the physical sciences 1969, Englewood Cliffs, N.J.,: Prentice-Hall. xii, 713 p.
- [106] J. E. Marsden and T. J. R. Hughes, Mathematical foundations of elasticity. Prentice-Hall civil engineering and engineering mechanics series 1983, Englewood Cliffs, N.J.: Prentice-Hall. xviii, 556 p.
- [107] M. E. Gurtin, E. Fried, and L. Anand, The mechanics and thermodynamics of continua 2010, New York: Cambridge University Press. xxi, 694 p.
- [108] M. F. Horstemeyer and M. I. Baskes, Strain tensors at the atomic scale. *Mater Res Soc Symp P*, **2000**, 578,
- [109] J. A. Zimmerman, D. J. Bammann, and H. J. Gao, Deformation gradients for continuum mechanical analysis of atomistic simulations. *Int J Solids Struct*, **2009**, 46, 2.

- [110] P. M. Gullett, M. F. Horstemeyer, M. I. Baskes, and H. Fang, A deformation gradient tensor and strain tensors for atomistic simulations. *Model Simul Mater Sc*, **2008**, 16, 1.
- [111] T. Belytschko, Y. Y. Lu, and L. Gu, Element-Free Galerkin Methods. *Int J Numer Meth Eng*, **1994**, 37, 2.
- [112] S. L. Zhang, R. Khare, Q. Lu, and T. Belytschko, A bridging domain and strain computation method for coupled atomistic-continuum modelling of solids. *Int J Numer Meth Eng*, **2007**, 70, 8.
- [113] H. Tada, P. C. Paris, and G. R. Irwin, The stress analysis of cracks handbook. 3rd ed2000, New York: ASME Press. xx, 677 p.
- [114] J. G. Swadener, M. I. Baskes, and M. Nastasi, Molecular dynamics simulation of brittle fracture in silicon. *Phys Rev Lett*, **2002**, 89, 8.
- [115] M. J. Buehler, A. C. van Duin, and W. A. Goddard, 3rd, Multiparadigm modeling of dynamical crack propagation in silicon using a reactive force field. *Phys Rev Lett*, **2006**, 96, 9.
- [116] N. Kroger and K. H. Sandhage, From Diatom Biomolecules to Bioinspired Syntheses of Silica- and Titania-Based Materials. *Mrs Bull*, **2010**, 35, 2.
- [117] P. Podsiadlo, A. K. Kaushik, E. M. Arruda, A. M. Waas, B. S. Shim, J. D. Xu, H. Nandivada, B. G. Pumplin, J. Lahann, A. Ramamoorthy, and N. A. Kotov, Ultrastrong and stiff layered polymer nanocomposites. *Science*, **2007**, 318, 5847.
- [118] J. R. Rice, A Path Independent Integral and Approximate Analysis of Strain Concentration by Notches and Cracks. *J Appl Mech*, **1968**, 35, 2.
- [119] H. D. Espinosa, J. E. Rim, F. Barthelat, and M. J. Buehler, Merger of structure and material in nacre and bone - Perspectives on de novo biomimetic materials. *Prog Mater Sci*, **2009**, 54, 8.
- [120] D. Bak, Rapid prototyping or rapid production? 3D printing processes move industry towards the latter. *Assembly Autom*, **2003**, 23, 4.
- [121] D. Dimitrov, K. Schreve, and N. de Beer, Advances in three dimensional printing - state of the art and future perspectives. *Rapid Prototyping J*, **2006**, 12, 3.
- [122] H. Seitz, W. Rieder, S. Irsen, B. Leukers, and C. Tille, Three-dimensional printing of porous ceramic scaffolds for bone tissue engineering. *J Biomed Mater Res B*, **2005**, 74B, 2.
- [123] E. A. Roth, T. Xu, M. Das, C. Gregory, J. J. Hickman, and T. Boland, Inkjet printing for high-throughput cell patterning. *Biomaterials*, **2004**, 25, 17.
- [124] C. X. F. Lam, X. M. Mo, S. H. Teoh, and D. W. Hutmacher, Scaffold development using 3D printing with a starch-based polymer. *Mat Sci Eng C-Bio S*, **2002**, 20, 1-2.
- [125] K. F. Leong, C. M. Cheah, and C. K. Chua, Solid freeform fabrication of three-dimensional scaffolds for engineering replacement tissues and organs. *Biomaterials*, **2003**, 24, 13.
- [126] B. W. Miller, J. W. Moore, H. H. Barrett, T. Frye, S. Adler, J. Sery, and L. R. Furenlid, 3D printing in X-ray and gamma-ray imaging: A novel method for fabricating high-density imaging apertures. *Nucl Instrum Meth A*, **2011**, 659, 1.
- [127] A. Park, B. Wu, and L. G. Griffith, Integration of surface modification and 3D fabrication techniques to prepare patterned poly(L-lactide) substrates allowing regionally selective cell adhesion. *J Biomat Sci-Polym E*, **1998**, 9, 2.

- [128] Objet, *Objet Materials Data Sheet*, 2012.
- [129] Objet, *10 Reasons Why Multi-Material 3D Printing is Better for your Product Design & Development*, 2012.
- [130] M. J. Buehler and Y. C. Yung, Deformation and failure of protein materials in physiologically extreme conditions and disease. *Nat Mater*, **2009**, 8, 3.
- [131] J. Knippers and T. Speck, Design and construction principles in nature and architecture. *Bioinspir Biomim*, **2012**, 7, 1.
- [132] A. W. Lang, P. Motta, P. Hidalgo, and M. Westcott, Bristled shark skin: a microgeometry for boundary layer control? *Bioinspir Biomim*, **2008**, 3, 4.
- [133] S. W. Cranford, A. Tarakanova, N. M. Pugno, and M. J. Buehler, Nonlinear material behaviour of spider silk yields robust webs. *Nature*, **2012**, 482, 7383.



## 8 Appendix

### 8.1 List of figures

- Figure 1 Process flow of the approach used here. Starting from the simple model material building blocks composites are built with bio-inspired topologies. The bio-inspired composites are manufactured with 3D printing and proceed to test the synthesized specimens. The results are compared to model predictions. Electron microscopy image of fractured nacre surface is reprinted from <http://en.wikipedia.org/wiki/Nacre>. ..... 12
- Figure 2 (a) Schematic of the structure of bone showing plate-like crystals staggered in a collagen matrix. Figure adapted from [71], with permission from Elsevier. (b) SEM micrograph showing the staggered arrangement of aragonite platelets in nacre. A small volume fraction of organic material forms the matrix phase connecting the platelets, bar = 2  $\mu\text{m}$ . Figure adapted from [69], with permission from Elsevier. (c) SEM image of a fracture spicule revealing an organic interlayer, bar = 1  $\mu\text{m}$ . Figure adapted from [1], with from AAAS. .... 17
- Figure 3 (a) Details of the Western Pacific hexactinellid sponge, *Euplectella aspergillum*, and its skeleton. (A) Illustration (from Schulze, 1887) of two preserved specimens, clearly showing the holdfast apparatuses, the external ridge systems, and the terminal sieve plates. (B) Photograph of the underlying siliceous cylindrical skeletal lattice exposed by removal of the organic material. (C) At higher magnification, the square-grid architecture and regular ordering of the vertical and horizontal components of the skeletal system are clearly visible. Scale bars: A: 5 cm; B: 5 cm; C: 5mm. Figure reprinted from [62], with permission from Elsevier. (b) Images showing the broad diversity of diatom silica structures. (a) Bar = 1  $\mu\text{m}$ , (b) bar = 5  $\mu\text{m}$ , (c) bar = 10  $\mu\text{m}$ , (d) bar = 500 nm, (e) bar = 2  $\mu\text{m}$ , (f) bar = 10  $\mu\text{m}$ , (g) bar = 2  $\mu\text{m}$ , (h) bar = 2  $\mu\text{m}$ , (i) bar = 50  $\mu\text{m}$ , (j) bar = 2  $\mu\text{m}$ , (k) bar = 1  $\mu\text{m}$ , (l) bar = 10  $\mu\text{m}$ . Figure reprinted from [81], copyright © 2007, with permission from American Chemical Society. .... 19

Figure 4 Hierarchical structural organization of bone: (a) macrostructure: cortical and cancellous bone; (b) microstructure: osteons with Haversian systems; (c) sub-microstructure: lamellae; (d) nanostructure: collagen fiber assemblies of collagen fibrils; (e) sub-nanostructure: bone mineral crystals, collagen molecules, and non-collagenous proteins. Figure reprinted from [10], with permission of Elsevier. .... 21

Figure 5 Hierarchical structure of *Euplectella* sp. (A) Image of the entire structure, indicating cylindrical glass cage. Scale bar: 1 cm. (B) Close up of the cage structure portraying two square-grid lattices super imposed on each other at angled orientations. The arrows indicate stabilizing orthogonal ridges. Scale bar: 5 mm. (C) SEM image showing how each strut (enclosed by a bracket) is composed of a bundle of multiple spicules (arrow indicates the long axis of the skeletal lattice). Scale bar: 100  $\mu$ m. (D) SEM image showing the ceramic fiber-composite nature of a fractured and partially HF-etched single beam. Scale bar: 20  $\mu$ m. (E) SEM image showing the cemented nature of the HF-etched junction area. Scale bar: 25  $\mu$ m. (F) Contrast-enhanced SEM image of showing a cross section of a spicular strut. The micrograph reveals the large variety of sizes of spicule surrounded by a laminated silica matrix. Scale bar: 10  $\mu$ m. (G) SEM image of a spicule cross section, revealing the laminated structure. Scale bar: 5  $\mu$ m. (H) SEM of a fractured spicule, revealing an organic interlayer. Scale bar: 1  $\mu$ m. (I) Bleaching of biosilica surface revealing its consolidated nanoparticulate nature (25). Scale bar: 500 nm. Figure reprinted from [1], with permission of AAAS. .... 21

Figure 6 (A) SEM image of a silica shell (*Coscinodiscus* sp.). (B) Schematic showing the structural set-up of the valve. (C) High-resolution SEM images of a valve seen in planar view from below (areolae, cribra, and cribella) from *Coscinodiscus radiatus*. Scale bar: 2.5 mm. (D) to (G) shows a schematic drawing of the templating mechanism by the phase separation model proposed in [19]. (E) to (H) show SEM images of *C. wailesii* valves in the nascent state. (D) The monolayer of polyamine-containing droplets in close-packed arrangement within the SDV guides silica deposition. (E and F) Consecutive segregations of smaller (about 300 nm) droplets open new routes for silica precipitation. (G) Dispersion of 300-nm droplets into 50-nm droplets guides the final stage of silica deposition. Silica precipitation occurs

only within the water phase (white areas). The repeated phase separations produce a hierarchy of self-similar patterns. Figure reprinted from [19], with permission of AAAS.....	22
Figure 7 Hierarchically organized structure of the nacreous layer of the Japanese pearl <i>Pinctada fuctata</i> . a) FESEM image of the highest level of hierarchy. Scale bar: 1 $\mu\text{m}$ . b) FESEM image of the second hierarchical level. Scale bare: 100 nm. c) FETEM image of the lowest level of hierarchy, the nano building block. Scale bar: 10 nm. Panels d) to f) show corresponding schematic drawings of the three levels of hierarchy. Figure adapted from [14], with permission of WILEY-VCH. ....	23
Figure 8 Schematic overview of a spring bead triangular lattice system. The lattice is two-dimensional, matter is represented by discrete beads and the beads are connected to their nearest neighbors by springs. ....	26
Figure 9 (a) ReaxFF derived stress-strain response for two of the tested geometries in [97], bulk silica and nanoporous silica with sidewall thickness $w$ of 17 Å. Solid lines indicate lines of best fit. Figure adapted from [97] and reprinted with permission from the Nature Publishing Group.....	27
Figure 10 Schematic indicating two particles, $\alpha$ and $\beta$ , interacting across an imaginary surface CC' at which the virial stress is evaluated. ....	29
Figure 11 Comparison of longitudinal strain fields from the MLS and virial description. a) MLS derived strain field for unnotched case, b) virial strain field for unnotched case, c) MLS derived strain field for notched case, d) virial strain field for notched case. The field plots show very good agreement indicating that the MLS description of displacements and virial strain agree well in terms of longitudinal strain. ....	36
Figure 12 Geometries of specimens, here shown with size parameter $h = 6.48 \mu\text{m}$ . With the blue and gray phases representing the nanoporous and bulk silica, respectively, for (a) the bio-calcite-like geometry, (b) the bone-like geometry and (c) the rotated bone-like geometry. The specimens are loaded by imposing stepwise displacement on their right vertical faces, whilst holding the left hand sides still. Periodic boundary conditions are employed in the horizontal direction. (d) Constitutive laws for the nanoporous and bulk silica phase representing the compliant and brittle phase	

respectively in the material model (adapted from [31] with permission from Nature Publishing Group).....	40
Figure 13 (a) Stress-strain response for the bulk silica specimen, (b) the bio-calcite-like specimen, (c) the bone-like specimen and (d) the rotated bone-like specimen. Circular markers indicate the points at which the ultimate stress snapshots are taken. ....	44
Figure 14 Normalized strength as a function of specimen size for all four investigated systems. The strengths are normalized with respect to the respective strengths of the unnotched samples. ....	44
Figure 15 Von Mises stress fields for 6.48 $\mu$ m (a) unnotched bulk silica, (b) unnotched bio-calcite-like, (c) notched bulk silica, (d) notched bio-calcite-like, (e) unnotched bone-like, (f) unnotched rotated bone-like, (g) notched bone-like and (h) unnotched rotated bone-like specimens at the instant immediately prior to failure. The unnotched bulk silica specimen shows the expected even distribution of stress throughout the sample while the notched specimen exhibits the strong characteristic stress concentration at the crack tip. The specific topologies have a visible effect on the stress distribution in the composites and the bio-calcite-like and bone-like specimen both exhibit significant delocalization of stresses in their flawed state. Specifically in the bone-like system the load path in both specimens, notched and unnotched, is seen to be very similar. This specific hierarchical geometry alleviates the stress tip concentration and maintains the same mechanism of load transfer despite the presence of the crack, thus reducing the specimen's sensitivity to the notch.....	46
Figure 16 Plots comparing the stress distribution in the notched bulk geometry with the stress distribution within the strong particles of the (a) notched bio-calcite-like geometry, (b) the notched bone-like geometry and (c) the notched rotated bone-like geometry for the 6.48 $\mu$ m specimens. The plot clearly shows how the strong particles in the bio-calcite-like geometry and the bone-like geometry are significantly higher stressed than their counterparts in the bulk-silica specimen, thereby supporting the claim that the stronger phase in these structures is more	

efficiently utilized after the introduction of the notch than in their bulk silica counterpart. ....	47
Figure 17 (a) Longitudinal and (b) shear strain fields for unnotched bio-calcite-like geometry at the instant immediately prior to failure. (c) Longitudinal and (d) shear strain fields for notched bio-calcite-like geometry at the instant immediately prior to failure. (e) Longitudinal and (f) shear strain fields for unnotched bone-like geometry at the instant immediately prior to failure. (g) Longitudinal and (h) shear strain fields for notched bone-like geometry at the instant immediately prior to failure. (i) Longitudinal and (j) shear strain fields for unnotched rotated bone-like geometry at the instant immediately prior to failure. (k) Longitudinal and (l) shear strain fields for notched rotated bone-like geometry at the instant immediately prior to failure. ....	49
Figure 18 Crack propagation through the 23.78 $\mu$ m bio-calcite-like specimen. Snapshots are taken at (a) 2.15% strain, (b) 2.34% strain and maximum loading, (c) 2.36% strain and (d) 2.50% strain and immediately prior to complete failure of the specimen. Strain increments are 0.017%. To visualize details in the distribution of stresses the maximum limit of the color bar was lowered to 4000 MPa. ....	52
Figure 19 Crack propagation through the 23.78 $\mu$ m bone-like specimen. Snapshots are taken at (a) 3.16% strain and maximum loading, (b) 3.18% strain, (c) 3.21% strain and (d) 3.54% strain and immediately prior to complete failure of the specimen. Strain increments are 0.019%. To visualize details in the distribution of stresses the maximum limit of the color bar was lowered to 4000 MPa. ....	53
Figure 20 Snapshots showing stable crack propagation through the 23.78 $\mu$ m rotated bone-like specimen. Snapshots are taken at (a) 4.79% strain, (b) 5.17% strain, (c) 5.40% strain and (d) 5.54% strain and immediately prior to unstable crack propagation. Strain increments are 0.047%. To visualize details in the distribution of stresses the maximum limit of the color bar was lowered to 4000 MPa. ....	53
Figure 21 Longitudinal strain fields for 23.78 $\mu$ m (a) bulk-silica, (b) bio-calcite-like, (c) bone-like and (d) rotated bone-like notched specimens at the instant where each of the specimens reach their maximum loading. The plots illustrate how the distribution of the soft phases controls the pattern of the strain transfer, and thereby enable a distinct mechanism of deformation and failure. ....	54

Figure 22 (a) Triangular lattice spring-bead material representation to describe a coarse-grained model of the material. All lines are of identical length. The constitutive relations for stiff phase are presented along with three example constitutive relations for the soft phase, representing the first three combinations of elastic properties listed in Table 1. The area under all four curves drawn is identical. (b) Brick and mortar composite topology considered here. Platelets are drawn in red while matrix phase is represented with blue. The notch and mode I loading condition used here is also represented..... 59

Figure 23 Stress-strain responses for the bulk system and three composite structures,  $\rho = 0.64, 0.44$  and  $0.02$  (recall that  $\rho = E_{\text{soft}}/E_{\text{stiff}}$ ). The strain and the stress are normalized by the maximum strain and stress of the brittle bulk system. Graphs indicate the rapid change in composite behavior as the stiffness ratio is varied. .... 62

Figure 24 Longitudinal strain fields and Von Mises stress fields for the bulk system, (a) and (e); the composite structures with stiffness ratios  $\rho = 0.64$ , (b) and (f);  $\rho = 0.44$ , (c) and (g); and  $\rho = 0.02$ , (d) and (h). The longitudinal strain field plots clearly show the softer phase taking an increasing portion of the strain as the stiffness-ratio decreases accompanied by a delocalization of stress and strain from the crack tip and increased stress and strain in regions far from the crack tip. Panels (c) and (g) clearly exhibit the superior performance of the  $\rho = 0.44$  composite structures. Insets for panels (c) and (d) indicate a transition in fracture mechanism. 64

Figure 25 Normalized toughness modulus  $G_{\text{norm}}$  plotted versus stiffness-ratio  $\rho$  for all four tests on the ten specimens. The legend identifies the markers indicating the results for the simulations with the various displacement increments, 1 through 4 indicating displacement increments of  $0.42$  through  $3.38 \cdot 10^{-5}$ . The fitted curve is a sigmoid function described by  $f\rho = 1 + 6\exp(-63\rho + 33)/(1 + \exp(-63\rho + 33))$ . The parameters for this fit were found by method of penalized least squared errors. .... 66

Figure 26 Stress versus strain response of pristine and flawed system. Again, both stresses and strains are normalized by the maximum values of the flawed bulk sample. The pristine sample is seen to fail at a stress  $\sim 5.5$  times larger than the flawed bulk sample. .... 68

Figure 27 Ashby plot of normalized toughness modulus versus normalized Young's modulus plotted together with corresponding representative Ashby plots of synthetic and biological materials. Stiffness' are normalized versus the stiffness of the bulk system and toughness' are normalized versus the toughness of the bulk system. Markers for composite systems with stiffness ratios  $\rho > 0.5$  are drawn with blue circles while those for systems with  $\rho < 0.5$  are drawn with blue crosses. The modulus-toughness combinations of the building blocks are indicated with red stars (same for all cases, by design). The superior toughness of the composite systems with respect to the individual blocks is clearly exhibited. The impressive performance of the stiffest  $\rho < 0.5$  system is clearly seen, circled in green, with an eightfold increase in toughness accompanied with a stiffness of over 80 % of the stiff bulk system. The fitted curve is a fifth-degree polynomial fitted by minimizing residual squared error, again with a non-zero regularization term. The curve clearly indicates that the composite structures span the Ashby area in a similar fashion as biological composites [119]. Figure 24 exhibits the deformation mechanisms underlying the various mechanical performances indicated here. .... 69

Figure 28 Panel (a) shows schematics of the three investigated topologies. Panel (b) shows the setup of test specimens with relevant dimensions and coordinate system indicated. Panel (c) shows an image of the setup of the experiment. A specimen of the bone-like geometry is being tested in the picture, shown here as an example. .. 74

Figure 29 Images of samples at the start of testing, the end of testing and graphs of stress-strain response for base materials, material A and material B, as well as their computational equivalents. (a) Images of test specimens of material A and material B before and after testing. Pictures indicate brittle catastrophic failure of the base materials. (b) Stress versus strain behavior of experimental and computational base materials drawn in blue and green respectively. The modulus of computational equivalent of material A is seen to match with its experimental counterpart. Further, the extreme compliance of material B makes it barely visible on the original plot and thus its notched stress strain response is included in an inset of the figure. The computational equivalents of material A and B are designed to fail at lower strains to avoid geometrical instabilities in the model. Further, the computational equivalent of



material B is designed with a more humble compliance to avoid instabilities in the simulation, and to also more closely resemble the average mechanical properties of the printed compliant phase. .... 80

Figure 30 Snapshots are presented displaying deformation and fracture mechanisms for (a) the 3D-printed and (b) simulated specimen of the bone-like topology, in direct comparison. The two samples exhibit very similar deformation and fracture mechanisms up to a certain point at which the change of boundary conditions in the experiment and the nonlinearities of the photopolymers start dominating. This instant is indicated with a vertical line in the stress versus strain plots. The figure shows that in both the synthetic and computational system the soft phase absorbs the bulk of the deformation and acts to delocalize the stress concentration around the notch. For the computational case shown in panel (b) the longitudinal strain fields are plotted in insets to make this clearer. Furthermore, the inset in panel (a) (iii) displays the strong interfacial adhesion of material A and material B with failure nucleating through the compliant material B instead of at the interface. This is consistent with the results of the computational model. .... 82

Figure 31 Visualization of dominating deformation and fracture mechanisms in experiment and simulation for (a) the rotated bone-like geometry and (b) the bio-calcite-like geometry in addition to the respective stress-strain responses, again with blue and green indicating results from experiment and simulation respectively. Schematics of the topologies are included at the top. Panel (a) displays the characteristic zigzag fracture path observed both in the simulation and for the initial propagation in experiment. As the effective length of the sample decreases the eccentricity of the applied load increases, changing the boundary conditions and thus causing predictions from experiment and simulation to diverge. As is apparent from the displayed images, for both simulation and experiment, the compliant phase forces the crack to take a longer path thus inducing toughening in the rotated bone-like specimen. The stress strain responses also reveal that a very compliant behavior of this topology is correctly predicted. Panel (b) indicates that the simulation predictions and experimental observations for the bio-calcite-like topology do not overlap very well. The inset in panel (b) (ii) shows inaccuracies in the printing that

are likely a contributing factor. Nonetheless, a similar toughening mechanism is observed in experiment and simulation in that both systems show an initial crack arrest and crack blunting in a soft inclusion; (i), (iii). ..... 84

Figure 32 Bar plot indicating trends of mechanical properties for the base materials and the various topologies studied in both (a) experiment and (b) simulation. A comparison is performed using data from experiment and simulation up to the point in which the two systems exhibit diverging mechanisms; these instants are displayed in Figure 4 and 5. For the simulation data, A and B refer to the computational equivalents of material A and material B as presented in Figure 3. The mechanical properties plotted are stiffness  $E$ , maximum strain  $\varepsilon$ , maximum stress  $\sigma$ , and toughness modulus  $D$ . In panel (a) the data is, as indicated, normalized by the respective values for the base material A while in panel (b) the data is normalized by the respective values for the computational equivalent of the base material A. The figure portrays that, with the exception of the bio-calcite-like sample for reasons stated above, the mechanical properties of the simulated materials exhibit the same trends as those of the synthesized materials, *i.e.* the models predict the correct composite to be the most extensible, strongest and toughest. Furthermore, the largely impressive fracture toughness of the synthesized bone-like specimen is observed, exceeding that of its fundamental building blocks by a factor larger than 20. .... 87

Figure 33 Snapshots of fracture propagation in the synthesized bone-like specimen. Images clearly show two dominating toughening mechanisms exhibited by the printed composite. The second snapshot indicates a delocalized load transfer in the topology with damage being sustained away from the crack tip. Furthermore, a pronounced crack deflection mechanism is observed, induced by the particular topological arrangement of the two base materials with widely contrasting constitutive behavior. This causes the crack to take a long path through the specimen thus dissipating large amounts of energy on the way. Moreover, as the fracture mainly propagates through the extremely compliant base material B the crack is blunted, leading to a lesser stress concentration at the crack tip and thus stable fracture propagation. .... 89

Figure 34 Snapshots of fracture propagation in the synthesized rotated bone-like specimen. The second snapshot indicates the significant deformability of the composite in the presence of the crack; an apparent blunting of the crack-tip highlights this. Furthermore, the characteristic zigzag pattern of fracture propagation in panel (c) is observed, made possible by the extreme compliance of the matrix phase combined with the specific composite topology. As the eccentricity of the applied load increases crack branching is observed (d), followed by a dominating crack propagating to and along the boundary in panel (e) resulting in complete failure of the composite. .... 90

Figure 35 Snapshots of fracture propagation in the bio-calcite like specimen. As for the rotated bone-like specimen the specimen is observed to undergo significant deformation prior to major crack propagation, enabled by the crack-tip blunting displayed in panel (b), this was also highlighted in Figure 5. In panel (c) the crack has started to propagate towards the boundary and eventually reaches it in panel (f). The crack propagates slowly through the sample undergoing significant deformation in the process. It is clearly observed that the compliant phase influences the crack propagation path and leads to toughening in the composite indicated by the resulting rough fracture surface. .... 91

## 8.2 List of tables

Table 1 Tabular representation of the subsystems of the hierarchical structure of the four biomineralized materials; human vertebrate bone, the hexactinellid sponge <i>Euplectella</i> sp., the siliceous frustule of the diatom algae genus <i>Coscinodiscus</i> and the nacreous layers of the Japanese pearl <i>Pinctada fuctata</i> .....	24
Table 2 Overview of variables, dimensions and their definitions. Dimensions are given in terms of the base dimensions M, L and T. <i>M</i> .....	59
Table 3 Elastic constants for the stiff (platelets) and soft phase (matrix) of the composite. Constants are expressed in normalized units, $E \cdot \epsilon^2 = \text{const.}$ .....	61
Table 4 Summary of key mechanisms induced by changes to the constitutive laws. Three regimes are identified; $\rho > 0.6$ , $0.3 < \rho < 0.5$ , and $\rho < 0.3$ . The regime $0.5 < \rho < 0.6$ is as indicated in Figure 25 a transition regime and is therefore not discussed here. ....	71